

<sup>1</sup> SEARCH FOR  $t\bar{t}Z' \rightarrow t\bar{t}t\bar{t}$  PRODUCTION IN THE MULTILEPTON FINAL STATE IN  
<sup>2</sup>  $pp$  COLLISIONS AT  $\sqrt{s} = 13$  TEV WITH THE ATLAS DETECTOR

<sup>3</sup> By

<sup>4</sup> Hieu Le

<sup>5</sup> A DISSERTATION

<sup>6</sup> Submitted to  
<sup>7</sup> Michigan State University  
<sup>8</sup> in partial fulfillment of the requirements  
<sup>9</sup> for the degree of

<sup>10</sup> Physics — Doctor of Philosophy

<sup>11</sup> 2025

12

## ABSTRACT

13 This dissertation presents a search for a new beyond-the-Standard-Model (BSM) particle  
14 at the Large Hadron Collider (LHC). Many BSM models predict a new heavy vector boson  
15 ( $Z$ ) that couples primarily to the top quark in both production and decay (topophilic). The  
16 search is performed in multilepton events consistent with four-top-quark ( $t\bar{t}t\bar{t}$ ) production,  
17 due to the distinctive signature of the multilepton final states and its robustness against  
18 common background processes at the LHC. Analysis data was collected by the ATLAS  
19 detector from 2015 to 2018, using proton-proton collisions at the LHC at a center-of-mass  
20 energy of 13 TeV. No statistically significant deviation from Standard Model predictions is  
21 observed. Exclusion limits are set on the production cross section of the targeted topophilic  
22 particle in the mass range between 1 TeV and 3 TeV.

## ACKNOWLEDGMENTS

24        First and foremost, I am deeply grateful for my dissertation advisor and P.I, Professor  
25    Reinhard Schwienhorst, for his support, guidance and tolerance as part of my role in ATLAS  
26    and my doctoral program at Michigan State. Reinhard is the primary driving force in many  
27    exciting opportunities that I've had the chance to experience, and he also provides much-  
28    appreciated support both in knowledge and wisdom in times of need. I am incredibly thankful  
29    that Reinhard is one of the people that plays a part in who I am today.

30        I would like to express sincere gratitude to one of our postdocs in the MSU ATLAS  
31    group, Binbin Dong, who I closely worked with within ATLAS. Binbin is a massive source  
32    of support for physics, technical and ATLAS-specific knowledge that played a pivotal role  
33    during my training with ATLAS, during the analysis in this dissertation, and during my  
34    time at CERN. I would have never been able to find my way through without her help.

35        I am also extremely thankful for the MSU ATLAS group, in particular Professors Wade  
36    Fisher and Daniel Hayden, for their guidance and feedback on my professional and per-  
37    sonal endeavors which helped immensely in my development both scientifically and socially.  
38    I thank Rongqian Qian and Jason Gombas, my fellow advisees that offered great ideas,  
39    knowledge and friendship. I would like to thank Julia Hinds, Stergios Kazakos and Pratik  
40    Kafle for their support and companionship during my time at CERN. I also thank former and  
41    presents members of our group that I've had the pleasure to work with: Joey Huston, Jos  
42    Gabriel Reyes Rivera, Cecilia Imthurn, Xinfei Huang, Ahmed Tarek, Kyle Fielman, Robert  
43    Les and Trisha Farooque. It was a wonderful experience being part of the MSU ATLAS  
44    group and I hope our group continues to grow, even if it makes scheduling weekly meetings  
45    for everyone that much harder.

46 I would like to express my gratitude to my dissertation committee members, Professors  
47 Reinhard Schwienhorst, Johannes Pollanen, Wade Fisher, Remco Zegers and Yuying Xie, for  
48 their guidance, patience and commitment to my growth and success as a researcher and a  
49 person.

50 It has been a pleasure to work with the many outstanding people in ATLAS, especially  
51 the BSM multi-top analysis team. I would like to thank Philipp Gadow, Krisztian Peters,  
52 Frédéric Déliot and Neelam Kumari for their dedication and commitment to fostering a  
53 successful and fruitful collaboration. I also thank Meng-Ju Tsai, Hui-Chi Lin, Thomas  
54 Nommensen, Jianming Qian, Quake Qin, Tomke Schröer, Xilin Wang, Helena Gomez and  
55 Daniela Paredes for their tireless efforts in the analysis. I am truly glad to have had the  
56 chance to work with all of you.

57 Special thanks to my fellow graduate students that I have had the chance to befriend  
58 during my doctoral journey: Daniel Lay, Grayson Perez, Jordan Purcell, Eric Flynn, Isabella  
59 Molina, Mo Hassan, Cavan Maher and Hannah Berg. You all taught me a lot more than I  
60 could ever imagine and helped me more than I could ever asked for, and I look forward to  
61 see where we go from here.

62 Finally, I would like to thank my family, to whom this dissertation is dedicated: my  
63 spouse Allen Sechrist, for encouraging me tirelessly everyday and always being there for me  
64 even when I can't be there for myself; my cat Eddie, for being the best cat anyone could ask  
65 for; my brother Hien Le, my dad Bac Le, and my mom Thuy Cao, for their endless love and  
66 support. Thank you for being the reason that I am where I am today.

## TABLE OF CONTENTS

67	<b>List of Tables . . . . .</b>	vii
68	<b>List of Figures . . . . .</b>	ix
69	<b>KEY TO ABBREVIATIONS . . . . .</b>	xi
70	<b>Chapter 1. Introduction . . . . .</b>	1
71	<b>Chapter 2. Theoretical Overview . . . . .</b>	5
72	2.1 The Standard Model . . . . .	5
73	2.1.1 Elementary particles . . . . .	5
74	2.1.2 Mathematical formalism . . . . .	9
75	2.1.2.1 Quantum chromodynamics . . . . .	10
76	2.1.2.2 Electroweak theory . . . . .	11
77	2.1.2.3 Higgs mechanism . . . . .	14
78	2.2 Beyond the Standard Model: $t\bar{t}Z' \rightarrow t\bar{t}t\bar{t}$ . . . . .	17
79	2.2.1 Top-philic vector resonance . . . . .	17
80	2.2.2 Production channels . . . . .	19
81	2.2.3 Decay modes . . . . .	20
82	<b>Chapter 3. LHC &amp; ATLAS Experiment . . . . .</b>	21
83	3.1 The Large Hadron Collider . . . . .	21
84	3.1.1 Overview . . . . .	21
85	3.1.2 LHC operations . . . . .	23
86	3.1.3 Physics at the LHC . . . . .	24
87	3.2 The ATLAS detector . . . . .	24
88	3.2.1 Inner detector . . . . .	27
89	3.2.2 Calorimeter systems . . . . .	28
90	3.2.3 Muon spectrometer . . . . .	30
91	3.2.4 Trigger & data acquisition . . . . .	32
92	<b>Chapter 4. Particle Reconstruction &amp; Identification . . . . .</b>	33
93	4.1 Primary reconstruction . . . . .	33
94	4.1.1 Tracks . . . . .	33
95	4.1.2 Vertices . . . . .	34
96	4.1.3 Topological clusters . . . . .	35
97	4.2 Jets . . . . .	36
98	4.2.1 Jet reconstruction . . . . .	37
99	4.2.2 Flavor tagging . . . . .	38
100	4.3 Leptons . . . . .	42
101	4.3.1 Electrons . . . . .	42
102	4.3.2 Muons . . . . .	45

103	4.4	Missing transverse momentum . . . . .	47
104	4.5	Overlap removal . . . . .	48
105	4.6	Object definition . . . . .	49
106	<b>Chapter 5. Data &amp; Simulated Samples</b>	. . . . .	<b>50</b>
107	5.1	Data samples . . . . .	50
108	5.2	Monte Carlo samples . . . . .	50
109	5.2.1	$t\bar{t}Z'$ signal samples . . . . .	51
110	5.2.2	Background samples . . . . .	53
111	<b>Chapter 6. Analysis Strategy</b>	. . . . .	<b>58</b>
112	6.1	Event selection . . . . .	58
113	6.1.1	Event categorization . . . . .	59
114	6.2	Analysis regions . . . . .	60
115	6.2.1	Signal regions . . . . .	62
116	6.2.2	Control regions . . . . .	64
117	6.3	Background estimation . . . . .	66
118	6.3.1	Template fitting for fake/non-prompt estimation . . . . .	67
119	6.3.2	Charge misidentification data-driven estimation . . . . .	67
120	6.3.3	$t\bar{t}W$ background data-driven estimation . . . . .	70
121	<b>Chapter 7. Systematic Uncertainties</b>	. . . . .	<b>72</b>
122	7.1	Experimental uncertainties . . . . .	72
123	7.1.1	Luminosity & pile-up reweighting . . . . .	72
124	7.1.2	Leptons . . . . .	72
125	7.1.3	Jets . . . . .	73
126	7.1.4	Missing transverse energy . . . . .	75
127	7.2	Modeling uncertainties . . . . .	76
128	7.2.1	Signal and irreducible background uncertainties . . . . .	76
129	7.2.2	Reducible background uncertainties . . . . .	78
130	<b>Chapter 8. Results</b>	. . . . .	<b>80</b>
131	8.1	Statistical interpretation . . . . .	80
132	8.1.1	Profile likelihood fit . . . . .	80
133	8.1.2	Exclusion limit . . . . .	83
134	8.2	Fit results . . . . .	84
135	<b>Chapter 9. Summary</b>	. . . . .	<b>90</b>
136	<b>References</b>	. . . . .	<b>91</b>

# <sup>137</sup> List of Tables

<sup>138</sup> 137	Table 4.1: Overlap removal process for this analysis, applied sequentially from top to bottom. . . . .	48
<sup>140</sup> 141	Table 4.2: Summary of object selection criteria used in this analysis. $\ell_0$ refers to the leading lepton in the event. . . . .	49
<sup>142</sup> 143	Table 5.1: Summary of all HLT triggers used in this analysis. Events are required to pass at least one trigger. . . . .	51
<sup>144</sup> 145 <sup>146</sup> <sup>147</sup>	Table 5.2: Summary of all Monte-Carlo samples used in this analysis. $V$ refers to an EW ( $W^\pm/Z/\gamma^*$ ) or Higgs boson. Matrix element (ME) order refers to the order in QCD of the perturbative calculation. Tune refers to the underlying-event tune of the parton shower (PS) generator. . . . .	52
<sup>148</sup> 149 <sup>150</sup> <sup>151</sup> <sup>152</sup> <sup>153</sup>	Table 6.1: Definitions of signal, control and validation regions (VR) used in this analysis. $N_{\text{jets}}$ and $N_b$ refers to the number of jets and number of $b$ -tagged jets respectively. $\ell_1$ refers to the leading lepton, $\ell_2$ refers to the subleading lepton and so on. $H_T$ refers to the $p_T$ scalar sum of all leptons and jets in the event. $m_{\ell\ell}$ refers to the dilepton invariant mass, which must not coincide with the $Z$ -boson mass range of 81-101 GeV for SS2L+3L events. . . . .	61
<sup>154</sup> 155	Table 6.2: Definitions of SR sub-regions. Events are sorted into different sub-regions based on the number of $b$ -tagged jets and leptons present. . . . .	62
<sup>156</sup>	Table 6.3: List of possible assigned values for DFCAA. . . . .	65
<sup>157</sup> 158 <sup>159</sup> <sup>160</sup>	Table 8.1: Normalization factors for backgrounds with dedicated CRs, obtained from a simultaneous fit in all CRs and SR under the background-only hypothesis. The nominal pre-fit value is 1 for all NFs and 0 for the scaling factors $a_0$ and $a_1$ . Uncertainties shown include both statistical and systematic uncertainties.	86

161	Table 8.2: Pre-fit and post-fit background yields in the inclusive SR. The number of 162 data events and pre-fit estimate signal yields are also shown. Background 163 yields shown are obtained from the fit using the $t\bar{t}Z'$ signal sample with 164 $m_{Z'} = 2$ TeV. Pre-fit yields for $t\bar{t}W$ background are set to 0 nominally 165 prior to data-driven normalization. Total yield uncertainty differs from 166 the quadrature sum of constituent uncertainties due to correlation and 167 anticorrelation effects. . . . .	88
168	Table 8.3: Post-fit impact of uncertainty sources on the signal strength $\mu$ , grouped by 169 categories. Values shown are obtained from the fit using the $t\bar{t}Z'$ signal 170 sample with $m_{Z'} = 2$ TeV. Impact on $\mu$ is evaluated for each uncertainty 171 category by re-fitting with the corresponding set of NPs fixed to their best- 172 fit values. Total uncertainty differs from the quadrature sum of constituent 173 uncertainties due to correlation between NPs in the fit. . . . .	89

# <sup>174</sup> List of Figures

<sup>175</sup> Figure 2.1: Particles within the SM and their properties. . . . .	6
<sup>176</sup> Figure 2.2: Feynman diagram for $t\bar{t}$ production and subsequent decay processes. Top quark decays into a $W$ -boson and $b$ -quarks, and $W$ -boson can decay to a $q\bar{q}$ or a $\ell\nu_\ell$ pair. . . . .	<sup>177</sup> 8
<sup>179</sup> Figure 2.3: Illustration of a common representation of the Higgs potential. Before SSB, the ground state $\phi(0)$ is located at A which is symmetric with respect to the potential. A perturbation to this state fixes the ground state energy $ \phi(0) ^2$ to a particular value at B, "spontaneously" breaking the symmetry and degeneracy in $ \phi(0) ^2$ . . . . .	<sup>180</sup> 15
<sup>184</sup> Figure 2.4: Feynman diagrams for tree level $Z'$ production in association with (a) $t\bar{t}$ , (b) $tj$ (light quark) and (c) $tW$ , decaying to final states containing (a) $t\bar{t}t\bar{t}$ or (b)(c) $t\bar{t}t$ . . . . .	<sup>185</sup> 19
<sup>187</sup> Figure 2.5: Branching ratios for $t\bar{t}t\bar{t}$ decay. The same-sign dilepton and multilepton channels together forms the SSML channel. . . . .	<sup>188</sup> 20
<sup>189</sup> Figure 3.1: The full CERN accelerator complex as of 2022. . . . .	22
<sup>190</sup> Figure 3.2: Current and future timeline of LHC operations as of 2025 with corresponding center-of-mass energies and projected integrated luminosities. .	<sup>191</sup> 23
<sup>192</sup> Figure 3.3: Summary of predicted and measured cross-section for SM processes at the LHC at different center-of-mass energies . . . . .	<sup>193</sup> 25
<sup>194</sup> Figure 3.4: A cross section slice of the ATLAS detector showing different subsystems along with visualization of different types of particles traveling through the detector . . . . .	<sup>195</sup> 26
<sup>197</sup> Figure 3.5: Cutaway illustration of the inner detector along with its subsystems. . .	<sup>196</sup> 27

198	Figure 3.6: Cutaway illustration of the calorimeter system including the EM, hadronic 199 and LAr forward calorimeters . . . . .	29
200	Figure 4.1: Stages of topo-cluster formation corresponding to each threshold. In (a), 201 proto-clusters are seeded from cells with adequate signal significance $\zeta_{\text{cell}}^{\text{EM}}$ . 202 The clusters are further merged and split in (b) according to a predefined 203 cluster growth threshold. The process stops in (c) when all sufficiently 204 significant signal hits have been matched to a cluster. . . . .	36
205	Figure 4.2: Jet energy scale calibration sequence for EM-scale jets. . . . .	38
206	Figure 4.3: Overview of the GN2 architecture. The number of jet and track features 207 are represented by $n_{\text{jf}}$ and $n_{\text{tf}}$ respectively. The global jet representation 208 and track embeddings output by the Transformer encoder are used as 209 inputs for three task-specific networks. . . . .	40
210	Figure 4.4: The $c$ -, light- and $\tau$ -jet rejection rate as a function of $b$ -tagging efficiency 211 for GN2 and DL1d using (a) jets in the $t\bar{t}$ sample, and (b) jets in the $Z'$ 212 sample. The performance ratios of GN2 to DL1d are shown in the bottom 213 panels. . . . .	41
214	Figure 6.1: Post-fit background composition in each analysis region and sub-region. 215 The fit was performed using ideal pseudo-datasets (Asimov data) in the SR. . . . .	60
216	Figure 6.2: Pre-fit kinematic distributions and event compositions for several observ- 217 ables in the inclusive SR. The shaded band represents the uncertainty in 218 the total distribution. The first and last bins of each distribution contains 219 underflow and overflow events respectively. . . . .	63
220	Figure 6.3: Charge flip rate calculated for SR and CR $t\bar{t}W$ in bins of $ \eta $ and $p_{\text{T}}$ . . . . .	69
221	Figure 7.1: Combined QmisID uncertainty rate for SR in bins of $ \eta $ and $p_{\text{T}}$ . . . . .	79
222	Figure 8.1: Observed (solid line) and expected (dotted line) upper limits as a function 223 of the $Z'$ mass at 95% CL on the cross-section of $pp \rightarrow t\bar{t}Z'$ production 224 times the $Z' \rightarrow t\bar{t}$ branching ratio. The region above the observed limit is 225 excluded. The solid blue line represents the theoretical signal cross-section 226 with $c_t = 1$ at LO in QCD. The green and yellow bands represent the 227 68% ( $\pm\sigma$ ) and 95% ( $\pm 2\sigma$ ) confidence intervals respectively. . . . .	86
228	Figure 8.2: Comparison between data and post-fit prediction for the discriminant ob- 229 servable in each non-prompt and $t\bar{t}W$ background CR. The fit is per- 230 formed simultaneously in all CRs and SR under the background-only 231 hypothesis. The lower panel shows the ratio between data and post-fit 232 predictions. The shaded band represents the total uncertainty on the fit.	87

## KEY TO ABBREVIATIONS

### Physical & Mathematical Quantities

<sup>235</sup>  $\chi^2$  chi-squared

<sup>236</sup>  $d_0$  transverse impact parameter

<sup>237</sup>  $\Delta R$  angular distance

<sup>238</sup>  $\sqrt{s}$  center-of-mass energy

<sup>239</sup>  $\eta$  pseudorapidity

<sup>240</sup>  $E_T$  transverse energy

<sup>241</sup>  $E_T^{\text{miss}}$  missing transverse energy

<sup>242</sup>  $\Gamma$  decay width

<sup>243</sup>  $\gamma_5$  chirality projection operator

<sup>244</sup>  $\gamma_\mu$  Dirac matrices

<sup>245</sup>  $H_0$  null hypothesis

<sup>246</sup>  $H_T$  scalar sum of transverse momenta  $p_T$  of all objects in an event

<sup>247</sup>  $\mathcal{L}$  Lagrangian

<sup>248</sup>  $\mathcal{L}(\theta)$  likelihood function

<sup>249</sup>  $L$  instantaneous luminosity

<sup>250</sup>  $m_{\ell\ell}$  dilepton invariant mass

<sup>251</sup>  $\mu$  signal strength

<sup>252</sup>  $\mu_F$  factorization scale

<sup>253</sup>  $\mu_R$  renormalization scale

<sup>254</sup>  $N_{\text{jets}}$  number of jets/jet multiplicity

<sup>255</sup>  $\mathcal{O}(n)$  on the order of  $n$

<sup>256</sup>  $\mathcal{P}$  Poisson probability

<sup>257</sup>  $p_T$  transverse momentum

- <sup>258</sup>  $Q$  electric charge  
<sup>259</sup>  $q_\mu$  profile likelihood ratio  
<sup>260</sup>  $\sigma$  standard deviation  
<sup>261</sup>  $\sigma[b]$  cross-section  
<sup>262</sup>  $z_0$  longitudinal impact parameter

## 263 Particles & Processes

- <sup>264</sup>  $\gamma^*$  virtual photon  
<sup>265</sup>  $gg$  gluon-gluon fusion  
<sup>266</sup>  $pp$  proton-proton  
<sup>267</sup> PbPb lead-lead  
<sup>268</sup>  $q$  quark  
<sup>269</sup>  $q\bar{q}$  quark-antiquark pair  
<sup>270</sup>  $t\bar{t}$  top/anti-top quark pair  
<sup>271</sup>  $t\bar{t}X$  top pair in association with another particle  
<sup>272</sup>  $t\bar{t}t\bar{t}$  four-top-quark  
<sup>273</sup>  $V$  massive vector bosons ( $W^\pm, Z$ )  
<sup>274</sup>  $H$  Higgs in association with a vector boson

## 275 Acronyms

- <sup>276</sup> **1LOS** one lepton, or two leptons of opposite charges  
<sup>277</sup> **2HDM** two-Higgs doublet model  
<sup>278</sup> **AF3** AtlFast3 fast simulation  
<sup>279</sup> **ALICE** A Large Ion Collider Experiment  
<sup>280</sup> **ATLAS** A Toroidal LHC ApparatuS  
<sup>281</sup> **AWAKE** Advanced WAKEfield Experiment  
<sup>282</sup> **BDT** boosted decision tree  
<sup>283</sup> **BR** branching ratio

- <sup>284</sup> **BSM** Beyond the Standard Model
- <sup>285</sup> **CB** combined muon
- <sup>286</sup> **CERN** European Organization for Nuclear Research
- <sup>287</sup> **CKM** Cabibbo-Kobayashi-Maskawa matrix
- <sup>288</sup> **CL** confidence level
- <sup>289</sup> **CMS** Compact Muon Solenoid
- <sup>290</sup> **CP** charge-parity symmetry
- <sup>291</sup> **CR** control region
- <sup>292</sup> **CSC** Cathode Strip Chambers
- <sup>293</sup> **CTP** Central Trigger Processor
- <sup>294</sup> **ECIDS** Electron Charge ID Selector
- <sup>295</sup> **EFT** effective field theory
- <sup>296</sup> **EM** electromagnetic
- <sup>297</sup> **EW** electroweak
- <sup>298</sup> **FASER** ForwArd Search ExpeRiment
- <sup>299</sup> **FCal** forward calorimeter
- <sup>300</sup> **FS** full detector simulation
- <sup>301</sup> **GNN** graph neural network
- <sup>302</sup> **GRL** Good Run List
- <sup>303</sup> **GSC** Global Sequential Calibration
- <sup>304</sup> **GSF** Gaussian-sum filter
- <sup>305</sup> **GUT** Grand Unified Theory
- <sup>306</sup> **HEC** hadronic endcap calorimeter
- <sup>307</sup> **HF** heavy-flavor
- <sup>308</sup> **HL-LHC** High-Luminosity Large Hadron Collider
- <sup>309</sup> **HLT** High-Level Trigger
- <sup>310</sup> **ID** Inner Detector

- <sup>311</sup> **IP** interaction point
- <sup>312</sup> **JER** jet energy resolution
- <sup>313</sup> **JES** jet energy scale
- <sup>314</sup> **JVT** Jet Vertex Tagger
- <sup>315</sup> **KATRIN** Karlsruhe Tritium Neutrino Experiment
- <sup>316</sup> **L1** Level 1
- <sup>317</sup> **LAr** liquid argon
- <sup>318</sup> **LF** light-flavor
- <sup>319</sup> **LH** likelihood
- <sup>320</sup> **LHC** Large Hadron Collider
- <sup>321</sup> **LHCb** Large Hadron Collider beauty
- <sup>322</sup> **LINAC** linear accelerator
- <sup>323</sup> **LLH** log-likelihood
- <sup>324</sup> **LO** leading order
- <sup>325</sup> **MC** Monte Carlo simulation
- <sup>326</sup> **ME** matrix element
- <sup>327</sup> **ML** multilepton
- <sup>328</sup> **MS** Muon Spectrometer
- <sup>329</sup> **MDT** Monitored Drift Tubes
- <sup>330</sup> **MET** missing transverse energy
- <sup>331</sup> **NF** normalization factor
- <sup>332</sup> **NNJvt** Neural Network-based Jet Vertex Tagger
- <sup>333</sup> **NLO** next-to-leading order
- <sup>334</sup> **NNLO** next-to-next-to-leading order
- <sup>335</sup> **NP** nuisance parameter
- <sup>336</sup> **OP** operating point (also working point)
- <sup>337</sup> **OS** opposite-sign

- <sup>338</sup> **PCBT** pseudo-continuous  $b$ -tagging
- <sup>339</sup> **PDF** parton distribution function
- <sup>340</sup> **POI** parameter of interest
- <sup>341</sup> **PS** parton shower
- <sup>342</sup> **PV** primary vertex
- <sup>343</sup> **QCD** quantum chromodynamics
- <sup>344</sup> **QED** quantum electrodynamics
- <sup>345</sup> **QFT** quantum field theory
- <sup>346</sup> **QmisID** charge mis-identification
- <sup>347</sup> **RPC** Resistive Plate Chamber
- <sup>348</sup> **SCT** Semiconductor Tracker
- <sup>349</sup> **SF** scale factor
- <sup>350</sup> **SM** Standard Model
- <sup>351</sup> **SR** signal region
- <sup>352</sup> **SS** same-sign
- <sup>353</sup> **SSB** spontaneous symmetry breaking
- <sup>354</sup> **SS2L** same-sign dilepton
- <sup>355</sup> **SSML** same-sign dilepton, or more than two leptons of any charges
- <sup>356</sup> **TDAQ** Trigger and Data Acquisition
- <sup>357</sup> **TGC** Thin-Gap Chamber
- <sup>358</sup> **TRT** Transition Radiation Tracker
- <sup>359</sup> **VEV** vacuum expectation value
- <sup>360</sup> **VR** validation region
- <sup>361</sup> **UE** underlying-event

# 362 Chapter 1. Introduction

363 The 20<sup>th</sup> century ushered in a revolutionary period for mankind's understanding of the  
364 fundamental nature of matter and the forces that govern our universe with the development  
365 of special relativity and quantum mechanics, which redefined our understanding of space,  
366 time, energy and matter at the furthest extremes of scale from the vast reaches of the cosmos  
367 to the tiniest constituents of matter. Building on these principles, Quantum Electrodynamics  
368 (QED) [1–3] was developed as the first successful quantum field theory (QFT) describing  
369 electromagnetism. The discovery of beta decay [4] and its paradoxical behaviors within the  
370 framework of QED prompted the prediction of neutrinos and development of the theory of  
371 weak interaction.

372 At around the same time, a spectrum of strongly interacting particles was discovered  
373 [5] as particle accelerators probed deeper into atomic nuclei, leading to the formation of  
374 the quark model in the 1960s and with it a hypothesized new binding force, the strong  
375 force. However, the QFT framework remained incapable of describing the weak and strong  
376 interactions until advancements in gauge theory and the quantization of non-Abelian gauge  
377 via QFT resulted in the formation of Yang-Mills theory [6, 7]. This sparked a renaissance  
378 in modern physics with the unification of electromagnetism and weak force in 1967 under  
379 the framework of electroweak (EW) [8] theory, as well as the development of Quantum  
380 Chromodynamics (QCD) [9, 10] to describe the strong force binding quarks.

381 At this point, the prediction of massless bosons within EW formalism remained a contra-  
382 diction to the predicted massive  $W^\pm$  and  $Z$  bosons that mediate the weak force. This was  
383 resolved by the introduction of EW spontaneous symmetry breaking and the Higgs mech-  
384 anism in 1964 [11–13], which explained the generation of masses for both the EW bosons

and fermions. Together, these developments culminated in the Standard Model of particle physics SM [14], a comprehensive theory that described the electromagnetic, weak, and strong interactions, classified all known fundamental particles and predicted mathematically consistent but not yet observed particles. Following its inception, particles predicted by the Standard Model were gradually observed experimentally, starting with the gluon in 1979 [15], then the  $W^\pm$  and  $Z$  bosons [16, 17], and finally the top quark in 1995 [18, 19]. The final missing piece was confirmed as the Higgs boson was observed in 2012 independently by the ATLAS [20] and CMS [21] detectors at the Large Hadron Collider, completing the Standard Model after a 40-year search and cementing it as the most successful framework so far describing fundamental constituents of matter and their governing forces.

Despite its successes, the Standard Model remains incomplete. Key unanswered questions include the nature of dark matter [22], which makes up about 27% of the universe's energy content but has no explanation within the Standard Model; the origin of neutrino masses and their oscillations [23]; the observed matter-antimatter asymmetry in the universe; possible unification of the EW and strong interaction into a Grand Unified Theory (GUT); and the hierarchy problem describing the large discrepancy in scales between forces and the apparent lightness of the Higgs boson compared to values predicted from quantum corrections.

After the discovery of the Higgs boson, efforts have been underway to construct new hypotheses and models in search of beyond the Standard Model (BSM) physics via different avenues, one of which being direct searches at colliders for new resonances or particles not predicted by the SM. In particular, the top quark possesses large mass and strong coupling to the Higgs boson [24] which gives it a special role in many proposed BSM models as a possible connection with strong coupling to new particles and heavy resonances. In addition, the top quark has a clean decay signature with well-understood final states and is produced in

abundance at the LHC from  $pp$  collisions in the form of top pairs  $t\bar{t}$  [25, 26]. This dissertation presents a search for the production of a heavy resonance that couples preferentially to top quark (top-philic) in association with a top pair ( $t\bar{t}$ ) in the final state with either two leptons of the same electric charge or at least three leptons (SSML). The search is performed in proton-proton collisions at  $\sqrt{s} = 13$  TeV with the ATLAS detector [27] via the four-top ( $t\bar{t}t\bar{t}$ ) production channel.

A similar search for top-philic heavy resonances was performed using a  $t\bar{t}t\bar{t}$  final state containing either one lepton or two opposite-sign leptons (1LOS) [28] with a much larger branching ratio of 56% and larger irreducible background of SM processes. Despite the small cross-section within the SM, the  $t\bar{t}t\bar{t}$  SSML final state provides heightened sensitivity to BSM physics and higher signal-to-background ratio than inclusive resonance searches (e.g. in dijet or dilepton final states) due to the distinctive signal signature and suppression of large SM background processes present in  $t\bar{t}$ -associated production i.e. diboson ( $VV$ ),  $t\bar{t}$  production with an additional boson ( $t\bar{t}V/ttH+jets$ ) or with additional light leptons from heavy-flavor decays ( $t\bar{t} + HF$ ). The cross-section for  $t\bar{t}t\bar{t}$  production can be enhanced by many proposed BSM models including supersymmetric gluino pair-production [29, 30], scalar gluon pair-production [31, 32], top-quark-compositeness models [33, 34], effective field theory (EFT) operators [26, 35–38] and two-Higgs-doublet models (2HDM) [39–43]. Searching within this channel is particularly motivated by the recent observed excess in the measurement of four-top production in the SSML final state at the LHC by the ATLAS detector [44] with a measured cross-section of  $24^{+7}_{-6}$  fb, almost double the SM prediction of  $13.4^{+1.0}_{-1.8}$  fb.

A simplified color-singlet vector boson model [45] is employed for the search to minimize parameter dependency on model choice. Data-driven background estimation methods are implemented for  $t\bar{t}W$ - one of the dominant irreducible backgrounds in the analysis - and

433 the charge misidentification background to rectify mismodeling related to jet multiplicity  
434 in simulated background that were not covered in the previous 1LOS search [28]. These  
435 methods are employed similarly to that in previous SM  $t\bar{t}t\bar{t}$  analyses [44, 46].

436 This dissertation is organized as follows. Chapter 2 presents the formalism of the SM and  
437 relevant BSM concepts. Chapter 3 provides an introduction to the LHC and ATLAS detector.  
438 Chapter 4 describes the reconstruction and identification of physics object from detector  
439 signals. Chapter 5 defines the data and simulated samples used in the analysis. Chapter 6  
440 describes the analysis strategy, including object definition, analysis region description and  
441 background estimation methods. Chapter 7 summarizes the uncertainties involved in the  
442 analysis. Chapter 8 presents the statistical interpretation and analysis results. Finally,  
443 Chapter 9 discusses a summary of the analysis and future outlook.

# 444 Chapter 2. Theoretical Overview

## 445 2.1 The Standard Model

446 The Standard Model of Physics (SM) [47] is currently the most successful formalism to  
447 describe the physical world at a microscopic scale by providing descriptions for all currently  
448 known elementary particles, along with three out of four fundamental forces (electromag-  
449 netism, weak force, strong force) with the exception of gravity. The SM is however not  
450 perfect, and there remains unanswered questions that require development and discovery  
451 of new physics beyond the Standard Model (BSM). This chapter describes an overview of  
452 important components within the SM and relevant BSM aspects for this analysis.

### 453 2.1.1 Elementary particles

454 Elementary particles in the SM can be classified into two groups: bosons consisting  
455 of particles following Bose-Einstein statistics with integer spin, and fermions consisting of  
456 particles following Fermi-Dirac statistics with half-integer spin. Fermions are the building  
457 blocks of composite particles and consequently all known matter, and can be further classified  
458 into quarks & leptons. Bosons act as force mediators for all fundamental forces described by  
459 the SM, and can either be a scalar boson with spin 0 or vector gauge bosons with spin 1. For  
460 each elementary particle, there also exists a corresponding antiparticle with identical mass  
461 and opposite charge (electric or color). Figure 2.1 shows all known elementary particles in  
462 the SM.

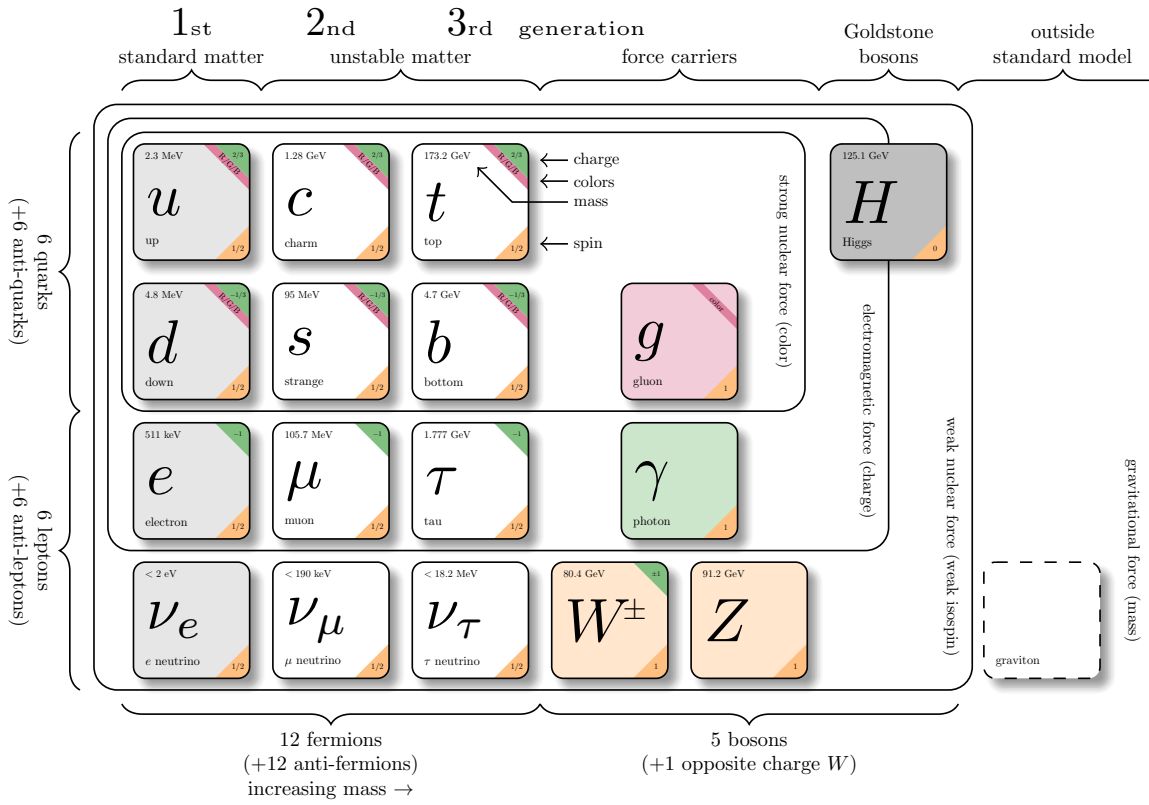


Figure 2.1: Particles within the SM and their properties [48].

## 463 Fermions

464 Fermions consist of quarks and leptons with six flavors each, grouped into three genera-  
 465 tions of doublets. The six quark flavors are up ( $u$ ), down ( $d$ ), charm ( $c$ ), strange ( $s$ ), bottom  
 466 ( $b$ ) and top ( $t$ ), arranged in increasing order of mass. The quark flavors form three doublets  
 467 ( $u, d$ ), ( $c, s$ ) and ( $t, b$ ), with each doublet containing one quark with electric charge of  $+2/3$   
 468 ( $u, s, t$ ), and the other with charge of  $-1/3$  ( $d, c, b$ ). Each quark also possesses a property  
 469 known as color charge, with possible values of red ( $R$ ), green ( $G$ ), blue ( $B$ ) or their corre-  
 470 sponding anticolor ( $\bar{R}, \bar{G}, \bar{B}$ ). Color charge follows color confinement rules, which allows  
 471 only configurations of quarks with total neutral color charge to exist in isolation. Neutral

472 charge configurations can be formed from either a set of three colors ( $R, G, B$ ), a set of a  
473 color and its anticolor, or any combination of the two. Consequently, quarks can only exist  
474 in bound states called hadrons and no isolated quark can be found in a vacuum. Quarks are  
475 the only elementary particles in the SM that can interact with all four fundamental forces.

476 The three leptons doublets consist of three charged leptons: electron ( $e$ ), muon ( $\mu$ ), tau  
477 ( $\tau$ ), and their respective neutrino flavors: electron neutrino ( $\nu_e$ ), muon neutrino ( $\nu_\mu$ ), tau  
478 neutrino ( $\nu_\tau$ ). Charged leptons carry an electric charge of  $-1$ , while their antiparticles carry  
479 the opposite charge ( $+1$ ) and their corresponding neutrino flavors carry no charge. Charged  
480 leptons interact with all fundamental forces except the strong force, while neutrinos only  
481 interact with the weak force and gravity.

## 482 **Bosons**

483 The SM classifies bosons into two types: one scalar boson with spin 0 known as the  
484 Higgs ( $H$ ) boson, and vector gauge bosons with spin 1 known as gluons ( $g$ ), photon ( $\gamma$ ),  $W^\pm$   
485 and  $Z$  bosons [22]. Gluons and photon are massless, while the  $W^\pm$ ,  $Z$  and  $H$  bosons are  
486 massive. Each vector gauge boson serves as the mediator for a fundamental force described  
487 by the SM. Gluons are massless particles mediating the strong interaction by carrying color  
488 charges between quarks following quantum chromodynamics (QCD). Each gluon carries a  
489 non-neutral color charge out of eight linearly independent color states in the gluon color octet  
490 [49]. The photon is the massless and charge-neutral mediator particle for the electromagnetic  
491 interaction following quantum electrodynamics (QED). The  $W^\pm$  and  $Z$  bosons are massive  
492 mediator particles for the weak interaction, with the  $W^\pm$  boson carrying an electric charge  
493 of  $\pm 1$  while the  $Z$  boson is charge neutral.

494 Other than the vector gauge boson, the only scalar boson in the SM is the massive and

495 charge neutral Higgs boson [22]. The Higgs boson does not mediate any fundamental force  
 496 like vector bosons, but serve to provide the rest mass for all massive elementary particles in  
 497 the SM through the Higgs mechanism described in section 2.1.2.3.

498 **Top quark**

499 As of now, the top quark ( $t$ ) is the heaviest particle in the SM with mass of about 173 GeV  
 500 [50], approaching the EW symmetry breaking scale. Its high mass gives the top quark the  
 501 strongest Yukawa coupling to the Higgs boson ( $y_t \approx 1$ ) [24] and exotic resonances in many  
 502 proposed BSM models [51–54], making the top quark and its processes attractive vehicles  
 503 with which to probe new physics.

504 Due to its mass, the top quark has a  
 505 very short lifetime of  $10^{-24}$  s [22] and de-  
 506 cays before it can hadronize following color  
 507 confinement. The top quark decays to a  $W$   
 508 boson and a  $b$ -quark with a branching ratio  
 509 of almost 100%. The  $W$  boson can subse-  
 510 quently decay to a quark-antiquark pair or  
 511 to a lepton-neutrino pair (Figure 2.2), with  
 512 branching ratios of approximately 68% and  
 513 32% respectively. All lepton flavors have  
 514 similar branching ratios during a leptonic  $W$   
 515 decay, assuming lepton universality.

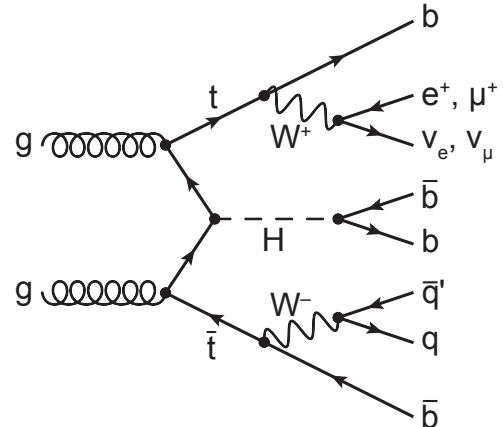


Figure 2.2: Feynman diagram for  $t\bar{t}$  production and subsequent decay processes [55]. Top quark decays into a  $W$ -boson and  $b$ -quarks, and  $W$ -boson can decay to a  $q\bar{q}$  or a  $\ell\nu_\ell$  pair.

### 516 2.1.2 Mathematical formalism

517 The SM can be described within the formalism of quantum field theory (QFT) with the  
518 Lagrangian [56]

$$\mathcal{L}_{\text{SM}} = \mathcal{L}_{\text{QCD}} + \underbrace{(\mathcal{L}_{\text{gauge}} + \mathcal{L}_{\text{fermion}} + \mathcal{L}_{\text{Higgs}} + \mathcal{L}_{\text{Yukawa}})}_{\mathcal{L}_{\text{EW}}} \quad (2.1)$$

519 where  $\mathcal{L}_{\text{QCD}}$  is the QCD term and  $\mathcal{L}_{\text{EW}}$  is the electroweak (EW) term of the Lagrangian.  
520 Formalism of QFT within the SM treats particles as excitations [57] of their corresponding  
521 quantum fields i.e. fermion field  $\psi$ , electroweak boson fields  $W_{1,2,3}$  &  $B$ , gluon fields  $G_\alpha$  and  
522 Higgs field  $\phi$ .

523 The foundation of modern QFT involves gauge theory. A quantum field has gauge sym-  
524 metry if there exists a continuous gauge transformation that when applied to every point in  
525 a field (local gauge transformation) leaves the field Lagrangian unchanged. The set of gauge  
526 transformations of a gauge symmetry is the symmetry group of the field which comes with  
527 a set of generators, each with a corresponding gauge field. Under QFT, the quanta of these  
528 gauge fields are called gauge bosons.

529 The SM Lagrangian is gauge invariant under global Poincaré symmetry and local  $SU(3)_C \times$   
530  $SU(2)_L \times U(1)_Y$  gauge symmetry, with the  $SU(3)_C$  symmetry group corresponding to the  
531 strong interaction and  $SU(2)_L \times U(1)_Y$  to the EW interaction. Global Poincaré symmetry  
532 ensures that  $\mathcal{L}_{\text{SM}}$  satisfies translational symmetry, rotational symmetry and Lorentz boost  
533 frame invariance [58]. These symmetries give rise to corresponding conservation laws, which  
534 lead to conservation of momentum, angular momentum and energy in the SM as a result of  
535 Noether's theorem [59].

536 **2.1.2.1 Quantum chromodynamics**

537 Quantum chromodynamics is a non-Abelian gauge theory i.e. Yang-Mills theory [6, 7]  
538 describing the strong interaction between quarks in the SM with the gauge group  $SU(3)_C$ ,  
539 where  $C$  represents conservation of color charge under  $SU(3)_C$  symmetry. According to  
540 QFT, quarks can be treated as excitations of the corresponding quark fields  $\psi$ . The free Dirac  
541 Lagrangian for the quark fields  $\mathcal{L}_0 = \bar{\psi}(i\gamma^\mu\partial_\mu - m)\psi$  is invariant under global  $SU(3)$  sym-  
542 metry, but not under local  $SU(3)_C$  symmetry. To establish invariance under local  $SU(3)_C$   
543 symmetry, the gauge covariant derivative  $D_\mu$  is defined so that

$$D_\mu\psi = (\partial_\mu - ig_s G_\mu^a T_a)\psi, \quad (2.2)$$

544 where  $g_s = \sqrt{4\pi\alpha_s}$  is the QCD coupling constant,  $G_\mu^a(x)$  are the eight gluon fields, and  
545  $T_a$  are generators of  $SU(3)_C$ , represented as  $T_a = \lambda_a/2$  with  $\lambda_a$  being the eight Gell-Mann  
546 matrices [49]. Let the gluon field strength tensors  $G_{\mu\nu}^a$  be

$$G_{\mu\nu}^a \equiv \partial_\mu G_\nu^a - \partial_\nu G_\mu^a - g_s f^{abc} G_\mu^b G_\nu^c, \quad (2.3)$$

547 where  $f^{abc}$  are the structure constants of  $SU(3)_C$ . The gauge invariant QCD Lagrangian  
548 can then be written as

$$\begin{aligned} \mathcal{L}_{\text{QCD}} &= \bar{\psi}(i\gamma^\mu D_\mu - m)\psi - \frac{1}{4}G_{\mu\nu}^a G_a^{\mu\nu} \\ &= \underbrace{-\frac{1}{4}G_{\mu\nu}^a G_a^{\mu\nu}}_{\text{gluon kinematics}} + \underbrace{\bar{\psi}(i\gamma^\mu\partial_\mu - m)\psi}_{\text{quark kinematics}} + \underbrace{\bar{\psi}^i(g_s\gamma^\mu(T_a)_{ij}G_\mu^a)\bar{\psi}^j}_{\text{quark-gluon interaction}}, \end{aligned} \quad (2.4)$$

549 where  $i, j$  are color indices with integer values from 1 to 3. Gluons are forced to be massless  
 550 from the lack of a gluon mass term to maintain gauge invariance for the Lagrangian.

551 **2.1.2.2 Electroweak theory**

552 The electroweak interaction is the unified description of the weak interaction and electro-  
 553 magnetism under the  $SU(2)_L \times U(1)_Y$  symmetry group, where  $L$  represents the left-handed  
 554 chirality of the weak interaction and  $Y$  represents the weak hypercharge quantum number.  
 555 Fermions can have either left-handed or right-handed chirality with the exception of neutrili-  
 556 nos which can only have left-handed chirality in the SM, and can be divided into left-handed  
 557 doublets and right-handed singlets

$$\psi_L = \begin{pmatrix} \nu_e \\ e_L \end{pmatrix}, \begin{pmatrix} \nu_\mu \\ \mu_L \end{pmatrix}, \begin{pmatrix} \nu_\tau \\ \tau_L \end{pmatrix}, \begin{pmatrix} u_L \\ d_L \end{pmatrix}, \begin{pmatrix} c_L \\ s_L \end{pmatrix}, \begin{pmatrix} t_L \\ b_L \end{pmatrix} \quad (2.5)$$

$$\psi_R = e_R, \mu_R, \tau_R, u_R, d_R, c_R, s_R, t_R, b_R.$$

558 where  $g'$  is the  $B_\mu$  coupling constant and  $B_\mu(x)$  is a vector gauge field that transforms under  
 559  $U(1)_Y$  as

$$B_\mu \rightarrow B_\mu + \frac{1}{g'} \partial_\mu \theta(x). \quad (2.6)$$

560 Right-handed fermion singlets are not affected by  $SU(2)_L$  transformation, so the fermion  
 561 fields  $\psi$  transform under  $SU(2)_L$  as

$$\psi_L \rightarrow e^{iI_3\vec{\theta}(x)\cdot\vec{\sigma}/2}\psi_L \quad (2.7)$$

$$\psi_R \rightarrow \psi_R.$$

562 where  $\vec{\sigma}/2$  are generators of  $SU(2)_L$  with  $\vec{\sigma}$  being the Pauli matrices. In order to preserve  
 563 local symmetry, the gauge covariant derivative for  $SU(2)_L$  and  $U(1)_Y$  can be defined [60] so

<sup>564</sup> that the gauge covariant derivative for  $SU(2)_L \times U(1)_Y$  can be written as

$$\begin{aligned} D_\mu \psi_L &= \left( \partial_\mu - ig' \frac{Y_L}{2} B_\mu - ig \frac{\sigma_i}{2} W_\mu^i \right) \psi_L \\ D_\mu \psi_R &= \left( \partial_\mu - ig' \frac{Y_R}{2} B_\mu \right) \psi_R. \end{aligned} \quad (2.8)$$

<sup>565</sup> where  $B_\mu(x)$  is a vector gauge field associated with  $U(1)_Y$  and  $W_\mu^i(x)$  ( $i = 1, 2, 3$ ) are three  
<sup>566</sup> vector gauge fields associated with  $SU(2)_L$ . The  $B_\mu$  and  $W_\mu^i$  gauge fields transform under  
<sup>567</sup> their corresponding symmetry groups  $U(1)_Y$  and  $SU(2)_L$  as

$$\begin{aligned} B_\mu &\rightarrow B_\mu + \frac{1}{g'} \partial_\mu \theta(x) \\ W_\mu^i &\rightarrow W_\mu^i + \frac{2}{g} \partial_\mu \theta_a(x) + \epsilon^{ijk} \theta_j(x) W_\mu^k, \end{aligned} \quad (2.9)$$

<sup>568</sup> where  $g'$  is the  $B_\mu$  gauge coupling constant,  $g$  is the  $W_\mu^i$  gauge coupling constants and  $\epsilon^{ijk}$   
<sup>569</sup> is the  $SU(2)_L$  structure constant. Similar to section 2.1.2.1, the kinetic term is added by  
<sup>570</sup> defining field strengths for the four gauge fields

$$\begin{aligned} B_{\mu\nu} &\equiv \partial_\mu B_\nu - \partial_\nu B_\mu \\ W_{\mu\nu}^i &\equiv \partial_\mu W_\nu^i - \partial_\nu W_\mu^i - g e^{ijk} W_\mu^j W_\nu^k. \end{aligned} \quad (2.10)$$

<sup>571</sup> The local  $SU(2)_L \times U(1)_Y$  invariant EW Lagrangian [60] is then

$$\begin{aligned} \mathcal{L}_{\text{EW}} &= i \bar{\psi} (\gamma^\mu D_\mu) \psi - \frac{1}{4} W_{\mu\nu}^i W_i^{\mu\nu} - \frac{1}{4} B_{\mu\nu} B^{\mu\nu} \\ &= \underbrace{i \bar{\psi} (\gamma^\mu \partial_\mu) \psi}_{\text{fermion kinematics}} - \underbrace{\bar{\psi} \left( \gamma^\mu g' \frac{Y}{2} B_\mu \right) \psi}_{\text{fermion-gauge boson interaction}} - \underbrace{\bar{\psi}_L \left( \gamma^\mu g \frac{\sigma_i}{2} W_\mu^i \right) \psi_L}_{\text{boson kinematics \& self-interaction}} - \frac{1}{4} W_{\mu\nu}^i W_i^{\mu\nu} - \frac{1}{4} B_{\mu\nu} B^{\mu\nu}. \end{aligned} \quad (2.11)$$

Under  $\approx 159.5$  GeV, the EW symmetry  $SU(2)_L \times U(1)_Y$  undergoes spontaneous symmetry breaking [61] into  $U(1)_{\text{QED}}$  symmetry, which corresponds to a separation of the weak and electrodynamic forces. Electroweak spontaneous symmetry breaking replaces the four massless and similarly-behaved EW gauge bosons  $B_\mu$  and  $W_\mu^i$  with the EM boson  $\gamma$  and the weak bosons  $Z/W^\pm$ , as well as giving the  $Z$  and  $W^\pm$  bosons masses via the Higgs mechanism.  
 This is due to a specific choice of gauge for the Higgs field leading to the reparameterization of the EW bosons  $B_\mu$  and  $W_\mu^i$  to  $W^\pm/Z/\gamma$  using the relations

$$\begin{aligned}
 W_\mu^\pm &\equiv \frac{1}{\sqrt{2}} (W_\mu^1 \mp iW_\mu^2) \\
 \begin{pmatrix} A_\mu \\ Z_\mu \end{pmatrix} &\equiv \begin{pmatrix} \cos \theta_W & \sin \theta_W \\ -\sin \theta_W & \cos \theta_W \end{pmatrix} \begin{pmatrix} B_\mu \\ W_\mu^3 \end{pmatrix}
 \end{aligned} \tag{2.12}$$

where  $\theta_W \equiv \cos^{-1} (g/\sqrt{g^2 + g'^2})$  is the weak mixing angle. The boson kinetic term can also be refactorized to extract cubic (three vertices) and quartic (four vertices) self-interactions among the gauge bosons [60]. The Lagrangian can then be rewritten as

$$\begin{aligned}
 \mathcal{L} = & \underbrace{eA_\mu \bar{\psi} (\gamma^\mu Q) \psi}_{\text{electromagnetism}} + \underbrace{\frac{e}{2\sin \theta_W \cos \theta_W} \bar{\psi} \gamma^\mu (v_f - a_f \gamma_5) \psi Z_\mu}_{\text{neutral current interaction}} \\
 & + \underbrace{\frac{g}{2\sqrt{2}} \sum_{\psi_L} [\bar{f}_2 \gamma^\mu (1 - \gamma_5) f_1 W_\mu^+ + \bar{f}_1 \gamma^\mu (1 - \gamma_5) f_2 W_\mu^-]}_{\text{charged current interaction}} \\
 & + \underbrace{\mathcal{L}_{\text{kinetic}} + \mathcal{L}_{\text{cubic}} + \mathcal{L}_{\text{quartic}}}_{\text{boson self-interaction}}
 \end{aligned} \tag{2.13}$$

where  $\gamma_5 = i\gamma^0\gamma^1\gamma^2\gamma^3$  is the chirality projection operator,  $a_f = I_3$ ,  $v_f = I_3(1 - 4|Q|\sin^2 \theta_W)$  and  $f_1, f_2$  are up and down type fermions of a left-handed doublet.

<sup>584</sup> **2.1.2.3 Higgs mechanism**

<sup>585</sup> So far, the EW bosons are massless since the mass terms  $-m\bar{\psi}\psi$  for fermions and  
<sup>586</sup>  $-mA^\mu A_\mu$  for bosons are not invariant under the EW Lagrangian symmetries. The parti-  
<sup>587</sup> cles must then acquire mass under another mechanism. The Brout-Engler-Higgs mechanism  
<sup>588</sup> [11–13] was introduced in 1964 to rectify this issue and verified in 2012 with the discovery  
<sup>589</sup> of the Higgs boson [20, 21].

<sup>590</sup> The Higgs potential is expressed as

$$V(\phi^\dagger \phi) = \mu^2 \phi^\dagger \phi + \lambda (\phi^\dagger \phi)^2 \quad (2.14)$$

<sup>591</sup> where  $\mu^2$  and  $\lambda > 0$  are arbitrary parameters, and the  $SU(2)_L$  doublet  $\phi = \begin{pmatrix} \phi^+ \\ \phi^0 \end{pmatrix}$  is the Higgs  
<sup>592</sup> field with complex scalar fields  $\phi^+$  and  $\phi^0$  carrying +1 and 0 electric charge respectively.

<sup>593</sup> The Lagrangian for the scalar Higgs field is

$$\mathcal{L}_H = (\partial_\mu \phi)^\dagger (\partial^\mu \phi) - V(\phi^\dagger \phi). \quad (2.15)$$

<sup>594</sup> Since the potential  $V(\phi^\dagger \phi)$  is constrained by  $\lambda > 0$ , the ground state is solely controlled by  
<sup>595</sup>  $\mu$ . If  $\mu^2 > 0$ , the ground state energy is  $\phi = 0$ , and the EW bosons would remain massless.  
<sup>596</sup> If  $\mu^2 < 0$ , the ground state is

$$|\phi|^2 = -\frac{\mu^2}{2\lambda} \equiv \frac{v^2}{\sqrt{2}}, \quad (2.16)$$

<sup>597</sup> where  $v$  is defined as the vacuum expectation value (VEV). The standard ground state for  
<sup>598</sup> the Higgs potential without loss of generality can be chosen as  $\phi(0) = 1/\sqrt{2}(0)_v$ .

<sup>599</sup> Having  $U(1)$  symmetry allows any  $-e^{i\theta} \sqrt{\mu^2/\lambda}$  to be a ground state energy for the Higgs

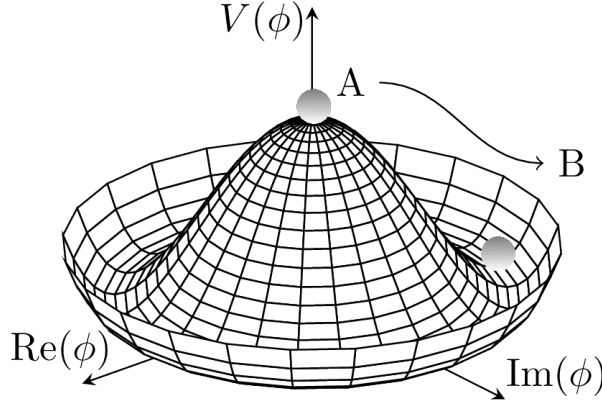


Figure 2.3: Illustration of a common representation of the Higgs potential [62]. Before SSB, the ground state  $\phi(0)$  is located at A which is symmetric with respect to the potential. A perturbation to this state fixes the ground state energy  $|\phi(0)|^2$  to a particular value at B, "spontaneously" breaking the symmetry and degeneracy in  $|\phi(0)|^2$ .

600 Lagrangian. This degeneracy results in spontaneous symmetry breaking of the  $SU(2)_L \times$   
 601  $U(1)_Y$  symmetry into  $U(1)_{\text{EM}}$  symmetry when the Higgs field settles on a specific vacuum  
 602 state as a result of a perturbation or excitation (Figure 2.3). The spontaneous symmetry  
 603 breaking introduces three massless (Nambu-Goldstone [63]) vector gauge boson  $\xi$  and a  
 604 massive scalar boson  $\eta$ , each corresponds to a generator of the gauge group. The vector field  
 605 for  $\xi$  and  $\eta$  are real fields parameterized as  $\xi \equiv \phi^+ \sqrt{2}$  and  $\eta \equiv \phi^0 \sqrt{2} - v$  [64]. The Higgs  
 606 field now becomes

$$\phi = \frac{v + \eta + i\xi}{\sqrt{2}} = \frac{1}{\sqrt{2}} e^{i\xi} \cdot \frac{\sigma}{2v} \begin{pmatrix} 0 \\ v + \eta \end{pmatrix}. \quad (2.17)$$

607 Due to  $U(1)_{\text{EM}}$  invariance, a unitary gauge with the transformation  $\phi \rightarrow \exp(-i\xi \cdot) \frac{\sigma}{2v}$  can  
 608 be chosen for the Higgs field to eliminate the massless bosons and incorporate them into the  
 609 EM/weak bosons via Equation 2.12. This leaves the massive  $\eta$  which can now be observed as  
 610 an excitation of the Higgs field from the standard ground state and must be the Higgs boson  
 611  $h$ . Using the EW covariant derivative from Equation 2.8, the Higgs Lagrangian around the

612 vacuum state becomes

$$\begin{aligned}\mathcal{L}_H &= (D_\mu \phi)^\dagger (D^\mu \phi) - \mu^2 \left( \frac{v+h}{\sqrt{2}} \right)^2 - \lambda \left( \frac{v+h}{\sqrt{2}} \right)^4 \\ &= (D_\mu \phi)^\dagger (D^\mu \phi) - \frac{1}{2} \mu^2 h^2 - \lambda v h^3 - \frac{\lambda}{4} h^4 - \dots\end{aligned}\tag{2.18}$$

613 The Higgs mass can be extracted from the quadratic term as  $m_H = \sqrt{-2\mu^2}$ . The kinetic

614 term in the Lagrangian can be written as

$$\begin{aligned}(D_\mu \phi)^\dagger (D^\mu \phi) &= \frac{1}{2} (\partial_\mu h)^2 + \frac{g^2}{8} (v+h)^2 \left| W_\mu^1 - i W_\mu^2 \right|^2 + \frac{1}{8} (v+h)^2 (g' W_\mu - g B_\mu) \\ &= \frac{1}{2} (\partial_\mu h)^2 + (v+h)^2 \left( \frac{g^2}{4} W_\mu^+ W^{-\mu} + \frac{1}{8} (g^2 + g'^2) Z_\mu^0 Z^{0\mu} \right).\end{aligned}\tag{2.19}$$

615 Masses for the EW bosons can be extracted from the quadratic terms

$$m_{W^\pm} = \frac{v}{2} g, \quad m_Z = \frac{v}{2} \sqrt{g^2 + g'^2}, \quad m_\gamma = 0.\tag{2.20}$$

616 However, the fermion mass term  $-m\bar{\psi}\psi$  still breaks EW invariance after spontaneous symmetry breaking. Instead, fermions acquire mass by replacing the mass term with a gauge invariant Yukawa term in the EW Lagrangian representing fermions' interactions with the 618 Higgs field [64]

$$\begin{aligned}\mathcal{L}_{\text{Yukawa}} &= -c_f \frac{v+h}{\sqrt{2}} (\bar{\psi}_R \psi_L + \bar{\psi}_L \psi_R) \\ &= -\underbrace{\frac{c_f}{\sqrt{2}} v (\bar{\psi} \psi)}_{\text{fermion mass}} - \underbrace{\frac{c_f}{\sqrt{2}} (h \bar{\psi} \psi)}_{\text{fermion-Higgs interaction}},\end{aligned}\tag{2.21}$$

620 where  $c_f$  is the fermion-Higgs Yukawa coupling. The fermion mass is then  $m_f = c_f v / \sqrt{2}$ .

## **621 2.2 Beyond the Standard Model: $t\bar{t}Z' \rightarrow t\bar{t}t\bar{t}$**

622 This analysis uses the  $t\bar{t}t\bar{t}$  final state signal signature to search for the existence of a heavy  
623 neutral BSM resonance that couples strongly to the top quark, nominally named  $Z'$ . Cross-  
624 section for  $t\bar{t}t\bar{t}$  production can be enhanced by many possible BSM models, in particular  
625 production of heavy scalars and pseudoscalar bosons predicted in Type-II two-Higgs-doublet  
626 models (2HDM) [39–43] or possible production of a heavy neutral resonance boson  $Z'(\rightarrow t\bar{t})$   
627 in association with a  $t\bar{t}$  pair [65, 66]. The  $t\bar{t}Z'$  production mode and consequently  $t\bar{t}t\bar{t}$  signal  
628 signature can provide a more sensitive channel for searches by avoiding contamination from  
629 the large SM  $gg \rightarrow t\bar{t}$  background in an inclusive  $Z' \rightarrow t\bar{t}$  search.

### **630 2.2.1 Top-philic vector resonance**

631 Many BSM models extend the SM by adding to the SM gauge group additional  $U(1)'$   
632 gauge symmetries [67, 68], each with an associated vector gauge boson ( $Z'$ ). In the case of  
633 a BSM global symmetry group with rank larger than the SM gauge group, the symmetry  
634 group can spontaneously break into  $G_{\text{SM}} \times U(1)'^n$ , where  $G_{\text{SM}}$  is the SM gauge group  
635  $SU(3)_C \times SU(2)_L \times U(1)_Y$  and  $U(1)'^n$  is any  $n \geq 1$  number of  $U(1)'$  symmetries. The  
636 existence of additional vector boson(s)  $Z'$  would open up many avenues of new physics e.g.  
637 extended Higgs sectors from  $U(1)'$  symmetry breaking [69, 70], existence of flavor-changing  
638 neutral current (FCNC) mediated by  $Z'$  [71], and possible exotic production from heavy  $Z'$   
639 decays [72].

640 Due to the top quark having the largest mass out of all known elementary particles in the  
641 SM, many BSM models [38–43, 73, 74] predict ‘top-philic’ vector resonances that have much  
642 stronger coupling to the top quark compared to other quarks. Previous BSM  $t\bar{t}t\bar{t}$  search for

643 top-philic resonances [28] with a similar model in the single-lepton final state and similar  
 644 mass ranges set upper limits on observed (expected)  $Z'$  production cross section between 21  
 645 (14) fb to 119 (86) fb depending on parameter choice. This analysis is also motivated by the  
 646 recent observation of SM  $t\bar{t}t\bar{t}$  production in the same-sign multilepton (SSML) channel by  
 647 ATLAS [44] and CMS [75] at  $6.1\sigma$  and  $5.6\sigma$  discovery significance respectively.

648 A simplified color-singlet vector particle model [45, 73] is employed in the search. The  
 649 interaction Lagrangian assumes only  $Z'$  to top coupling and has the form

$$\begin{aligned}
 \mathcal{L}_{Z'} &= \bar{t}\gamma_\mu (c_L P_L + c_R P_R) t Z'^\mu \\
 &= c_t \bar{t}\gamma_\mu (\cos\theta P_L + \sin\theta P_R) t Z'^\mu,
 \end{aligned} \tag{2.22}$$

650 where  $c_t = \sqrt{c_L^2 + c_R^2}$  is the  $Z'$ -top coupling strength,  $P_{L/R} = (1 \mp \gamma_5)/2$  are the chirality  
 651 projection operators, and  $\theta = \tan^{-1}(c_R/c_L)$  is the chirality mixing angle. Expanding the  
 652 Lagrangian results in

$$\mathcal{L}_{Z'} = \frac{1}{\sqrt{2}} \bar{t}\gamma_\mu \left[ \sin\left(\theta + \frac{\pi}{4}\right) - \left( \sqrt{2} \cos\left(\theta + \frac{\pi}{4}\right) \right) \gamma_5 \right] t Z'^\mu, \tag{2.23}$$

653 which bears striking resemblance to the EW Lagrangian neutral current interaction term in  
 654 Equation 2.13, showing the similarity between the  $Z'$  and the  $Z$  boson that acquires mass  
 655 from  $SU(2)_L \times U(1)_Y$  spontaneous symmetry breaking. Assuming the  $Z'$  mass  $m_{Z'}$  is much  
 656 larger than the top mass ( $m_t^2/m_{Z'}^2 \approx 0$ ), the  $Z'$  decay width at leading-order (LO) can be  
 657 approximated as

$$\Gamma(Z' \rightarrow t\bar{t}) \approx \frac{c_t^2 m_{Z'}}{8\pi}. \tag{2.24}$$

658 It can be observed that  $\Gamma/m_{Z'} \approx c_t^2/8\pi \ll 1$  for  $c_t \approx 1$ , which suggests a very narrow and

659 well-defined resonance peak, validating the narrow-width approximation for the choice of  
 660  $c_t = 1$ .

### 661 2.2.2 Production channels

662 The main production channels for the aforementioned heavy topophilic color singlet  $Z'$   
 663 are at tree level and loop level, with the one-loop level being the dominant processes [45].  
 664 Loop level processes are dependent on the chirality angle  $\theta$ , where  $\theta = \pi/4$  suppresses all  
 665 but gluon-initiated box sub-processes. To minimize model dependence, only the tree level  
 666 production was considered for this analysis by choosing  $\theta = \pi/4$ . Figure 2.4 illustrates  
 667 several tree level  $Z'$  production processes.

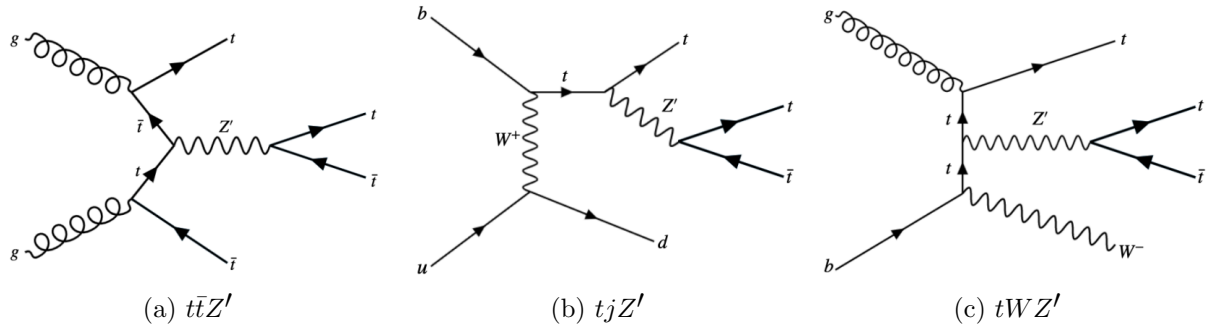


Figure 2.4: Feynman diagrams for tree level  $Z'$  production in association with (a)  $t\bar{t}$ , (b)  $tj$  (light quark) and (c)  $tW$ , decaying to final states containing (a)  $t\bar{t}\bar{t}\bar{t}$  or (b)(c)  $t\bar{t}t$  [45].

668 The tree level  $t\bar{t}$ -associated process  $t\bar{t}Z'$  is the targeted production channel for the search  
 669 in this dissertation. Contributions from the single-top-associated channels  $tjZ'$  and  $tWZ'$   
 670 are not considered due to a smaller cross-section by a factor of two compared to  $t\bar{t}Z'$  due  
 671 to suppression in the three-body phase space [45]. Additionally,  $t\bar{t}Z' \rightarrow t\bar{t}t\bar{t}$  production is  
 672 independent of  $\theta$  while  $tjZ'$  and  $tWZ'$  are minimally suppressed under pure left-handed  
 673 interactions ( $\theta = 0$ ) and maximally suppressed under pure right-handed interactions ( $\theta =$   
 674  $\pi/2$ ); both channels are affected by the choice of  $\theta = \pi/4$  to suppress loop level production.

675    **2.2.3 Decay modes**

676    The different  $W$  boson decay modes  
677    shown in Figure 2.2 result in many differ-  
678    ent final states for  $t\bar{t}Z'/t\bar{t}\bar{t}$  decay, which  
679    can each be classified into one of three chan-  
680    nels shown in Figure 2.5: all hadronic de-  
681    cays; exactly one lepton or two opposite-sign  
682    leptons (1LOS); exactly two same-sign lep-  
683    tons or three or more leptons (SSML). The  
684    branching ratio for each channel is shown  
685    in Figure 2.5. The all hadronic and 1LOS  
686    channels have much larger branching ratios  
687    compared to SSML channel but suffer heavily from  $gg \rightarrow t\bar{t}$  background contamination,  
688    giving the SSML channel better sensitivity at the cost of lower statistics. This is also the  
689    targeted channel for this analysis.

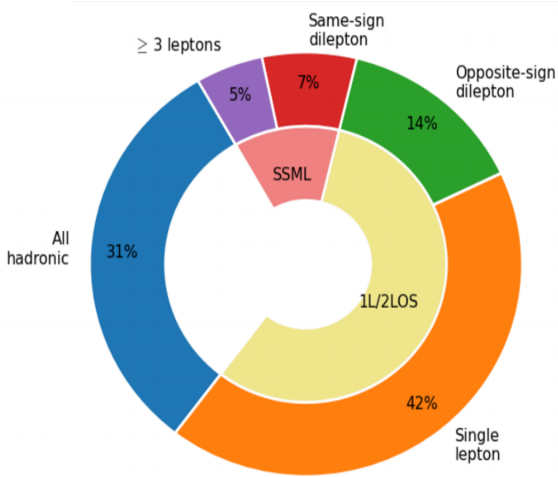


Figure 2.5: Branching ratios for  $t\bar{t}t\bar{t}$  decay [76]. The same-sign dilepton and multilepton chan-  
nels together forms the SSML channel.

# 690 Chapter 3. LHC & ATLAS Experiment

## 691 3.1 The Large Hadron Collider

692 Predictions from theoretical models are evaluated against experimental data collected  
693 from particle detectors. This chapter provides a detailed overview of the Large Hadron  
694 Collider (LHC) and the ATLAS detector, one of the key experiments designed to study  
695 high-energy collisions at the LHC.

### 696 3.1.1 Overview

697 The Large Hadron Collider [77] (LHC) is currently the world's largest particle collider  
698 with a circumference of almost 27 km. Built by CERN on the border of Switzerland and  
699 France, the LHC is designed as a particle collider for proton-proton ( $pp$ ), sometimes heavy  
700 ions i.e. lead-lead (PbPb) and proton-lead ( $pPb$ ) beams at TeV-scale energies. Two beams  
701 of particles are injected into the LHC in opposite directions and allowed to collide at the  
702 center of four major experiments:

- 703 • **A Toroidal LHC ApparatuS** (ATLAS) [27] and **Compact Muon Solenoid** (CMS)  
704 [78]: multi-purpose detectors, designed to target a variety of phenomena including SM,  
705 BSM and heavy-ion physics.
- 706 • **Large Ion Collider Experiment** (ALICE) [79]: specialized detector to record ion  
707 collisions and study heavy-ion physics.
- 708 • **Large Hadron Collider beauty** (LHCb) [80]: detector dedicated to study properties  
709 of  $b$ -quarks and  $b$ -hadrons.

710      Aside from the four major experiments, the LHC also houses smaller experiments e.g.  
 711     AWAKE [81], FASER [82], KATRIN [83], that either share an interaction point with one of  
 712     the above experiments or make use of particle beams pre-LHC injection.

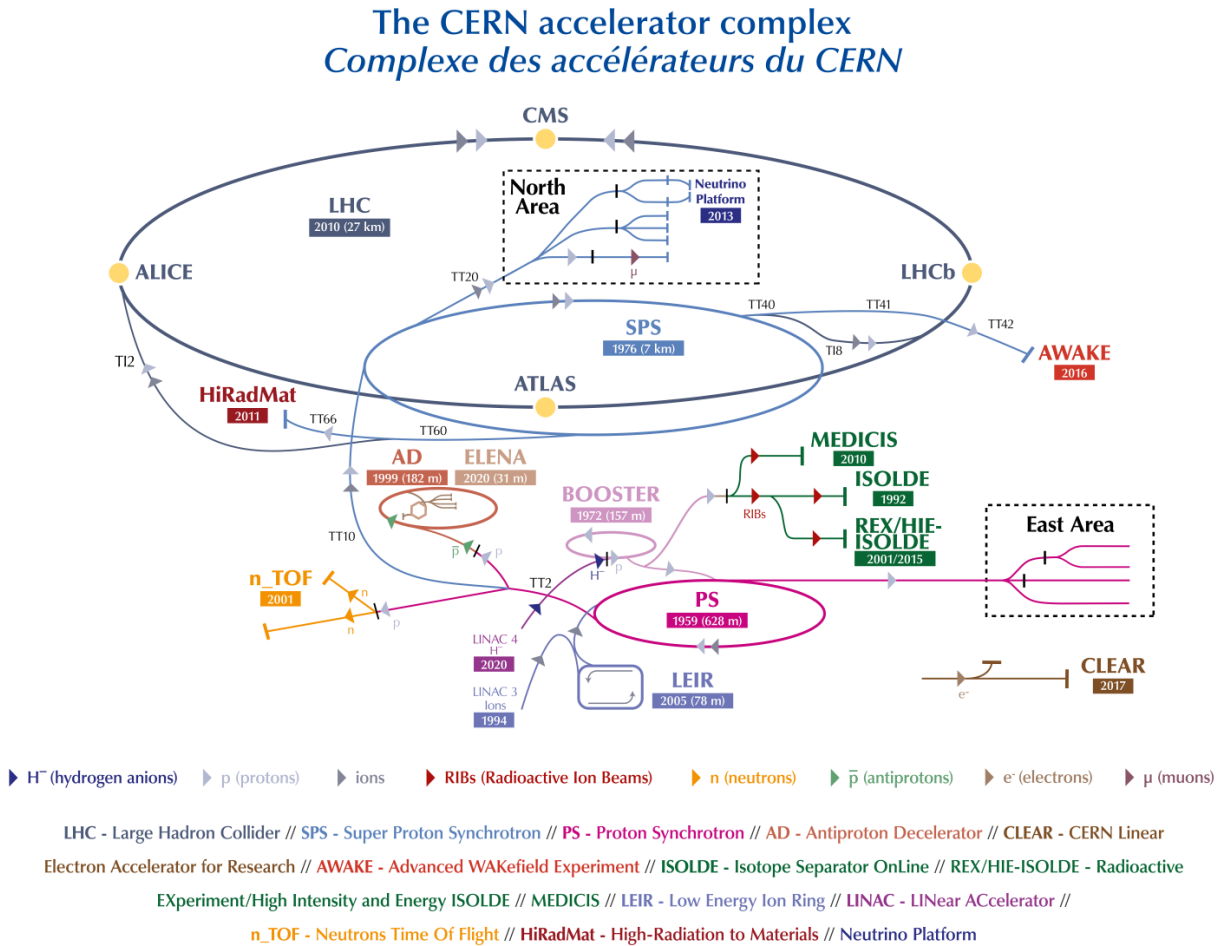


Figure 3.1: The full CERN accelerator complex as of 2022 [84].

713      The majority of the LHC operational time is dedicated to studying  $pp$  collisions of up to  
 714      $\sim 13$  TeV center-of-mass energy, denoted as  $\sqrt{s}$ . Reaching collision energy requires a sequence  
 715     of accelerators within the CERN accelerator complex, shown in Figure 3.1. Proton produc-  
 716     tion starts at LINAC 4, where hydrogen atoms are accelerated to 160 MeV then stripped  
 717     of electrons. The leftover proton beams are injected into the Proton Synchrotron Booster

718 (PSB) and accelerated to 2 GeV before being transferred into the Proton Synchrotron (PS).  
 719 Here, the beams are ramped up to 26 GeV then injected into the Super Proton Synchrotron  
 720 (SPS) to further raise the energy threshold to 450 GeV. The beams are finally injected into  
 721 the LHC in opposite directions, continuously increasing in energy up to 6.5 TeV per beam,  
 722 reaching the 13 TeV center-of-mass energy threshold necessary for collision during Run 2.  
 723 As of the start of Run 3 in 2022, proton beams can now be ramped up to 6.8 TeV per beam  
 724 for a total of  $\sqrt{s} = 13.6$  TeV.

### 725 3.1.2 LHC operations

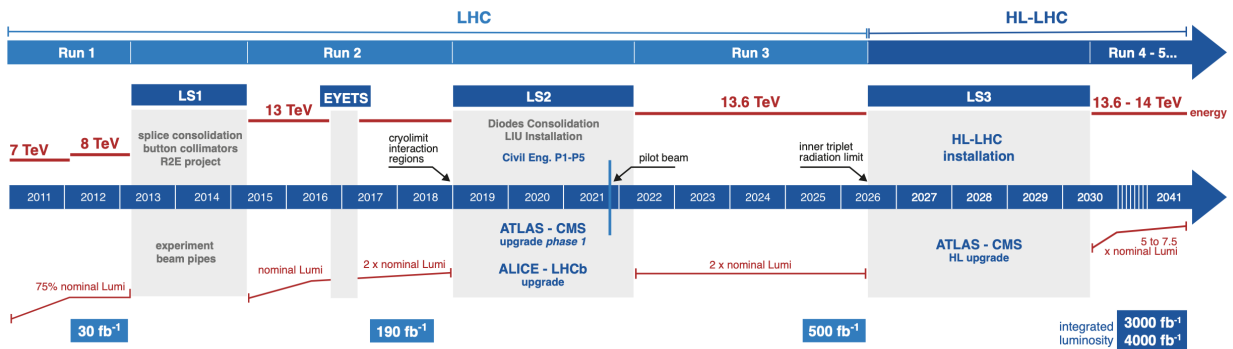


Figure 3.2: Current and future timeline of LHC operations with corresponding center-of-mass energies and projected integrated luminosities. [85].

726 Operations at the LHC are defined in periods of data-taking and shut-down known as  
 727 runs and long shutdowns respectively; the first period (Run 1) started with first collisions  
 728 at the LHC in 2010 at  $\sqrt{s} = 7$  TeV [86]. Upgrades are usually carried out for detectors and  
 729 accelerators during long shutdowns, raising the maximum energy threshold in preparation  
 730 for the next run. An overview of the LHC runtime and corresponding center-of-mass energies  
 731 are summarized in Figure 3.2. During Run 2 from 2015-2018, the ATLAS detector recorded  
 732 a total of  $1.1 \times 10^{16}$   $pp$  collisions at  $\sqrt{s} = 13$  TeV, which corresponds to an integrated

733 luminosity of  $140 \pm 0.83\% \text{ fb}^{-1}$  that passed data quality control and are usable for analyses  
734 [87]. This is also the data set used for the analysis in this dissertation.

### 735 3.1.3 Physics at the LHC

736 The majority of physics studied at the LHC focus primarily on QCD proton-proton hard  
737 scattering processes and the resulting products. Hard scattering processes involve large  
738 momentum transfer compared to the proton mass e.g. top pair production ( $gg \rightarrow t\bar{t}$ ) and  
739 Higgs production ( $gg \rightarrow H$ ), and can be predicted using perturbative QCD [88]. Hard  
740 processes probe distance scales much lower than the proton radius and can be considered  
741 collisions between the constituent quarks and gluons i.e. partons. Soft processes involve  
742 lower momentum transfer between partons and are dominated by less well-understood non-  
743 perturbative QCD effects. The hard interaction between two partons are represented by a  
744 parton distribution function (PDF)  $f_i(x, Q^2)$ , which describes the probability of interacting  
745 with a constituent parton  $i$  that carries a fraction  $x$  of the external hadron's momentum  
746 when probed at a momentum scale of  $Q^2$  [89]. Other partons within the hadron that did  
747 not participate in the collision can still interact via lower momentum underlying-events  
748 (UE). The probability of a particular interaction occurring is defined as its cross-section  
749  $\sigma[b]$ . Figure 3.3 gives an overview of SM processes produced within the LHC and their  
750 cross-sections.

## 751 3.2 The ATLAS detector

752 One of the four main experiments at the LHC is ATLAS [27], designed as a multi-purpose  
753 detector for the role of studying high-energy physics in  $pp$  and heavy-ion collisions. ATLAS

## Standard Model Production Cross Section Measurements

Status: October 2023

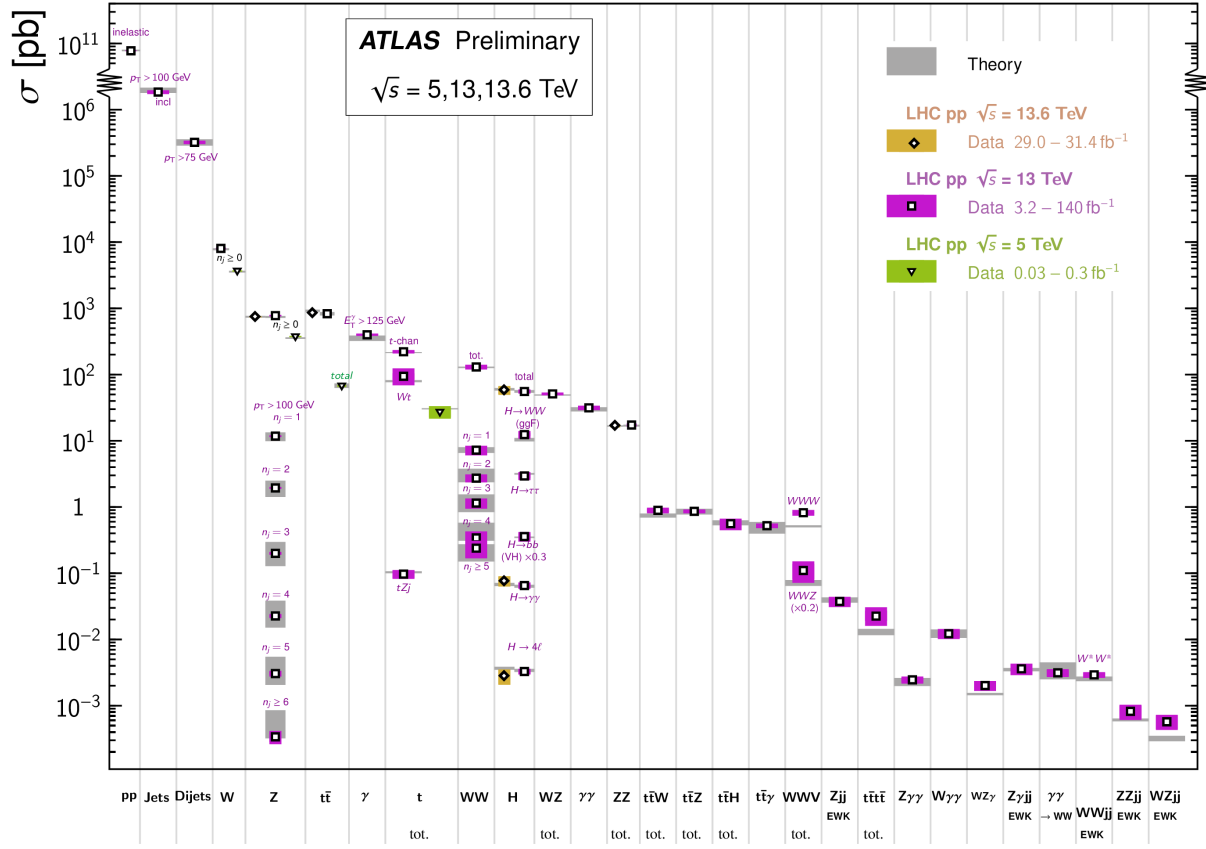


Figure 3.3: Summary of predicted and measured cross-section for SM processes at the LHC at different center-of-mass energies [90].

754 is a detector with symmetric cylindrical geometry with dimensions of 44 m in length and 25  
 755 m in diameter, covering a solid angle of almost  $4\pi$  around the collision point. The detector is  
 756 built concentrically around the beamline with the collision point at the center to maximally  
 757 capture signals produced by interactions. Figure 3.4 shows a slice of the ATLAS detector.  
 758 From the inside out, the main ATLAS subdetector system consists of the inner detector  
 759 (ID), calorimeter systems (electromagnetic and hadronic) and the muon spectrometer (MS).  
 760 The ATLAS detector uses a right-handed coordinate system [27] designed to align with  
 761 the geometry of a collision interaction, with the origin set at the interaction point, the  $z$ -axis

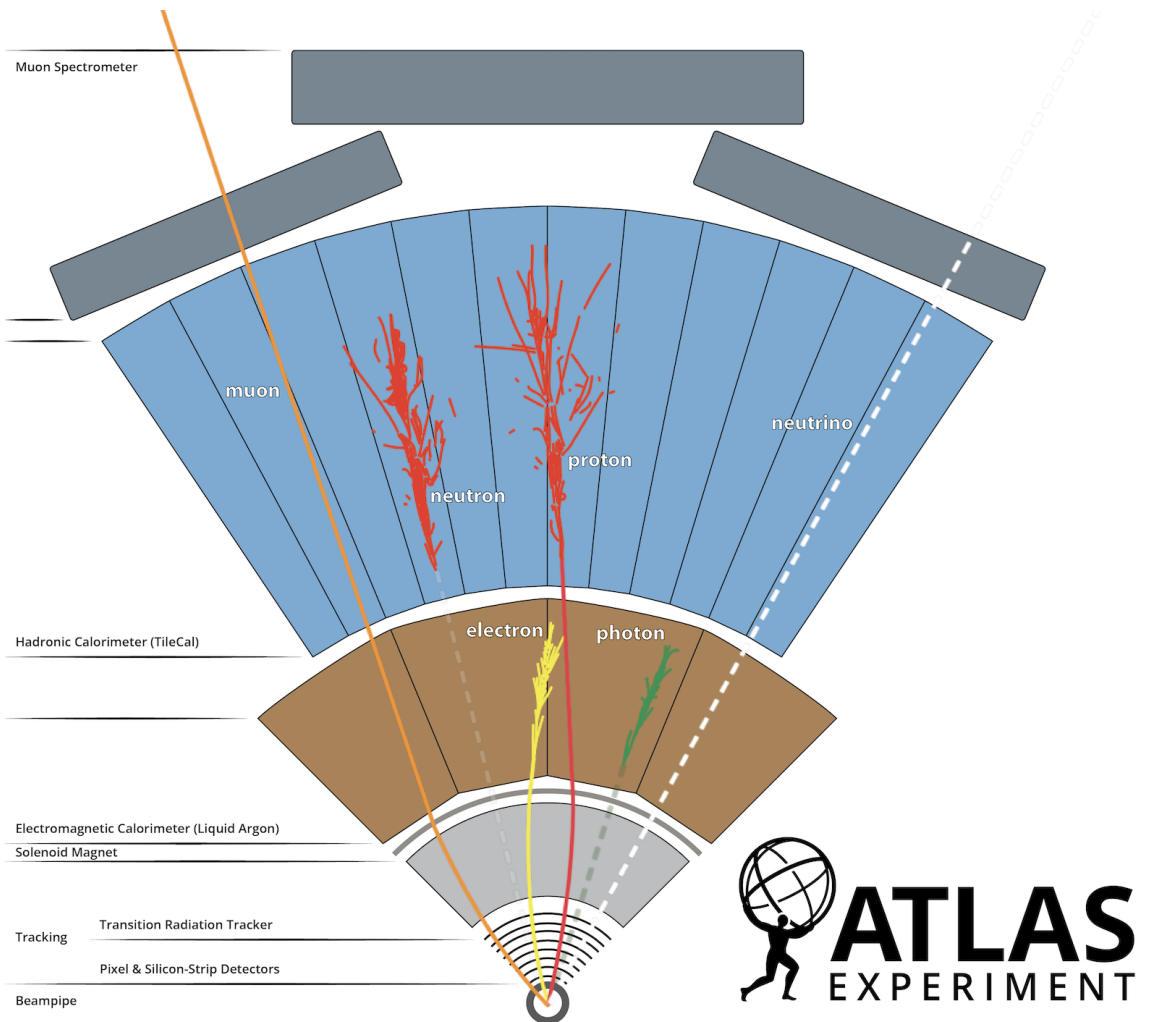


Figure 3.4: A cross section slice of the ATLAS detector showing different subsystems along with visualization of different types of particles traveling through the detector [91].

following (either of) the beamline and the  $x$ -axis pointing towards the center of the LHC ring. In cylindrical coordinates, the polar angle  $\theta$  is measured from the beam axis, and the azimuthal angle  $\phi$  is measured along the transverse plane ( $xy$ -plane) starting at the  $x$ -axis. Additional observables are defined for physics purposes: the pseudorapidity defined as  $\eta = -\ln \tan(\theta/2)$ ; angular distance within the detector defined as  $\Delta R = \sqrt{\Delta\eta^2 + \Delta\phi^2}$ ; and transverse momentum  $p_T$  (transverse energy  $E_T$ ) defined as the component of the particle's momentum (energy) projected onto the transverse plane.

### 769 3.2.1 Inner detector

770 The innermost part of ATLAS is the inner detector (ID) [27], constructed primarily for  
771 the purpose of measuring and reconstructing charged tracks within the  $|\eta| < 2.5$  region with  
772 high momentum resolution ( $\sigma_{p_T}/p_T = 0.05\% \pm 1\%$ ). Figure 3.5 shows the composition of  
773 the ID with three subsystems, the innermost being the pixel detector, then Semiconductor  
774 Tracker (SCT), and the Transition Radiation Tracker (TRT) on the outermost layer; all of  
775 which are surrounded by a solenoid magnet providing a magnetic field of 2 T.

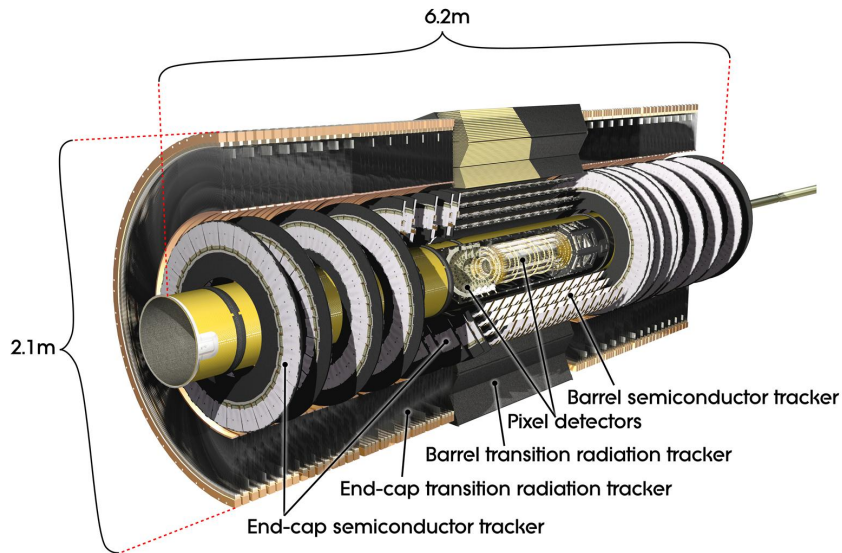


Figure 3.5: Cutaway illustration of the inner detector along with its subsystems [92].

### 776 Pixel detector

777 The pixel detector subsystem [27] consists of 250  $\mu\text{m}$  silicon semiconductor pixel layers  
778 with about 80.4 million readout channels, reaching a spatial resolution of 10  $\mu\text{m}$  in the  
779  $R - \phi$  (transverse) plane and 115  $\mu\text{m}$  in the  $z$ -direction for charged tracks. Charged particles  
780 passing through the pixel detector ionize the silicon layers and produce electron-hole pairs;

781 the electrons drift towards the detector's electrode under an applied electric field and the  
782 resulting electric signals are collected in read-out regions. The pixel detector is used primarily  
783 for impact parameter measurement, pile-up suppression, vertex finding and seeding for track  
784 reconstruction.

### 785 Semiconductor Tracker

786 The Semiconductor Tracker (SCT) [27] functions similarly to the pixel detector, using  
787 silicon semiconductor microstrips totaling about 6.3 million read-out channels, reaching a  
788 per layer resolution of 17  $\mu\text{m}$  in the  $R\text{-}\phi$  plane and 580  $\mu\text{m}$  in the  $z$ -direction [27]. The  
789 SCT plays an important role in precise  $p_{\text{T}}$  measurement of charged particles as well as track  
790 reconstruction.

### 791 Transition Radiation Tracker

792 The outermost layer of the ID, the Transition Radiation Tracker (TRT) [27], consists of  
793 layers of 4 mm diameter straw tubes filled with a xenon-based gas mixture and a 30  $\mu\text{m}$   
794 gold-plated wire in the center. The TRT contains a total of about 351 thousand readout  
795 channels with a resolution of 130  $\mu\text{m}$  for each straw tube in the  $R\text{-}\phi$  plane, and provides  
796 extended track measurement, particularly estimation of track curvature under the solenoidal  
797 magnetic field. Importantly, the TRT also serves to identify electrons through absorption of  
798 emitted transition-radiation within the Xe-based gas mixture.

### 799 3.2.2 Calorimeter systems

800 Surrounding the ID is the ATLAS calorimeter system [27] with electromagnetic (EM) and  
801 hadronic calorimeters, covering a range of  $|\eta| < 4.9$ . The calorimeters are sampling calorime-

802 ters with alternating absorbing layers to stop incoming particles and active layers to collect  
 803 read-out signals from energy deposits. Incoming particles passing through the calorimeters  
 804 interact with the absorbing layers, producing EM or hadronic showers of secondary particles.  
 805 The particle showers deposit energy in the corresponding layer of the calorimeters, which  
 806 are collected and aggregated to identify and reconstruct the original particle's energy and  
 807 direction. Figure 3.6 shows a schematic overview of the ATLAS calorimeter system.

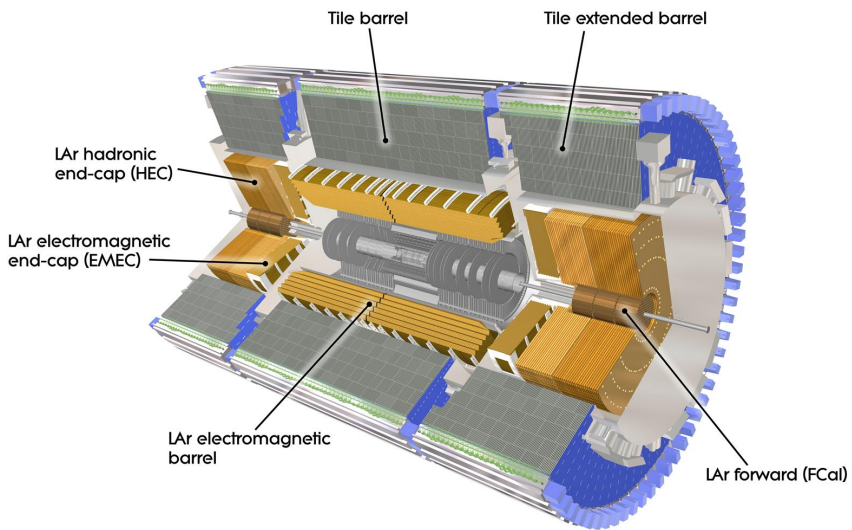


Figure 3.6: Cutaway illustration of the calorimeter system including the EM, hadronic and LAr forward calorimeters [93].

## 808 Electromagnetic calorimeter

809 The EM calorimeter [27] covers the innermost part of the calorimeter system, with lead  
 810 (Pb) absorbing layers and liquid argon (LAr) active layers to capture the majority of electrons  
 811 and photons exiting the ID. The EM calorimeter is divided into regions depending on  $\eta$   
 812 coverage: a barrel region ( $|\eta| < 1.475$ ), two endcap regions ( $1.375 < |\eta| < 3.2$ ) and a  
 813 transition region ( $1.372 < |\eta| < 1.52$ ). The endcap calorimeters are further divided into an

814 outer wheel region ( $1.372 < |\eta| < 2.5$ ) and an inner wheel region ( $2.5 < |\eta| < 3.2$ ) in order  
815 to provide precise coverage within the same  $\eta$  range as the ID. Overlap between the barrel  
816 and endcap regions compensates for the lower material density in the transition region.

817 **Hadronic calorimeter**

818 The hadronic calorimeter [27] covers up to  $|\eta| < 4.9$  and is comprised of three parts: the  
819 tile calorimeter with a barrel region ( $|\eta| < 1.0$ ) and extended barrel regions ( $0.8 < |\eta| < 1.7$ );  
820 the hadronic endcap calorimeter (HEC) covering  $1.5 < |\eta| < 3.2$ ; and the forward calorimeter  
821 (FCal) covering  $3.2 < |\eta| < 4.9$ . The tile calorimeter covers the EM calorimeter barrel region  
822 and uses steel as material for the absorbing layers with scintillating tiles for the active layers.  
823 Signals captured by scintillating tiles are read out from both sides using photomultiplier  
824 tubes. The HEC calorimeter covers the endcap regions of the EM calorimeter and uses a  
825 copper-LAr calorimeter layer scheme. The FCal is located close to the beamline providing  
826 coverage for particles traveling close to parallel with the beam axis. The subdetector contains  
827 three modules: one with copper absorbing layers optimized for EM measurements, and two  
828 with tungsten absorbing layers targeting hadronic cascades. All modules in the FCal use  
829 LAr as the active layer.

830 **3.2.3 Muon spectrometer**

831 Generally, the only particles that penetrate past the calorimeter layer are muons and  
832 neutrinos. The muon spectrometer (MS) [27] is situated on the outermost of the ATLAS  
833 detector and aims to track and measure muons within  $|\eta| < 2.7$ . The MS utilizes an array of  
834 toroid magnets to provide a magnetic field perpendicular to the muon trajectory, bending  
835 the track in order to measure its curvature. The magnetic field is powered by a large barrel

836 toroid ( $|\eta| < 1.4$ ) with strength of 0.5 T and two endcap toroid magnets ( $1.6 < |\eta| < 2.7$ ) of  
837 1 T. Both types contribute to the magnetic field in the transition region ( $1.4 < |\eta| < 1.6$ ).

838 To measure the muon itself, four types of large gas-filled chambers known as muon cham-  
839 bers [27] are designed and constructed for two main goals: triggering on potential muon  
840 candidates entering the MS and tracking their trajectories through the detector with high  
841 precision. The tracking system include Monitored Drift Tubes (MDTs), which record muon  
842 track information over the entire MS  $\eta$  range ( $|\eta| < 2.7$ ). The MDTs are built with multi-  
843 ple layers of drift tubes and filled with a mixture of 93% Ar and 7% CO<sub>2</sub>. Muons passing  
844 through drift tubes in the MDT ionize the gas within each tube; signals are then recorded  
845 as freed electrons drift to read-out channels under an applied electric field. In the forward  
846 region ( $2.0 < |\eta| < 2.7$ ), Cathode Strip Chambers (CSCs) are included along with MDTs.  
847 The CSCs are multiwire proportional chambers built with higher granularity and shorter  
848 drift time than the MDTs to handle tracking in an environment with high background rates

849 .

850 The MS trigger system includes Resistive Plate Chambers (RPCs) [27], which provide  
851 triggering in the barrel region ( $|\eta| < 1.05$ ) using parallel electrode plates made of resistive  
852 materials with a gas mixture inbetween. High voltage is applied to the plates, accelerat-  
853 ing the electrons freed from ionized gas and creating a fast avalanche of charge, which is  
854 collected on external read-out strips almost instantaneously. Triggering and coarse position  
855 measurements in the endcap region ( $1.05 < |\eta| < 2.5$ ) is handled by Thin-Gap Chambers  
856 (TGCs). Similar to CSCs, TGCs are multiwire proportional chambers with a small wire gap  
857 ("thin-gap") and high applied voltage across the gap, resulting in fast response time giving  
858 TGCs the capabilities to identify muon candidates in real time.

859 **3.2.4 Trigger & data acquisition**

860 The LHC produces a colossal amount of collision data at a bunch crossing rate of 40 MHz  
861 with bunch spacing of 25 ns. The ATLAS Trigger and Data Acquisition (TDAQ) system [94]  
862 synchronously identifies and records interesting events for in-depth analysis. The ATLAS  
863 trigger system in Run 2 consists of two steps: Level-1 (L1) trigger and High-Level Trigger  
864 (HLT). Events failing any step in the trigger chain are permanently lost.

865 The L1 trigger hardware is divided into L1 calorimeter triggers (L1Calo) and L1 muon  
866 triggers (L1Muon) [94]. L1Calo trigger uses information from ATLAS calorimeter system  
867 to quickly identify signs of high  $p_T$  objects e.g. EM clusters, jets and missing transverse  
868 energy  $E_T^{\text{miss}}$  (section 4.4). Similarly, L1Muon uses information from the RPCs and TGCs  
869 of the MS to make quick decisions on potentially interesting muon candidates. Outputs  
870 from L1Calo and L1Muon are fed into the L1 topological trigger (L1Topo) for additional  
871 filtering based on event topology and multi-object correlation, allowing for more selective  
872 and physics-motivated triggering. Decisions from all three types of L1 triggers are provided  
873 as inputs for the Central Trigger Processor (CTP) for a final Level-1 Accept (L1A) decision.

874 The entire L1 trigger chain results in a 2.5  $\mu\text{s}$  latency and reduces the event rate to 100 kHz.

875 Events passing L1 triggers are sent to HLTs before being saved to offline storage at  
876 CERN data centers. HLTs are software-based triggers used for more complex and specific  
877 selections on physics objects required by targeted analysis goals, in turn requiring more  
878 computing power with longer latency. After HLT selections, the event rate is reduced to 1  
879 kHz on average [94]. Overall, the full trigger chain reduces the event rate for ATLAS by  
880 approximately a factor of  $4 \times 10^4$ .

# 881 Chapter 4. Particle Reconstruction & Identifi- 882 fication

883 Activity within the ATLAS detector is recorded as raw electronic signals, which can  
884 be utilized by ATLAS reconstruction software to derive physics objects for analysis. This  
885 chapter describes the reconstruction and identification of basic objects (e.g. interaction  
886 vertices, tracks, topological clusters of energy deposits) and subsequently of complex physics  
887 objects i.e. particles and particle signatures.

## 888 4.1 Primary reconstruction

### 889 4.1.1 Tracks

890 Charged particles traveling through the ATLAS detector deposit energy in different layers  
891 of the ID and MS. The ID track reconstruction software consists of two algorithm chains:  
892 inside-out and outside-in track reconstruction [95–97].

893 The inside-out algorithm is primarily used for the reconstruction of primary particles  
894 i.e. particles directly produced from  $pp$  collisions or decay products of short-lived particles.

895 The process starts by forming space points from seeded hits in the silicon detectors within  
896 the pixel & SCT detectors. Hits further away from the interaction vertex are added to  
897 the track candidate using a combinatorial Kalman filter [98] pattern recognition algorithm.

898 Track candidates are then fitted with a  $\chi^2$  filter [99] and loosely matched to a fixed-sized  
899 EM cluster. Successfully matched track candidates are re-fitted with a Gaussian-sum filter  
900 (GSF) [100], followed by a track scoring strategy to resolve fake tracks & hit ambiguity

901 between different tracks [101]. The track candidate is then extended to the TRT to form  
902 final tracks satisfying  $p_T > 400$  MeV. The outside-in algorithm handles secondary tracks  
903 mainly produced from long-lives particles or decays of primary particles by back-tracking  
904 from TRT segments, which are then extended inward to match silicon hits in the pixel and  
905 SCT detectors to form track reconstruction objects.

### 906 4.1.2 Vertices

907 Vertices represent the point of interaction or decay for particles within the ATLAS de-  
908 tector. Primary vertices (PVs) are defined as the point of collision for hard-scattering  $pp$   
909 interactions, while secondary or displaced vertices result from particle decays occurring at a  
910 distance from its production point.

911 Reconstruction of PVs is crucial to accurately profile the kinematic information of an  
912 event and form a basis for subsequent reconstruction procedures. Primary vertex recon-  
913 struction occurs in two stages: vertex finding and vertex fitting [102]. The vertex finding  
914 algorithm uses the spatial coordinates of reconstructed tracks to form the seed for a vertex  
915 candidate. An adaptive vertex fitting algorithm [103] then iteratively evaluates track-vertex  
916 compatibility to estimate a new best vertex position. Less compatible tracks are down-  
917 weighted in each subsequent iteration, and incompatible tracks are removed and can be  
918 used for another vertex seed; the process is repeated until no further PV can be found.  
919 All reconstructed vertices without at least two matched tracks are considered invalid and  
920 discarded.

921 Secondary vertex reconstruction uses the Secondary Vertex Finder (SVF) algorithm [104]  
922 which is primarily designed to reconstruct  $b$ - and  $c$ -hadrons for flavor tagging purposes. The  
923 SVF aims to reconstruct one secondary vertex per jet and only considers tracks that are

924 matched to a two-track vertex and contained within a  $p_T$ -dependent cone around the jet  
925 axis. The tracks are then used to reconstruct a secondary vertex candidate using an iterative  
926 process similar to the PV vertex fitting procedure.

927 **Pile-up**

928 At high luminosities, multiple interactions can be associated with one bunch crossing,  
929 resulting in many PVs. The effect is called pile-up [105], and usually result from soft QCD  
930 interactions. Pile-up can be categorized into two types: in-time pile-up, stemming from  
931 additional  $pp$  collisions in the same bunch crossing that is not the hard-scatter process; out-  
932 of-time pile-up, resulting from leftover energy deposits in the calorimeters from other bunch  
933 crossings.

934 **4.1.3 Topological clusters**

935 Topological clusters (topo-clusters) [106] consist of clusters of spatially related calorimeter  
936 cell signals. Topo-clusters are primarily used to reconstruct hadron- and jet-related objects  
937 in an effort to extract signal while minimizing electronic effects and physical fluctuations, and  
938 also allow for recovery of energy lost through bremsstrahlung or photon conversions. Cells  
939 with signal-to-noise ratio  $\zeta_{\text{cell}}^{\text{EM}}$  passing a primary seed threshold are seeded into a dynamic  
940 topological cell clustering algorithm as part of a proto-cluster. Neighboring cells satisfying a  
941 cluster growth threshold are collected into the proto-cluster. If a cell is matched to two proto-  
942 clusters, the clusters are merged. Two or more local signal maxima in a cluster satisfying  
943  $E_{\text{cell}}^{\text{EM}} > 500 \text{ MeV}$  suggest the presence of multiple particles in close proximity, and the cluster  
944 is split accordingly to maintain good resolution of the energy flow. The process continues  
945 iteratively until all cells with  $\zeta_{\text{cell}}^{\text{EM}}$  above a principal cell filter level have been matched to a

946 cluster.

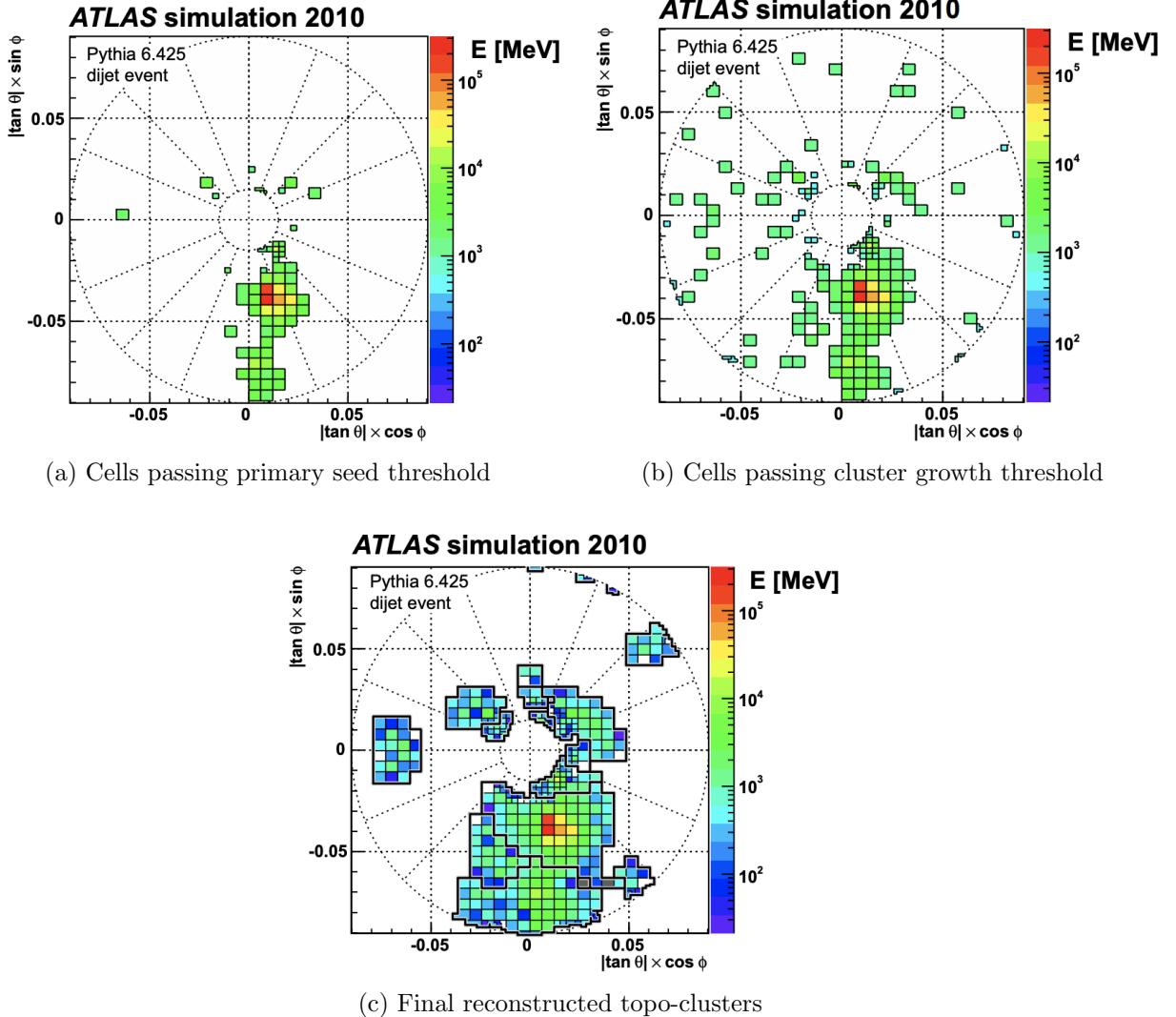


Figure 4.1: Stages of topo-cluster formation corresponding to each threshold. In (a), proto-clusters are seeded from cells with adequate signal significance  $\zeta_{\text{cell}}^{\text{EM}}$ . The clusters are further merged and split in (b) following a predefined cluster growth threshold. The process stops in (c) when all sufficiently significant signal hits have been matched to a cluster [106].

## 947 4.2 Jets

948 Quarks, gluons and other hadrons with non-neutral color charge cannot be observed  
949 individually due to QCD color confinement, which forces a non-color-neutral hadron to

almost immediately undergo hadronization, producing a collimated cone of color-neutral hadrons defined as a jet. Jet signals can be used to reconstruct and indirectly observe the quarks or gluons from which the jet originated in the original hard-scattering process.

### 4.2.1 Jet reconstruction

The ATLAS jet reconstruction pipeline is largely carried out using a particle flow (PFlow) algorithm combined with an anti- $k_t$  jet clustering algorithm. The PFlow algorithm [107] utilizes topo-clusters along with information from both the calorimeter systems and the ID in order to make use of the tracker system’s advantages in low-energy momentum resolution and angular resolution. First, the energy from charged particles is removed from the calorimeter topo-clusters; then, it is replaced by particle objects created using the remaining energy in the calorimeter and tracks matched to topo-clusters. The ensemble of “particle flow objects” and corresponding matched tracks are used as inputs for the iterative anti- $k_t$  algorithm [108].

The main components of the anti- $k_t$  algorithm involve the distance  $d_{ij}$  between two jet candidates  $i$  and  $j$ , and the distance  $d_{iB}$  between the harder jet candidate of the two (defined as  $i$ ) and the beamline  $B$ . If  $d_{ij} < d_{iB}$ , then the two jet candidates are combined and returned to the pool of candidates; otherwise, jet candidate  $i$  is considered a jet and removed from the pool. The distance  $d_{ij}$  is inversely proportional to a predefined radius parameter  $\Delta R$  in order to control reconstruction quality for small- $R$  and large- $R$  jets. This analysis uses  $\Delta R = 0.4$  to better handle heavily collimated small- $R$  jets resulting from parton showers.

The anti- $k_t$  jets so far have only been reconstructed at the EM level and need to be calibrated to match the energy scale of jets reconstructed at particle level. This is done via a MC-based jet energy scale (JES) calibration sequence, along with further calibrations

973 to account for pile-up effects and energy leakage. The full JES calibration sequence is  
 974 shown in Figure 4.2. All calibrations except origin correction are applied to the jet's four-  
 975 momentum i.e. jet  $p_T$ , energy and mass. Afterwards, a jet energy resolution (JER) [109]  
 976 calibration step is carried out in a similar manner to JES to match the resolution of jets in  
 977 dijet events. To further suppress pile-up effects, a neural-network based jet vertex tagger  
 978 (NNJvt) discriminant was developed based on the previous jet vertex tagger (JVT) algorithm  
 979 [105] and applied to low- $p_T$  reconstructed jets.

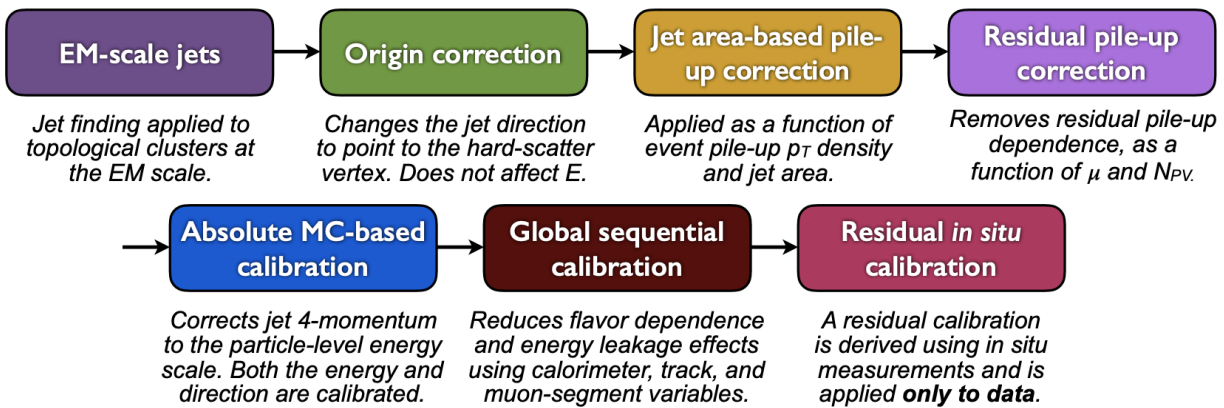


Figure 4.2: Jet energy scale calibration sequence for EM-scale jets [110].

### 980 4.2.2 Flavor tagging

981 Identifying and classifying hadronic jets are important tasks for ATLAS physics, for  
 982 example analyses involving Higgs decays  $H \rightarrow b\bar{b}$  or top quarks. Flavor tagging or  $b$ -tagging  
 983 is the process of identifying jets containing  $b$ -hadrons,  $c$ -hadrons, light-hadrons ( $uds$ -hadrons)  
 984 or jets from hadronically decaying  $\tau$  leptons. Distinguishing  $b$ -jets is possible due to their  
 985 characteristically long lifetime ( $\tau \approx 1.5$  ps), displaced secondary decay vertex and high decay  
 986 multiplicity.

987 Usage of  $b$ -tagging in this analysis is done via five operating points (OPs), corresponding

988 to 65%, 70%, 77%, 85% and 90%  $b$ -jet tagging efficiency  $\varepsilon_b$  in simulated  $t\bar{t}$  events, in order  
989 from the tightest to loosest discriminant cut point. The OPs are defined by placing selections  
990 on the tagger output to provide a predefined  $\varepsilon_b$  level; the selection cuts act as a variable  
991 trade-off between  $b$ -tagging efficiency and  $b$ -jet purity i.e.  $c$ - or light-jet rejection. For this  
992 analysis, a jet is considered  $b$ -tagged if it passes the 85% OP. The  $b$ -tagged jet is then  
993 assigned a pseudo-continuous  $b$ -tagging (PCBT) score, which quantifies a jet's ability to  
994 satisfy different OPs. The score can take integer values between 1 and 6, where a score of 6  
995 is assigned to jets passing all OP thresholds; a score of 2 for jets that pass only the tightest  
996 OP (90%); and a score of 1 for jets that pass no OP. A value of -1 is also defined for any jet  
997 that does not satisfy  $b$ -tagging criteria. Since the targeted  $t\bar{t}t\bar{t}$  final states contain at least  
998 four  $b$ -hadrons from top and  $W$  decays, a  $b$ -tagging OP of 85% is used to maintain high  
999 purity during  $b$ -tagged jet selections in the signal region.

1000 **GN2  $b$ -tagging algorithm**

1001 For this analysis,  $b$ -jets are identified and tagged with the GN2v01  $b$ -tagger [111]. The  
1002 GN2 algorithm uses a Transformer-based model [112] modified to incorporate domain knowl-  
1003 edge and additional auxiliary physics objectives: grouping tracks with a common vertex and  
1004 predicting the underlying physics process for a track. The network structure is shown in  
1005 Figure 4.3. The GN2  $b$ -tagger form the input vector by concatenating 2 jet variables and  
1006 19 track reconstruction variables (for up to 40 tracks), normalized to zero mean and unit  
1007 variance. The output consists of a track-pairing output layer of size 2, a track origin clas-  
1008 sification layer of 7 categories, and a jet classification layer of size 4 for the probability of  
1009 each jet being a  $b$ -,  $c$ -, light- or  $\tau$ -jet respectively. For  $b$ -tagging purpose, a discriminant is

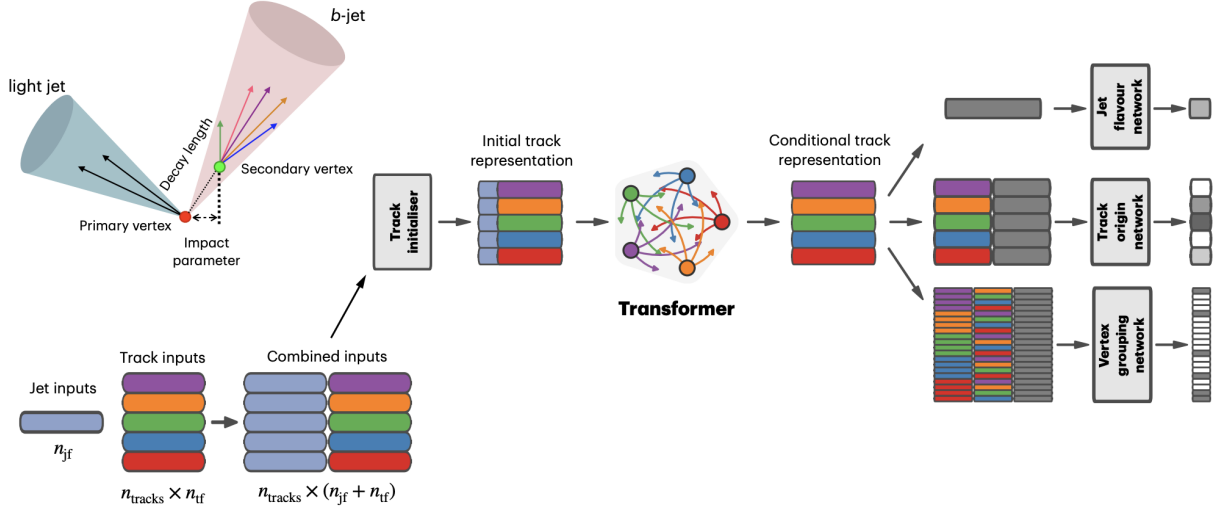


Figure 4.3: Overview of the GN2 architecture. The number of jet and track features are represented by  $n_{\text{jf}}$  and  $n_{\text{tf}}$  respectively. The global jet representation and track embeddings output by the Transformer encoder are used as inputs for three task-specific networks [111].

1010 defined using these four outputs

$$D_b = \ln \left( \frac{p_b}{f_c p_c + f_\tau p_\tau + (1 - f_c - f_\tau)p_{\text{light}}} \right) \quad (4.1)$$

1011 where  $p_x$  is the probability of the jet being an  $x$ -jet as predicted by GN2, and  $f_c, f_\tau$  are tun-  
 1012 able free parameters controlling balance between  $c$ - and light-jet rejection. Simulated SM  $t\bar{t}$   
 1013 and BSM  $Z'$  events from  $pp$  collisions were used as training and evaluation samples. In order  
 1014 to minimize bias, both  $b$ - and light-jet samples are re-sampled to match  $c$ -jet distributions.  
 1015 Figure 4.4 shows the performance of GN2 compared to the previous convolutional neural  
 1016 network-based standard  $b$ -tagging algorithm DL1d, in terms of  $c$ -, light- and  $\tau$ -jet rejection  
 1017 as a function of  $b$ -tagging efficiency. The network gives a factor of 1.5-4 improvement in  
 1018 experimental applications compared to DL1d [111], without dependence on the choice of  
 1019 MC event generator or inputs from low-level flavor tagging algorithm.

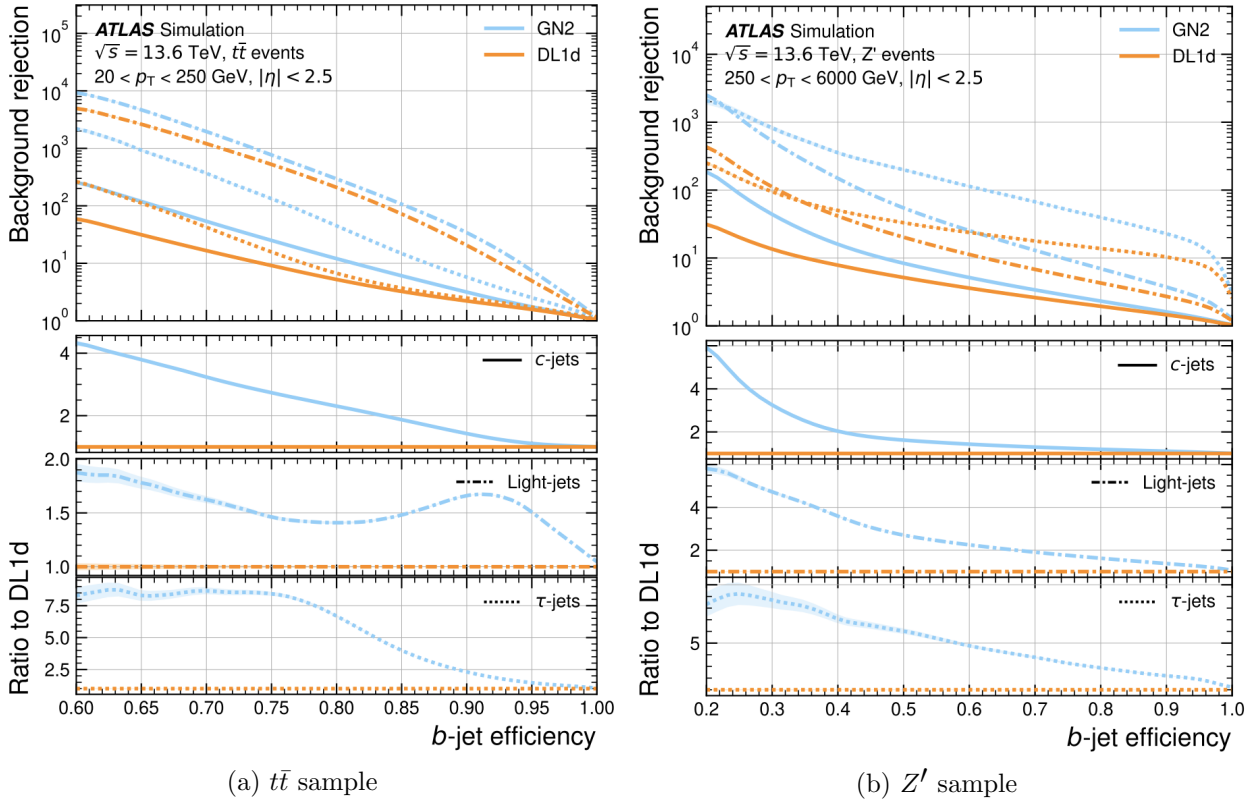


Figure 4.4: The  $c$ -, light- and  $\tau$ -jet rejection rate as a function of  $b$ -tagging efficiency for GN2 and DL1d using (a) jets in the  $t\bar{t}$  sample, and (b) jets in the  $Z'$  sample. The performance ratios of GN2 to DL1d are shown in the bottom panels [111].

## 1020 Efficiency calibration

1021 Due to imperfect description of detector response and physics modeling effects in simu-  
 1022 lation, the  $b$ -tagging efficiency predicted by MC simulation  $\varepsilon_b^{\text{sim}}$  requires a correction factor  
 1023 to match the efficiency measured in collision data  $\varepsilon_b^{\text{data}}$ . The correction scale factors (SFs)  
 1024 are defined as  $\text{SF} = \varepsilon_b^{\text{data}} / \varepsilon_b^{\text{sim}}$  and are determined by data-to-MC calibration using samples  
 1025 enriched in dileptonic  $t\bar{t}$  decays [113]. The resulting SFs are applied to MC simulated jets  
 1026 individually.

## 1027 4.3 Leptons

1028 Lepton reconstruction in ATLAS involves electron and muon reconstruction since tau  
1029 decays quickly, and depending on decay mode can be reconstructed using either jets or light  
1030 leptons. From here on out within this dissertation, leptons will be used exclusively to refer to  
1031 electrons and muons. Leptons can be classified into two categories: prompt leptons resulting  
1032 from heavy particle decays and non-prompt leptons resulting from detector or reconstruction  
1033 effects, or from heavy-flavor hadron decays.

### 1034 4.3.1 Electrons

1035 Electrons leave energy signature in the detector by interacting with the detector materials  
1036 and losing energy in the form of bremsstrahlung photons. A bremsstrahlung photon can  
1037 produce an electron-positron pair which can itself deposit signals in the detector, creating a  
1038 cascade of particles that can leave multiple of either tracks in the ID or EM showers in the  
1039 calorimeters, all of which are considered part of the same EM topo-cluster. Electron signal  
1040 signature has three characteristic components: localized energy deposits in the calorimeters,  
1041 multiple tracks in the ID and compatibility between the above tracks and energy clusters in  
1042 the  $\eta \times \phi$  plane [114]. Electron reconstruction in ATLAS follows these steps accordingly.

1043 Seed-cluster reconstruction and track reconstruction are performed sequentially in ac-  
1044 cordance with the iterative topo-clustering algorithm and track reconstruction method de-  
1045 scribed in section 4.1. The seed-cluster and GSF-refitted track candidate not associated  
1046 with a conversion vertex are matched to form an electron candidate. The cluster energy is  
1047 then calibrated using multivariate techniques on data and simulation to match the original  
1048 electron energy.

1049 **Electron identification**

1050 Additional LH-based identification selections using ID and EM calorimeter information  
1051 are implemented to further improve the purity of reconstructed electrons in the  $|\eta| < 2.47$  re-  
1052 gion of the detector [114]. The electron LH function is built with the signal being prompt elec-  
1053 trons and background being objects with similar signature to prompt electrons i.e. hadronic  
1054 jet deposits, photon conversions or heavy-flavor hadron decays. Three identification OPs  
1055 are defined for physics analyses: *Loose*, *Medium* and *Tight*, optimized for 9 bins in  $|\eta|$  and  
1056 12 bins in  $E_T$  with each OP corresponding to a fixed efficiency requirement for each bin.  
1057 For typical EW processes, the target efficiencies for *Loose*, *Medium* and *Tight* start at 93%,  
1058 88% and 80% respectively and increase with  $E_T$ . Similar to  $b$ -tagging OPs, the electron  
1059 identification OPs represent a trade-off in signal efficiency and background rejection. The  
1060 electron efficiency are estimated using tag-and-probe method on samples of  $J/\Psi \rightarrow ee$  and  
1061  $Z \rightarrow ee$  [114]. The *Tight* electron identification OP is used for this analysis.

1062 **Electron isolation**

1063 A characteristic distinction between prompt electrons and electrons from background  
1064 processes is the relative lack of activity in both the ID and calorimeters within an  $\Delta\eta \times \Delta\phi$   
1065 area surrounding the reconstruction candidate. Calorimeter-based and track-based electron  
1066 isolation variables [114] are defined to quantify the amount of activity around the electron  
1067 candidate using topo-clusters and reconstructed tracks respectively.

1068 Calorimeter-based isolation variables  $E_T^{\text{cone}XX}$  are computed by first summing the energy  
1069 of topo-clusters with barycenters falling within a cone of radius  $\Delta R = \sqrt{(\Delta\eta)^2 + (\Delta\phi)^2} =$   
1070  $XX/100$  around the direction of the electron candidate. The final isolation variables are

obtained by subtracting from the sum the energy belonging to the candidate electron at the core of the cone, then applying corrections for pile-up effects and energy leakage outside of the core. Similar to calorimeter-based variables, track-based isolation variables  $p_T^{\text{varcone}XX}$  are calculated by summing all track  $p_T$  within a cone of radius  $\Delta R$  around the electron candidate, minus the candidate's contribution. The cone radius is variable as a function of  $p_T$  and is described as

$$\Delta R \equiv \min \left( \frac{10}{p_T}, \Delta R_{\max} \right), \quad (4.2)$$

where  $p_T$  is expressed in GeV and  $\Delta R_{\max}$  is the maximum cone size, defined to account for closer proximity of decay products to the electron in high-momentum heavy particle decays. Four isolation operating points are implemented to satisfy specific needs by physics analyses: *Loose*, *Tight*, *HighPtCaloOnly* and *Gradient* [114]. For this analysis, electrons isolation uses *Tight* requirements.

## 1082 Electron charge misidentification

Charge misidentification is a crucial irreducible background, particularly for analyses with electron charge selection criteria. Electron charge is determined by the curvature of the associated reconstructed track, and misidentification of charge can occur via either an incorrect curvature measurement or an incorrectly matched track. Inaccurate measurement is more likely for high energy electrons due to the small curvature in track trajectories at high  $p_T$ , while track matching error usually results from bremsstrahlung pair-production generating secondary tracks in close proximity [114]. Suppression of charge misidentification background in Run 2 is additionally assisted by a boosted decision tree discriminant known

1091 as the Electron Charge ID Selector (ECIDS). For this analysis, all electrons are required to  
1092 pass the ECIDS criterion.

1093 **4.3.2 Muons**

1094 Muons act as minimum-ionizing particles, leaving tracks in the MS or characteristics  
1095 energy deposits in the calorimeter and can be reconstructed globally using information from  
1096 the ID, MS and calorimeters. Five reconstruction strategies corresponding to five muon  
1097 types [115] are utilized in ATLAS:

- Combined (CB): the primary ATLAS muon reconstruction method. Combined muons  
1098 are first reconstructed using MS tracks then extrapolated to include ID tracks (outside-in strategy). A global combined track fit is performed on both MS and ID tracks.
- Inside-out combined (IO): complementary to CB reconstruction. IO muon tracks are  
1101 extrapolated from ID to MS, then fitted with MS hits and calorimeter energy loss in a  
1102 combined track fit.
- MS extrapolated (ME): ME muons are defined as muons with a MS track that cannot  
1104 be matched to an ID track using CB reconstruction. ME muons allow extension of  
1105 muon reconstruction acceptance to regions not covered by the ID ( $2.5 < |\eta| < 2.7$ )
- Segment-tagged (ST): ST muons are defined as a successfully matched ID track that  
1107 satisfies tight angular matching criteria to at least one reconstructed MDT or CSC  
1108 segment when extrapolated to the MS. MS reconstruction is used primarily when  
1109 muons only crossed one layer of MS chambers.
- Calorimeter-tagged (CT): CT muons are defined as an ID track that can be matched to  
1111

1112 energy deposits consistent with those of a minimum-ionizing particle when extrapolated  
1113 through the calorimeter. CT reconstruction extends acceptance range to regions in the  
1114 MS with sparse instrumentation ( $|\eta| < 0.1$ ) with a higher  $p_T$  threshold of 5 GeV,  
1115 compared to the 2 GeV threshold used by other muon reconstruction algorithms due  
1116 to large background contamination at the low  $p_T$  range of  $15 < p_T < 100$  GeV [116].

## 1117 Muon identification

1118 Reconstructed muons are further filtered by identification criteria to select for high-  
1119 quality prompt muons. Requirements include number of hits in the MS and ID, track fit  
1120 properties and compatibility between measurements of the two systems. Three standard  
1121 OPs (*Loose*, *Medium*, *Tight*) are defined to better match the needs of different physics  
1122 analyses concerning prompt muon  $p_T$  resolution, identification efficiency and non-prompt  
1123 muon rejection. The default identification OP for ATLAS physics and also the OP used in  
1124 this analysis is *Medium*, which provides efficiency and purity suitable for a wide range of  
1125 studies while minimizing systematic uncertainties [115].

## 1126 Muon isolation

1127 Muons from heavy particle decays are often produced in an isolated manner compared to  
1128 muons from semileptonic decays, and is therefore an important tool for background rejection  
1129 in many physics analyses. Muon isolation strategies are similar to that of electron in section  
1130 4.3.1, with track-based and calorimeter-based isolation variables. Seven isolation OPs are  
1131 defined using either or both types of isolation variables, balancing between prompt muon  
1132 acceptance and non-prompt muon rejection. The full definition and description for the muon  
1133 isolation OPs are detailed in Ref. [115].

## 1134 4.4 Missing transverse momentum

1135 Collisions at the LHC happen along the  $z$ -axis of the ATLAS coordination system between  
1136 two particle beam of equal center-of-mass energy. By conservation of momentum, the sum of  
1137 transverse momenta of outgoing particles should be zero. A discrepancy between measured  
1138 momentum and zero would then suggest the presence of undetectable particles, which would  
1139 consist of either SM neutrinos or some unknown BSM particles, making missing transverse  
1140 momentum ( $E_T^{\text{miss}}$ ) an important observable to reconstruct.

1141 Reconstructing  $E_T^{\text{miss}}$  utilizes information from fully reconstructed leptons, photons, jets  
1142 and other matched track-vertex objects not associated with a prompt object (soft signals),  
1143 defined with respect to the  $x(y)$ -axis as

$$E_{x(y)}^{\text{miss}} = - \sum_{i \in \{\text{hard objects}\}} p_{x(y),i} - \sum_{j \in \{\text{soft signals}\}} p_{x(y),j}, \quad (4.3)$$

1144 where  $p_{x(y)}$  is the  $x(y)$ -component of  $p_T$  for each particle [117]. The following observables  
1145 can then be defined:

$$\begin{aligned} \mathbf{E}_T^{\text{miss}} &= (E_x^{\text{miss}}, E_y^{\text{miss}}), \\ E_T^{\text{miss}} &= |\mathbf{E}_T^{\text{miss}}| = \sqrt{(E_x^{\text{miss}})^2 + (E_y^{\text{miss}})^2}, \\ \phi^{\text{miss}} &= \tan^{-1}(E_y^{\text{miss}}/E_x^{\text{miss}}), \end{aligned} \quad (4.4)$$

<sub>1146</sub> where  $E_T^{\text{miss}}$  represents the magnitude of the missing transverse energy vector  $\mathbf{E}_T^{\text{miss}}$ , and  
<sub>1147</sub>  $\phi^{\text{miss}}$  its direction in the transverse plane. The vectorial sum  $\mathbf{E}_T^{\text{miss}}$  can be broken down into

$$\mathbf{E}_T^{\text{miss}} = - \underbrace{\sum_{\text{selected electrons}} \mathbf{p}_T^e - \sum_{\text{selected muons}} \mathbf{p}_T^\mu - \sum_{\text{accepted photons}} \mathbf{p}_T^\gamma - \sum_{\text{accepted } \tau\text{-leptons}} \mathbf{p}_T^\tau}_{\text{hard term}} - \underbrace{\sum_{\text{accepted jets}} \mathbf{p}_T^{\text{jet}} - \sum_{\text{unused tracks}} \mathbf{p}_T^{\text{track}}}_{\text{soft term}}. \quad (4.5)$$

<sub>1148</sub> Two OPs are defined for  $E_T^{\text{miss}}$ , *Loose* and *Tight*, with selections on jet  $p_T$  and JVT criteria  
<sub>1149</sub> [118]. The *Tight* OP is used in this analysis; *Tight* reduces pile-up dependence of  $E_T^{\text{miss}}$   
<sub>1150</sub> by removing the phase space region containing more pile-up than hard-scatter jets, at the  
<sub>1151</sub> expense of resolution and scale at low pile-up,

## <sub>1152</sub> 4.5 Overlap removal

<sub>1153</sub> Since different objects are reconstructed independently, it is possible for the same de-  
<sub>1154</sub> tector signals to be used to reconstruct multiple objects. An overlap removal strategy is  
<sub>1155</sub> implemented to resolve ambiguities; the overlap removal process for this analysis applies  
<sub>1156</sub> selections in Table 4.1 sequentially, from top to bottom.

Table 4.1: Overlap removal process for this analysis, applied sequentially from top to bottom.

Remove	Keep	Matching criteria
Electron	Electron	Shared ID track, $p_{T,1}^e < p_{T,2}^e$
Muon	Electron	Shared ID track, CT muon
Electron	Muon	Shared ID track
Jet	Electron	$\Delta R < 0.2$
Electron	Jet	$\Delta R < 0.4$
Jet	Muon	( $\Delta R < 0.2$ or ghost-associated) & $N_{\text{track}} < 3$
Muon	Jet	$\Delta R < \min(0.4, 0.04 + 10\text{GeV}/p_T^\mu)$

## 1157 4.6 Object definition

1158 Table 4.2 summarizes the selections on physics objects used in this analysis. Each se-  
1159 lection comes with associated calibration scale factors (SFs) to account for discrepancies  
1160 between data and MC simulation, and are applied multiplicatively to MC event weights.

Table 4.2: Summary of object selection criteria used in this analysis.  $\ell_0$  refers to the leading lepton in the event.

Selection	Electrons	Muons	Jets
$p_T$ [GeV]	$> 15$ $p_T(\ell_0) > 28$	$> 15$	$> 20$
$ \eta $	$1.52 \leq  \eta  < 2.47$ $< 1.37$	$< 2.5$	$< 2.5$
Identification	<i>TightLH</i> pass ECIDS ( $ee/e\mu$ )	<i>Medium</i>	NNJvt <i>FixedEffPt</i> ( $p_T < 60$ , $ \eta  < 2.4$ )
Isolation	<i>Tight_VarRad</i>	<i>PflowTight_VarRad</i>	
Track-vertex assoc.			
$ d_0^{\text{BL}}(\sigma) $	$< 5$	$< 3$	
$ \Delta z_0^{\text{BL}} \sin \theta $ [mm]	$< 0.5$	$< 0.5$	

# 1161 Chapter 5. Data & Simulated Samples

## 1162 5.1 Data samples

1163 Data samples used in this analysis were collected by the ATLAS detector during Run  
1164 2 data-taking campaign between 2015-2018. The samples contain  $pp$  collisions at center-of-  
1165 mass energy of  $\sqrt{s} = 13$  TeV with 25 ns bunch-spacing, which corresponds to an integrated  
1166 luminosity of  $140 \text{ fb}^{-1}$  with an uncertainty of 0.83% [87]. The HLT trigger strategy is similar  
1167 to that of previous  $t\bar{t}t\bar{t}$  observation analysis [44] and include single lepton and dilepton  
1168 triggers. Calibration for di-muon and electron-muon triggers were not ready for the samples  
1169 used in this analysis, and are therefore not included. Events are also required to contain at  
1170 least one lepton matched to the corresponding object firing the trigger. Triggers used are  
1171 summarized in Table 5.1.

## 1172 5.2 Monte Carlo samples

1173 Monte Carlo simulated samples are used to estimate signal acceptance before unblinding,  
1174 profile the physics background for the analysis and to study object optimizations. Simulated  
1175 samples for this analysis use are generated from ATLAS generalized MC20a/d/e samples for  
1176 Run 2, using full detector simulation (FS) and fast simulation (AF3) to simulate detector  
1177 response. MC samples used and simulation processes are summarized in Table 5.2.

Table 5.1: Summary of all HLT triggers used in this analysis. Events are required to pass at least one trigger.

Trigger	Data period			
	2015	2016	2017	2018
Single electron triggers				
HLT_e24_lhmedium_L1EM20VH	✓	-	-	-
HLT_e60_lhmedium	✓	-	-	-
HLT_e120_lhloose	✓	-	-	-
HLT_e26_lhtight_nod0_ivarloose	-	✓	✓	✓
HLT_e60_lhmedium_nod0	-	✓	✓	✓
HLT_e140_lhloose_nod0	-	✓	✓	✓
Di-electron triggers				
HLT_2e12_lhloose_L12EM10VH	✓	-	-	-
HLT_2e17_lhvloose_nod0	-	✓	-	-
HLT_2e24_lhvloose_nod0	-	-	✓	✓
HLT_2e17_lhvloose_nod0_L12EM15VHI	-	-	-	✓
Single muon trigger				
HLT_mu20_iloose_L1MU15	✓	-	-	-
HLT_mu40	✓	-	-	-
HLT_mu26_ivarmedium	-	✓	✓	✓
HLT_mu50	-	✓	✓	✓

### <sup>1178</sup> 5.2.1 $t\bar{t}Z'$ signal samples

<sup>1179</sup> Signal  $t\bar{t}Z'$  samples were generated based on the simplified topophilic resonance model in  
<sup>1180</sup> section 2.2.1. Six  $Z'$  mass points were utilized for the generation of the signal sample: 1000,  
<sup>1181</sup> 1250, 1500, 2000, 2500 and 3000 GeV. The top- $Z'$  coupling  $c_t$  is chosen to be 1 for a narrow  
<sup>1182</sup> resonance peak, and the chirality angle  $\theta$  is chosen to be  $\pi/4$  to suppress loop production  
<sup>1183</sup> of  $Z'$ . The samples were then generated with MADGRAPH5\_AMC@NLO v.3.5.0 [119] at  
<sup>1184</sup> LO with the NNPDF3.1LO [120] PDF set interfaced with PYTHIA8 [121] using A14 tune  
<sup>1185</sup> and NNPDF2.3lo PDF set for parton showering and hadronization. The resonance width is  
<sup>1186</sup> calculated to be 4% for  $c_t = 1$ .

Table 5.2: Summary of all Monte-Carlo samples used in this analysis.  $V$  refers to an EW ( $W^\pm/Z/\gamma^*$ ) or Higgs boson. Matrix element (ME) order refers to the order in QCD of the perturbative calculation. Tune refers to the underlying-event tune of the parton shower (PS) generator.

Process	ME Generator	ME Order	ME PDF	PS	Tune	Sim.
<b>Signals</b>						
$t\bar{t}Z'$	MADGRAPH5_AMC@NLO LO		NNPDF3.1LO		PYTHIA8 A14	FS
<b><math>t\bar{t}t\bar{t}</math> and <math>t\bar{t}\bar{t}</math></b>						
$t\bar{t}t\bar{t}$	MADGRAPH5_AMC@NLO NLO		NNPDF3.0nlo		PYTHIA8 A14	AF3
	MADGRAPH5_AMC@NLO NLO		MMHT2014 LO		HERWIG7 H7-UE-MMHT	AF3
	SHERPA	NLO	NNPDF3.0nnlo		HERWIG7 SHERPA	FS
$t\bar{t}\bar{t}$	MADGRAPH5_AMC@NLO LO		NNPDF2.3lo		PYTHIA8 A14	AF3
<b><math>t\bar{t}V</math></b>						
$t\bar{t}H$	POWHEGBOX v2	NLO	NNPDF3.0nlo		PYTHIA8 A14	FS
	POWHEGBOX v2	NLO	NNPDF3.0nlo		HERWIG7 H7.2-Default	FS
$t\bar{t}(Z/\gamma^*)$	MADGRAPH5_AMC@NLO NLO		NNPDF3.0nlo		PYTHIA8 A14	FS
	SHERPA	NLO	NNPDF3.0nnlo		SHERPA SHERPA	FS
$t\bar{t}W$	SHERPA	NLO	NNPDF3.0nnlo		SHERPA SHERPA	FS
	SHERPA	LO	NNPDF3.0nnlo		SHERPA SHERPA	FS
<b><math>t\bar{t}</math> and Single-Top</b>						
$t\bar{t}$	POWHEGBOX v2	NLO	NNPDF3.0nlo		PYTHIA8 A14	FS
$tW$	POWHEGBOX v2	NLO	NNPDF3.0nlo		PYTHIA8 A14	FS
$t(q)b$	POWHEGBOX v2	NLO	NNPDF3.0nlo (s)		PYTHIA8 A14	FS
			NNPDF3.0nlo 4f (t)			FS
$tWZ$	MADGRAPH5_AMC@NLO NLO		NNPDF3.0nlo		PYTHIA8 A14	FS
$tZ$	MADGRAPH5_AMC@NLO LO		NNPDF3.0nlo 4f		PYTHIA8 A14	FS
<b><math>t\bar{t}VV</math></b>						
$t\bar{t}WW$	MADGRAPH5_AMC@NLO LO		NNPDF3.0nlo		PYTHIA8 A14	FS
$t\bar{t}WZ$	MADGRAPH	LO	NNPDF3.0nlo		PYTHIA8 A14	AF3
$t\bar{t}HH$	MADGRAPH	LO	NNPDF3.0nlo		PYTHIA8 A14	AF3
$t\bar{t}WH$	MADGRAPH	LO	NNPDF3.0nlo		PYTHIA8 A14	AF3
$t\bar{t}ZZ$	MADGRAPH	LO	NNPDF3.0nlo		PYTHIA8 A14	AF3
<b><math>V(VV)+\text{jets}</math> and <math>VH</math></b>						
$V+\text{jets}$	SHERPA	NLO	NNPDF3.0nnlo		SHERPA SHERPA	FS
$VV+\text{jets}$	SHERPA	NLO	NNPDF3.0nnlo		SHERPA SHERPA	FS
		LO ( $gg \rightarrow VV$ )				FS
$VVV+\text{jets}$	SHERPA	NLO	NNPDF3.0nnlo		SHERPA SHERPA	FS
$VH$	POWHEGBOX v2	NLO	NNPDF3.0aznlo		PYTHIA8 A14	FS

<sub>1187</sub> **5.2.2 Background samples**

<sub>1188</sub> **SM  $t\bar{t}t\bar{t}$  background**

<sub>1189</sub> The nominal SM  $t\bar{t}t\bar{t}$  sample was generated with MADGRAPH5\_AMC@NLO [119] at  
<sub>1190</sub> NLO in QCD with the NNPDF3.0nlo [120] PDF set and interfaced with PYTHIA8.230 [121]  
<sub>1191</sub> using A14 tune [122]. Decays for top quarks are simulated at LO with MADSPIN [123,  
<sub>1192</sub> 124] to preserve spin information, while decays for  $b$ - and  $c$ -hadrons are simulated with  
<sub>1193</sub> EVTGEN v1.6.0 [125]. The renormalization and factorization scales  $\mu_R$  and  $\mu_F$  are set  
<sub>1194</sub> to  $1/4\sqrt{m^2 + p_T^2}$ , which represents the sum of transverse mass of all particles generated  
<sub>1195</sub> from the ME calculation [126]. The ATLAS detector response was simulated with AF3.  
<sub>1196</sub> Additional auxiliary  $t\bar{t}t\bar{t}$  samples are also generated to evaluate the impact of generator and  
<sub>1197</sub> PS uncertainties as shown in 5.2.

<sub>1198</sub>  **$t\bar{t}W$  background**

<sub>1199</sub> Nominal  $t\bar{t}W$  sample was generated using SHERPA v2.2.10 [127] at NLO in QCD with  
<sub>1200</sub> the NNPDF3.0nnlo [120] PDF with up to one extra parton at NLO and two at LO, which  
<sub>1201</sub> are matched and merged with the SHERPA PS based on Catani-Seymour dipole factorization  
<sub>1202</sub> [128] using the MEPS@NLO prescription [129–132] and a merging scale of 30 GeV. Higher-  
<sub>1203</sub> order ME corrections are provided in QCD by the OpenLoops 2 library [133–135] and in  
<sub>1204</sub> EW from  $\mathcal{O}(\alpha^3) + \mathcal{O}(\alpha_S^2\alpha^2)$  (LO3 & NLO2) via two sets of internal event weights. An  
<sub>1205</sub> alternative sample with only EW corrections at LO from  $\mathcal{O}(\alpha_S\alpha^3)$  (NLO3) diagrams were  
<sub>1206</sub> also simulated with the same settings.

1207  **$t\bar{t}(Z/\gamma^*)$  background**

1208 Nominal  $t\bar{t}(Z/\gamma^*)$  samples were generated separately for different ranges of dilepton in-  
1209 variant mass  $m_{\ell\ell}$  to account for on-shell and off-shell  $Z/\gamma^*$  production. Sample for  $m_{\ell\ell}$   
1210 between 1 and 5 GeV was produced using MADGRAPH5\_AMC@NLO [119] at NLO with  
1211 the NNPDF3.0nlo [120] PDF set, interfaced with PYTHIA8.230 [121] using A14 tune [122] and  
1212 NNPDF2.3l0 PDF set. Sample for  $m_{\ell\ell} < 5$  GeV was produced with SHERPA v2.2.10 [127]  
1213 at NLO using NNPDF3.0nnlo PDF set. To account for generator uncertainty, an alternative  
1214  $m_{\ell\ell} > 5$  GeV sample was generated with identical settings to the low  $m_{\ell\ell}$  sample. The  
1215 ATLAS detector response was simulated with full detector simulation (FS).

1216  **$t\bar{t}H$  background**

1217 Generation of  $t\bar{t}H$  background was done using POWHEGBox [136–139] at NLO in QCD  
1218 with the NNPDF3.0nlo PDF [120] set. The nominal sample is interfaced with PYTHIA8.230  
1219 [121] using the A14 tune [122] and the NNPDF2.3l0 [140] PDF set. Detector response is  
1220 simulated using FS. An alternative  $t\bar{t}H$  sample generated similarly, but instead interfaced  
1221 with HERWIG7.2.3 [141, 142] to study the impact of parton shower and hadronization model.  
1222 Detector response for the alternative sample is simulated using AF3.

1223  **$t\bar{t}t$  background**

1224 The  $t\bar{t}t$  sample is generated using MADGRAPH5\_AMC@NLO [119] at LO in QCD, inter-  
1225 faced with PYTHIA8 [121] using the A14 tune [122]. The sample is produced in the five-flavor  
1226 scheme [143] to prevent LO interference with  $t\bar{t}t\bar{t}$ .

1227  **$t\bar{t}$  background**

1228 The  $t\bar{t}$  sample is modeled with POWHEGBox [136–139] at NLO in QCD with the NNPDF3.0nlo  
1229 [120] PDF set and the  $h_{\text{damp}}$  parameter set to  $1.5m_{\text{top}}$  [144]. Events are interfaced with  
1230 PYTHIA8.230 [121] using the A14 tune [122] and the NNPDF2.3l0 [140] PDF set.

1231 **Single-top ( $tW$  &  $t(q)b$ ) background**

1232 Single-top  $tW$ -associated production is modeled using the POWHEGBox generator [136–  
1233 139] at NLO in QCD in the five-flavor scheme [143] with the NNPDF3.0nlo [120] PDF set. In-  
1234 terference with  $t\bar{t}$  production [144] is handled using the diagram removal scheme [145]. Single-  
1235 top  $t(q)b$  production is modeled using the POWHEGBox generator at NLO in QCD with the  
1236 s-channel production modeled in the five-flavor scheme with the NNPDF3.0nlo PDF set, while  
1237 the t-channel production is modeled in the four-flavor scheme with the NNPDF3.0nlo 4f [120]  
1238 PDF set. The  $t\bar{t}WW$  contributions are normalized to NLO theoretical cross section. All  
1239 single-top samples are interfaced with PYTHIA8.230 [121] using the A14 tune [122] and the  
1240 NNPDF2.3l0 [140] PDF set.

1241  **$tWZ$  +jets background**

1242 The  $tWZ$  sample is generated using MADGRAPH5\_AMC@NLO [119] at NLO in QCD  
1243 with the NNPDF3.0nlo [120] PDF set, interfaced with PYTHIA8.212 [121] using the A14 tune  
1244 [122] and the NNPDF2.3l0 [140] PDF set.

1245  **$tZ$  &  $t\bar{t}VV$  background**

1246 Production of  $tZ$  is modeled using MADGRAPH5\_AMC@NLO [119] at NLO in QCD  
1247 with scale of  $H_T/6$  and the NNPDF3.0nlo 4f [120] PDF set. Production of  $t\bar{t}WW$  is modeled

1248 using `MADGRAPH5_AMC@NLO` [119] at LO, while production of  $t\bar{t}WZ$ ,  $t\bar{t}HH$ ,  $t\bar{t}WH$  and  
1249  $t\bar{t}ZZ$  are modeled using `MADGRAPH` at LO. All  $t\bar{t}VV$  samples use the `NNPDF3.0nlo` [120]  
1250 PDF set, and all samples in this section are interfaced with `PYTHIA8` [121] using the A14  
1251 tune [122].

## 1252 Single boson ( $V$ ) +jets background

1253 Production of  $V$ +jets is modeled with `SHERPA v2.2.10` [127] using NLO ME for up to two  
1254 jets and LO ME for up to four jets, with the `NNPDF3.0nlo` [120] PDF set. Matrix elements  
1255 are calculated with the Comix [146] and OpenLoops libraries [133, 134] and matched with  
1256 the `SHERPA` PS based on Catani-Seymour dipole factorization [128] using the MEPS@NLO  
1257 prescription [129–132]. The sample is normalized to NNLO [147] theoretical cross section.

## 1258 Diboson ( $VV$ ) +jets background

1259 Diboson samples are simulated with `SHERPA v2.2.14` [127] with the `NNPDF3.0nlo` [120]  
1260 PDF set. Fully leptonic and semileptonic final states are generated using NLO ME for up to  
1261 one extra parton and LO ME for up to three extra parton emissions. Loop-induced processes  
1262 are generated using LO ME for up to one extra parton. Matrix elements are matched and  
1263 merged with the `SHERPA` PS based on Catani-Seymour dipole factorization [128] using the  
1264 MEPS@NLO prescription [129–132]. Virtual QCD ME corrections are provided by the  
1265 OpenLoops library [133, 134].

## 1266 Triboson ( $VVV$ ) +jets background

1267 The triboson sample is modeled with `SHERPA v2.2.10` [127] using factorized gauge boson  
1268 decays. Matrix elements for the inclusive process at NLO and up to two extra partons at

1269 LO are matched and merged with the SHERPA PS based on Catani-Seymour dipole factor-  
1270 ization [128] using the MEPS@NLO prescription [129–132]. Virtual QCD ME corrections  
1271 are provided by the OpenLoops library [133, 134].

1272 ***VH* background**

1273 Generation of  $WH$  and  $ZH$  samples is performed using PowhegBox [136–139] at NLO  
1274 with the NNPDF3.0aznlo [120] PDF set, interfaced with PYTHIA8.230 [121] using the A14  
1275 tune [122] and the NNPDF2.3l0 [140] PDF set. The samples are normalized to theoretical  
1276 cross sections at NNLO in QCD and NLO in EW accuracies.

<sub>1277</sub> **Chapter 6. Analysis Strategy**

<sub>1278</sub> **6.1 Event selection**

<sub>1279</sub> Events for the analysis first are preselected following a list of criteria to optimize for event  
<sub>1280</sub> quality and background rejection. The following criteria are applied sequentially from top  
<sub>1281</sub> to bottom along with cleaning and veto cuts

- <sub>1282</sub> 1. **Good Run List (GRL)**: data events must be part of a predefined list of suitable  
<sub>1283</sub> runs and luminosity blocks [[148](#)].
- <sub>1284</sub> 2. **Primary vertex**: events must have at least one reconstructed vertex matched to 2 or  
<sub>1285</sub> more associated tracks with  $p_T > 500$  MeV.
- <sub>1286</sub> 3. **Trigger**: events must be selected by at least one trigger in Table 5.1.
- <sub>1287</sub> 4. **Kinematic selection**: events must have exactly two *Tight* leptons with the same  
<sub>1288</sub> electric charge, or at least three *Tight* leptons of any charge. The leading lepton must  
<sub>1289</sub> have  $p_T > 28$  GeV, and all leptons must satisfy  $p_T > 15$  GeV.

<sub>1290</sub> Events are separated into two channels based on the number of leptons: same-sign di-  
<sub>1291</sub> lepton (SS2L) for events with exactly two leptons of the same charge, or multilepton (ML)  
<sub>1292</sub> for events with three or more leptons. The channels are further separated into regions defined  
<sub>1293</sub> in section 6.2 to prepare for analysis.

<sub>1294</sub> Additional selections are applied based on the lepton flavors present. In the SS2L channel,  
<sub>1295</sub> if both leptons are electrons, the invariant mass  $m_{ll}$  must satisfy  $m_{ll} < 81$  GeV and  $m_{ll} > 101$   
<sub>1296</sub> GeV to suppress background involving  $Z$ -bosons. In the ML channel, the same criteria must  
<sub>1297</sub> be satisfied for every opposite-sign same-flavor pair of leptons in an event.

### 1298 6.1.1 Event categorization

1299 Simulated events are categorized using truth information of leptons ( $e/\mu$ ) and their orig-  
1300 inating MC particle (mother-particle). Each lepton can be classified as either prompt or  
1301 non-prompt, with non-prompt leptons further categorized for background estimation pur-  
1302 poses. If an event contains only prompt leptons, the event is classified as its correspond-  
1303 ing process. If the event contains one non-prompt lepton, the event is classified as the corre-  
1304 sponding type of the non-prompt lepton. If the event contains more than one non-prompt  
1305 lepton, the event is classified as other.

1306 • **Prompt:** if the lepton originates from  $W/Z/H$  boson decays, or from a mother-  
1307 particle created by a final state photon.

1308 • **Non-prompt:**

1309 – **Charge-flip ( $e$  only):** if the reconstructed charge of the lepton differs from that  
1310 of the first mother-particle.

1311 – **Material conversion ( $e$  only):** if the lepton originated from a photon conversion  
1312 and the mother-particle is an isolated prompt photon, non-isolated final state  
1313 photon, or heavy boson.

1314 –  **$\gamma^*$ -conversion ( $e$  only):** if the lepton originated from a photon conversion and  
1315 the mother-particle is a background electron.

1316 – **Heavy flavor decay:** if the lepton originated from a  $b$ - or  $c$ -hadron.

1317 – **Fake:** if the lepton originated from a light- or  $s$ -hadron, or if the truth type of  
1318 the lepton is hadron.

1319 – **Other:** any lepton that does not belong to one of the above categories.

## 1320 6.2 Analysis regions

1321 Events are selected and categorized into analysis regions belonging to one of two types:  
 1322 control regions (CRs) enriched in background events, and signal regions (SRs) enriched in  
 1323 signal events. This allows for the examination and control of backgrounds and systematic  
 1324 uncertainties, as well as study of signal sensitivities. The signal is then extracted from the  
 1325 SRs with a profile LH fit using all regions. The full selection criteria for each region are  
 1326 summarized in Table 6.1. The post-fit background compositions in different CRs and SR  
 1327 sub-regions are shown in Figure 6.1.

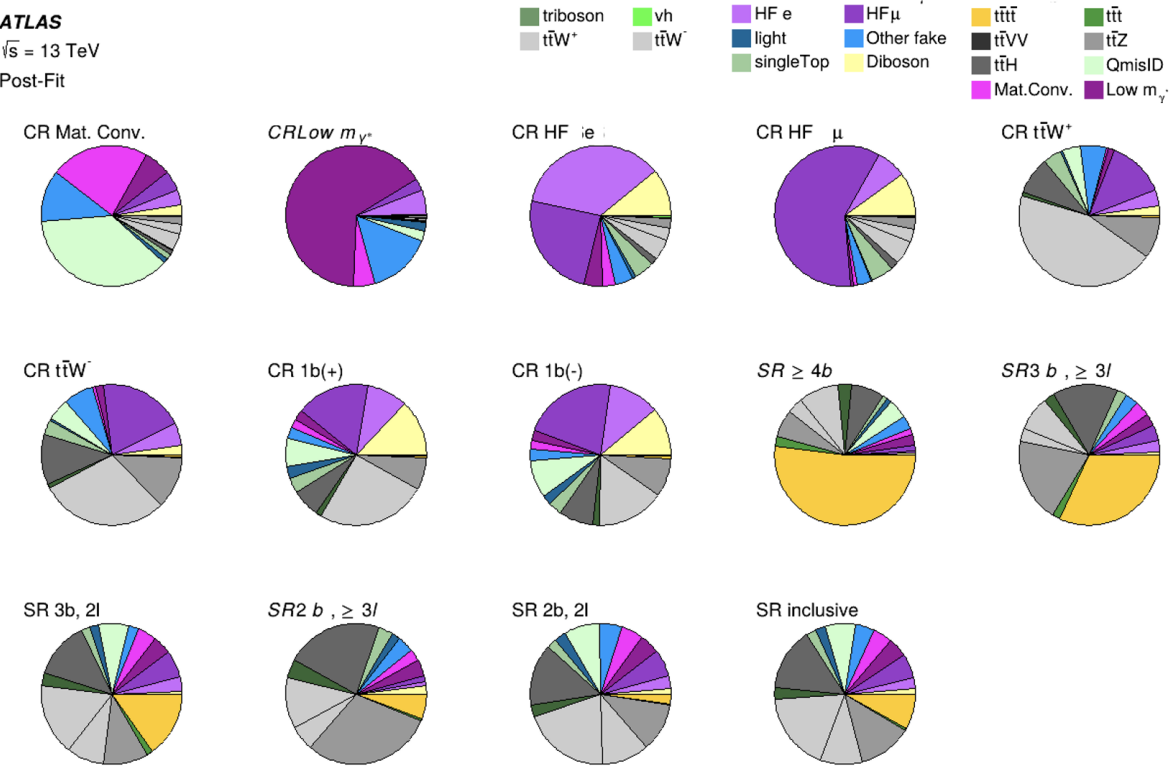


Figure 6.1: Post-fit background composition in each analysis region and sub-region. The fit was performed using ideal pseudo-datasets (Asimov data) in the SR.

Table 6.1: Definitions of signal, control and validation regions (VR) used in this analysis.  $N_{\text{jets}}$  and  $N_b$  refers to the number of jets and number of  $b$ -tagged jets respectively.  $\ell_1$  refers to the leading lepton,  $\ell_2$  refers to the subleading lepton and so on.  $H_T$  refers to the  $p_T$  scalar sum of all leptons and jets in the event.  $m_{\ell\ell}$  refers to the dilepton invariant mass, which must not coincide with the  $Z$ -boson mass range of 81-101 GeV for SS2L+3L events.

Region	Channel	$N_{\text{jets}}$	$N_b$	Other selections	Fitted variable
CR Low $m_{\gamma^*}$	SS $e\ell$	[4, 6)	$\geq 1$	$\ell_1/\ell_2$ is from virtual photon decay $\ell_1 + \ell_2$ not from material conversion	event yield
CR Mat. Conv.	SS $e\ell$	[4, 6)	$\geq 1$	$\ell_1/\ell_2$ is from material conversion $\ell_1 + \ell_2$ not conversion candidates	event yield
CR HF $\mu$	$\ell\mu\mu$	$\geq 1$	1	$100 < H_T < 300$ GeV $E_T^{\text{miss}} > 35$ GeV total charge = $\pm 1$	$p_T(\ell_3)$
CR HF $e$	$e\ell\ell$	$\geq 1$	1	$\ell_1 + \ell_2$ not conversion candidates $100 < H_T < 275$ GeV $E_T^{\text{miss}} > 35$ GeV total charge = $\pm 1$	$p_T(\ell_3)$
CR $t\bar{t}W^+$	SS $\ell\mu$	$\geq 4$	$\geq 2$	$ \eta(e)  < 1.5$ for $N_b = 2$ : $H_T < 500$ GeV or $N_{\text{jets}} < 6$ for $N_b \geq 3$ : $H_T < 500$ GeV total charge > 0	$N_{\text{jets}}$
CR $t\bar{t}W^-$	SS $\ell\mu$	$\geq 4$	$\geq 2$	$ \eta(e)  < 1.5$ for $N_b = 2$ : $H_T < 500$ GeV or $N_{\text{jets}} < 6$ for $N_b \geq 3$ : $H_T < 500$ GeV total charge < 0	$N_{\text{jets}}$
CR 1b(+)	SS2L+3L	$\geq 4$	1	$\ell_1 + \ell_2$ not from material conversion $H_T > 500$ GeV total charge > 0	$N_{\text{jets}}$
CR 1b(-)	SS2L+3L	$\geq 4$	1	$\ell_1 + \ell_2$ not from material conversion $H_T > 500$ GeV total charge < 0	$N_{\text{jets}}$
VR $t\bar{t}Z$	3L $\ell^\pm\ell^\mp$	$\geq 4$	$\geq 2$	$m_{\ell\ell} \in [81, 101]$ GeV	$N_{\text{jets}}, m_{\ell\ell}$
VR $t\bar{t}W +1b$	SS2L+3L			CR $t\bar{t}W^\pm$    CR 1b( $\pm$ )	$N_{\text{jets}}$
VR $t\bar{t}W +1b+SR$	SS2L+3L			CR $t\bar{t}W^\pm$    CR 1b( $\pm$ )    SR	$N_{\text{jets}}$
SR	SS2L+3L	$\geq 6$	$\geq 2$	$H_T > 500$ GeV $m_{\ell\ell} \notin [81, 101]$ GeV	$H_T$

<sub>1328</sub> **6.2.1 Signal regions**

<sub>1329</sub> All events selected for the SR must satisfy the following criteria:

- <sub>1330</sub> • Contains 6 or more jets, with at least 2 jets  $b$ -tagged at the 85% OP.
- <sub>1331</sub> • Scalar sum of the transverse momenta of all leptons and jets  $H_T > 500$  GeV.
- <sub>1332</sub> • Dilepton invariant mass  $m_{\ell\ell}$  does not coincide with the  $Z$ -boson mass range of 81 – 101
- <sub>1333</sub> GeV

<sub>1334</sub> The SR is further divided into sub-regions by the number of  $b$ -tagged jets and leptons

<sub>1335</sub> present to study signal behavior and sensitivity with respect to the selection variables.

Table 6.2: Definitions of SR sub-regions. Events are sorted into different sub-regions based on the number of  $b$ -tagged jets and leptons present.

Sub-region	Selection criteria	
	$b$ -jets	leptons
SR 2b2l	$N_b = 2$	$N_l = 2$
SR 2b3l4l	$N_b = 2$	$N_l \geq 3$
SR 3b2l	$N_b = 3$	$N_l = 2$
SR 3b3l4l	$N_b = 3$	$N_l \geq 3$
SR 4b	$N_b \geq 4$	

<sub>1336</sub> **Signal extraction**

<sub>1337</sub> Signal extraction in the SR is performed via a binned profile likelihood (LH) fit as de-

<sub>1338</sub> scribed in section 8.1 using  $H_T$  as the discriminant observable. The discriminant observable

<sub>1339</sub> for a LH fit serves as the set of observed data upon which the LH function is constructed.

<sub>1340</sub> Ideally, the chosen observable shows significant separation between the functional forms of

<sub>1341</sub> the signal and background distributions, allowing for effective separation of the two. Fig-

<sub>1342</sub> ure 6.2 shows several pre-fit kinematic distributions in the inclusive SR. From empirical

1343 optimization studies,  $H_T$  possesses good discriminating power compared to other observ-  
1344 ables constructed using event-level information.

1345 **6.2.2 Control regions**

1346 Control regions are defined for each background to be enriched in the targeted process, in  
1347 order to maximize the background's purity and minimize contamination from other sources  
1348 within the region. This helps to constrain and reduce correlation between background nor-  
1349 malization factors in the final fit. Fit variables and selection criteria are determined via  
1350 optimization studies performed on CRs that aimed to achieve the largest discriminating  
1351 power possible between the target background and other event types.

1352  **$t\bar{t}W$  background CRs**

1353 Theoretical modeling for  $t\bar{t}W + \text{jets}$  background in the phase space of this analysis suffers  
1354 from large uncertainties, especially at high jet multiplicities [149]. A data-driven method was  
1355 employed in a similar manner to the SM  $t\bar{t}t\bar{t}$  observation analysis [44] to mitigate this effect,  
1356 and are described in further details in section 6.3.3. The method necessitates the definition  
1357 of two groups of dedicated CRs to estimate the flavor composition and normalization of  $t\bar{t}W$   
1358 + jets background: CR  $t\bar{t}W + \text{jets}$  to constrain flavor composition, and CR 1b to constrain  
1359 the jet multiplicity spectrum. These are further split into CR  $t\bar{t}W^\pm$  and CR 1b( $\pm$ ) due to  
1360 the pronounced asymmetry in  $t\bar{t}W$  production from  $pp$  collisions, with  $t\bar{t}W^+$  being produced  
1361 at approximately twice the rate of  $t\bar{t}W^-$  [150].

1362 Events in CR  $t\bar{t}W^\pm$  are required to contain at least two  $b$ -tagged jets similar to the SR  
1363 to determine the  $t\bar{t}W$  normalization within an SR-related phase space. Orthogonality with  
1364 SR is ensured by requiring  $H_T < 500$  GeV or  $N_{\text{jets}} < 6$  when  $N_b = 2$ , and  $H_T < 500$

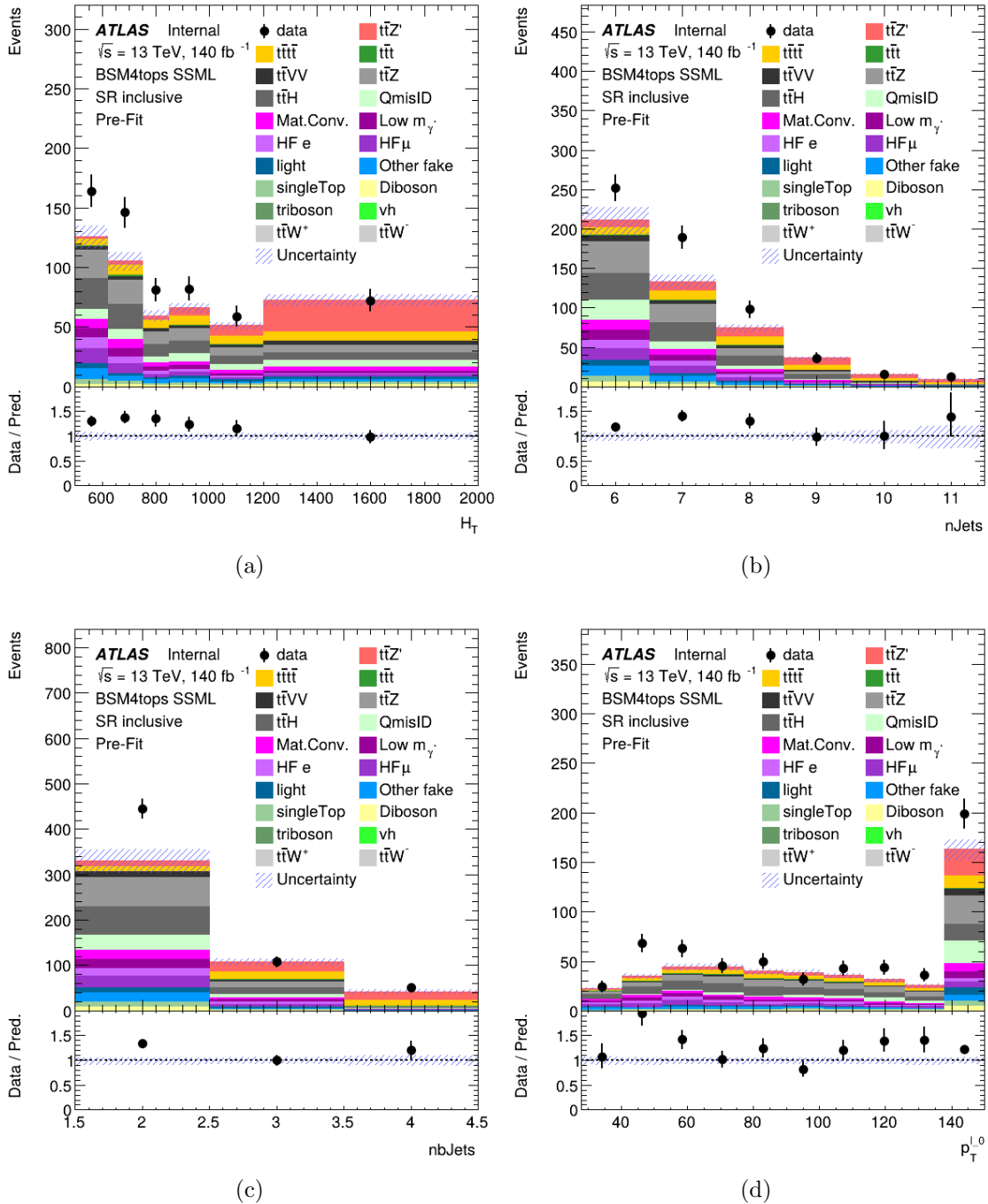


Figure 6.2: Pre-fit kinematic distributions and event compositions in the inclusive SR for (a)  $H_T$  i.e. scalar sum of  $p_T$  of all objects in the event, (b) jet multiplicity, (c)  $b$ -jet multiplicity, (d) leading lepton  $p_T$ . The shaded band represents the uncertainty in the total distribution. The first and last bins of each distribution contain underflow and overflow events respectively.

1365 GeV when  $N_b \geq 3$ . Events in CR 1b( $\pm$ ) are required to have  $H_T > 500$  GeV and at least  
 1366 four jets to encompass events with high  $N_{\text{jets}}$ , which can be used to determine the  $t\bar{t}W$  jet  
 1367 multiplicity spectrum for fitting  $a_{0,1}$ . The selection criteria also include exactly one  $b$ -tagged  
 1368 jet to maintain orthogonality with the SR.

### 1369 **Fake/non-prompt background CRs**

1370 Selection for fake/non-prompt CRs are determined using the `DFCommonAddAmbiguity`  
 1371 (`DFCAA`) variable for reconstructed leptons.

Table 6.3: List of possible assigned values for DFCAA.

DFCAA	Description
-1	No 2nd track found
0	2nd track found, no conversion found
1	Virtual photon conversion candidate
2	Material conversion candidate

1372 Four CRs are defined for the three main types of fake/non-prompt backgrounds in the  
 1373 analysis - virtual photon ( $\gamma^*$ ) conversion, photon conversion in detector material (Mat.  
 1374 Conv.) and heavy flavor decays (HF). The full selection criteria for fake/non-prompt CRs  
 1375 are shown in Table 6.1.

- 1376 • **Low  $m_\gamma^*$ :** events with an  $e^+e^-$  pair produced from a virtual photon.

1377 Events are selected if there are two same-sign leptons with at least one electron recon-  
 1378 structed as an internal conversion candidate, and neither reconstructed as a material  
 1379 conversion candidate.

- 1380 • **Mat. Conv.:** events with an electron originating from photon conversion within the  
 1381 detector material.

1382 Events are selected if there are two same-sign leptons with at least one electron recon-  
1383 structed as a material conversion candidate.

1384 • **HF  $e(\mu)$ :** events with a reconstructed non-prompt lepton from semi-leptonic decays of  
1385  $b$ - and  $c$ -hadrons (heavy flavor decays).

1386 Events are selected if there are three leptons with at least two electrons (muons), with  
1387 no lepton reconstructed as a conversion candidate.

## 1388 6.3 Background estimation

1389 Background in this analysis consist of SM processes that can result in a signal signature  
1390 similar to a  $t\bar{t}t\bar{t}$  SSML final state and can be divided into two types, reducible and irreducible.

1391 Reducible background consists of processes that do not result in a SSML final state physically,  
1392 but are reconstructed as such due to detector and reconstruction effects. The main types  
1393 of reducible background considered are charge misidentification (QmisID) and fake/non-

1394 prompt leptons. Fake/non-prompt lepton backgrounds contaminate the SR when a non-  
1395 prompt lepton is reconstructed as a prompt lepton in a  $t\bar{t}$ -associated process, leading to  
1396 a similar final state to that of SSML  $t\bar{t}t\bar{t}$ . These backgrounds are estimated using the

1397 template fitting method described in subsection 6.3.1, where MC simulations are normalized  
1398 to their theoretical SM cross section via floating normalization factors (NFs) constrained by

1399 the corresponding CRs. Lepton charge misidentification background contaminates the SR  
1400 similarly when one of the two leptons in a  $t\bar{t}$ -associated process with two opposite-sign leptons

1401 is misidentified, producing a SS2L  $t\bar{t}t\bar{t}$  final state. Charge misidentification background is  
1402 estimated using a data-driven method described in section 6.3.2 along with ECIDS described  
1403 in section 4.3.1.

1404 Irreducible background consists of SM processes that result in SSML final states physi-  
1405 cally with all leptons being prompt. The dominating background in the SR are SM  $t\bar{t}t\bar{t}$ ,  $t\bar{t}W$ ,  
1406  $t\bar{t}Z$ , and  $t\bar{t}H$  production with smaller contributions from  $VV$ ,  $VVV$ ,  $VH$  and rarer processes  
1407 like  $t\bar{t}VV$ ,  $tWZ$ ,  $tZq$  and  $t\bar{t}t$ . Most irreducible backgrounds are estimated using template  
1408 fitting method, with the exception of  $t\bar{t}W + \text{jets}$  background. The  $t\bar{t}W + \text{jets}$  background is  
1409 instead given four dedicated CRs, and estimated using a data-driven method with a fitted  
1410 function parameterized in  $N_{\text{jets}}$ . All CRs and SR are included in the final profile LH fit to  
1411 data.

### 1412 6.3.1 Template fitting for fake/non-prompt estimation

1413 Template fitting method is a semi-data-driven approach [149] that estimates fake/non-  
1414 prompt background distributions by fitting the MC kinematic profile of background processes  
1415 arising from fake/non-prompt leptons to data. The four main sources of fake/non-prompt  
1416 leptons are generated from  $t\bar{t} + \text{jets}$  samples and are constrained by four CRs enriched with  
1417 the corresponding backgrounds. Each of the aforementioned background is assigned a free-  
1418 floating NF resulting in  $\text{NF}_{\text{HF } e}$ ,  $\text{NF}_{\text{HF } \mu}$ ,  $\text{NF}_{\text{Mat. Conv.}}$  and  $\text{NF}_{\text{Low } m_{\gamma^*}}$ . The NFs are fitted  
1419 simultaneously with the signal within their constraining CRs.

### 1420 6.3.2 Charge misidentification data-driven estimation

1421 The  $ee$  and  $e\mu$  channels in the SS2L  $t\bar{t}t\bar{t}$  region are contaminated with opposite-sign  
1422 (OS) dilepton  $t\bar{t}$ -associated events where one electron has its charge misidentified. Charge  
1423 misidentification (QmisID) largely affects electrons due to muons' precise curvature informa-  
1424 tion using ID and MS measurements and low bremsstrahlung rate. The charge flip rates are

<sub>1425</sub> significant at higher  $p_T$  and varies with  $|\eta|$  which is proportional to the amount of detector  
<sub>1426</sub> material the electron interacted with.

<sub>1427</sub> The charge flip probability  $\epsilon$  is estimated in this analysis with a data-driven method  
<sub>1428</sub> [151] using a sample of  $Z \rightarrow e^+e^-$  events with additional constraints on the invariant mass  
<sub>1429</sub>  $m_{ee}$  to be within 10 GeV of the  $Z$ -boson mass. The  $Z$ -boson mass window is defined to  
<sub>1430</sub> be within  $4\sigma$  to include most events within the peak, and is determined by fitting the  $m_{ee}$   
<sub>1431</sub> spectrum of the two leading electrons to a Breit-Wigner function, resulting in a range of  
<sub>1432</sub> [65.57, 113.49] for SS events and [71.81, 109.89] for OS events. Background contamination  
<sub>1433</sub> near the peak is assumed to be uniform and subtracted using a sideband method. Since the  
<sub>1434</sub>  $Z$ -boson decay products consist of a pair of opposite-sign electrons, all same-sign electron  
<sub>1435</sub> pairs are considered affected by charge misidentification.

<sub>1436</sub> Let  $N_{ij}^{\text{SS}}$  be the number of events with SS electrons with the leading electron in the  
<sub>1437</sub>  $i^{\text{th}}$  2D bin in  $(p_T, |\eta|)$  and the sub-leading electron in the  $j^{\text{th}}$  bin. Assuming the QmisID  
<sub>1438</sub> probabilities of electrons in an event are uncorrelated,  $N_{ij}^{\text{SS}}$  can be estimated as

$$N_{ij}^{\text{SS}} = N_{ij}^{\text{tot}} [\epsilon_i(1 - \epsilon_j) + \epsilon_j(1 - \epsilon_i)], \quad (6.1)$$

<sub>1439</sub> where  $N_{ij}^{\text{tot}}$  is the total number of events in the  $i^{\text{th}}$  and  $j^{\text{th}}$  bin regardless of charge, and  
<sub>1440</sub>  $\epsilon_{i(j)}$  is the QmisID rate in the  $i^{\text{th}}(j^{\text{th}})$  bin. Assuming  $N_{ij}^{\text{SS}}$  follows a Poisson distribution  
<sub>1441</sub> around the expectation value  $\bar{N}_{ij}^{\text{SS}}$ , the  $(i, n)^{\text{th}}$  rate  $\epsilon$  can be estimated by minimizing a  
<sub>1442</sub> negative-LLH function parameterized in  $p_T$  and  $|\eta|$ ,

$$\begin{aligned}
-\ln(\mathcal{L}(\epsilon|N_{\text{SS}})) &= -\ln \prod_{ij} \frac{(N_{ij}^{\text{tot}})^{N_{ij}^{\text{SS}}} \cdot e^{N_{ij}^{\text{tot}}}}{N_{ij}^{\text{SS}}!} \\
&= -\sum_{ij} \left[ N_{ij}^{\text{SS}} \ln(N_{ij}^{\text{tot}}(\epsilon_i(1-\epsilon_j) + \epsilon_j(1-\epsilon_i))) - N_{ij}^{\text{tot}}(\epsilon_i(1-\epsilon_j) + \epsilon_j(1-\epsilon_i)) \right]. \tag{6.2}
\end{aligned}$$

1443 The QmisID rates are then calculated separately for SR and CRs with different electron  
 1444 definitions i.e. CR Low  $m_{\gamma^*}$ , CR Mat. Conv., CR  $t\bar{t}W^\pm$ , using events from data after  
 1445 applying region-specific lepton selections and ECIDS. The events are required to satisfy  
 1446 SS2L kinematic selections but contains OS electrons. The following weight is applied to OS  
 1447 events to correct for misidentified SS events within the region,

$$w = \frac{\epsilon_i + \epsilon_j - 2\epsilon_i\epsilon_j}{1 - \epsilon_i - \epsilon_j + 2\epsilon_i\epsilon_j}. \tag{6.3}$$

1448 The QmisID rates calculated for SR and CR  $t\bar{t}W$  are shown in Figure 6.3

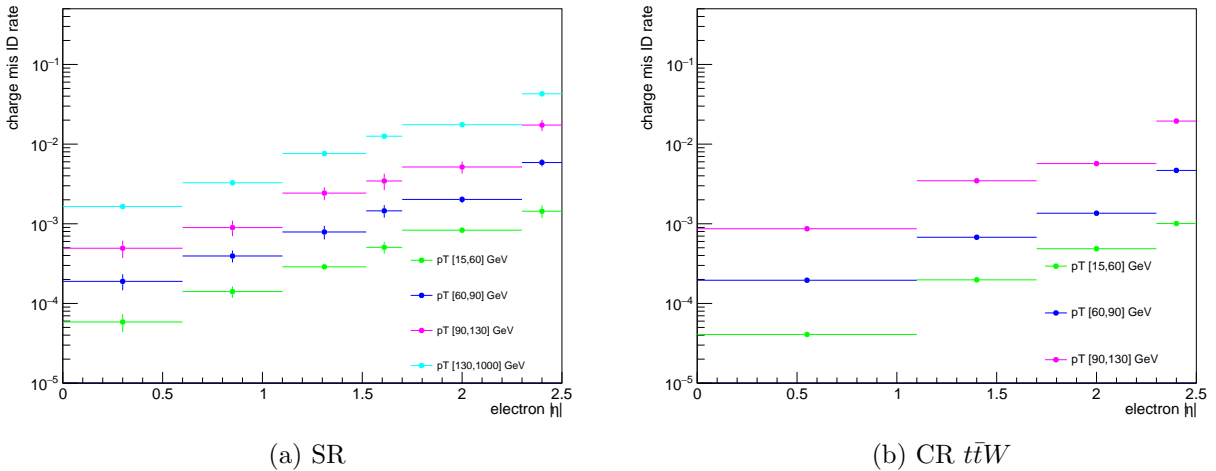


Figure 6.3: Charge flip rate calculated for SR and CR  $t\bar{t}W$  in bins of  $|\eta|$  and  $p_T$ .

1449        The QmisID rates obtained after applying  $w$  contain a dependency on jet multiplicity  
 1450        and are underestimated at higher  $N_{\text{jets}}$ . This dependency affect the SR which require events  
 1451        with  $\geq 6$  jets, and is corrected by applying a correction factor  $SF_{i,n} = \epsilon_{i,n}/\epsilon_{i,N}$  where  $N$  is  
 1452        the inclusive bin containing all  $N_{\text{jets}}$  and  $\epsilon_{i,n}$  is the QmisID rate obtained from Equation 6.2  
 1453        in the  $(i, n)^{\text{th}}$  2D bin in  $(p_{\text{T}}, N_{\text{jets}})$ . Jet multiplicity and consequently the obtained SFs are  
 1454        assumed to be independent of  $|\eta|$ .

### 1455        6.3.3 $t\bar{t}W$ background data-driven estimation

1456        Previously, the  $t\bar{t}W$  background in  $t\bar{t}t\bar{t}$  final state analysis was handled by assigning large  
 1457        ad-hoc systematic uncertainties to  $t\bar{t}W$  events with 7 or more jets [46]. A semi-data-driven  
 1458        method [152] was shown to be effective in the SM  $t\bar{t}t\bar{t}$  observation analysis [44] by improving  
 1459         $t\bar{t}W$  modeling, especially in the showering step and switching  $t\bar{t}W$  systematic uncertainties  
 1460        from predominantly modeling to statistical.

1461        The data-driven method applies correction factors obtained from a fitted function pa-  
 1462        rameterized in  $N_{\text{jets}}$  to  $t\bar{t}W$  MC kinematic distibutions. The QCD scaling patterns [153] can  
 1463        be represented by ratio of successive exclusive jet cross-sections

$$R_{(n+1)/n} = \frac{\sigma_{n+1}}{\sigma_n} = e^{-b} + \frac{\bar{n}}{n+1} = a_0 + \frac{a_1}{1+(j-4)}, \quad (6.4)$$

1464        where  $a_{0(1)}$  and  $b$  are constants,  $n$  is the number of jets in addition to the hard process,  $j$   
 1465        is the inclusive number of jets, and  $\bar{n}$  is the expectation value for the Poisson distribution  
 1466        of exclusive jet cross-section at jet multiplicity  $n$ . The  $t\bar{t}W$  ME for SS2L events gives 4 jets  
 1467        in the hard process, so  $n$  is defined starting from the 5<sup>th</sup> jets and the inclusive number of  
 1468        jets  $j = n + 4$ . The two terms in Equation 6.4 correspond to staircase and Poisson scaling

1469 in cross section between successive jet multiplicities and are sensitive to high and low jet  
1470 multiplicity events respectively [153]. The scaling pattern can then be reparameterized in  
1471  $a_0$  and  $a_1$  to obtain the  $t\bar{t}W$  yield at  $j' \equiv j + 1$  jets

$$\text{Yield}_{t\bar{t}W(j')} = \text{Yield}_{t\bar{t}W(N_{\text{jets}}=4)} \times \prod_{j=4}^{j'-1} \left( a_0 + \frac{a_1}{1+(j-4)} \right) \quad (6.5)$$

1472 with  $j \geq 4$ . The  $t\bar{t}W$  yield in the 4-jet bin can be represented by a NF applied to  $t\bar{t}W$  MC  
1473 simulation

$$\text{Yield}_{t\bar{t}W(N_{\text{jets}}=4)} = \text{NF}_{t\bar{t}W(N_{\text{jets}}=4)} \times \text{MC}_{t\bar{t}W(N_{\text{jets}}=4)}. \quad (6.6)$$

1474 To account for the asymmetry in  $t\bar{t}W^+$  and  $t\bar{t}W^-$  cross-sections,  $\text{NF}_{t\bar{t}W(N_{\text{jets}}=4)}$  is further  
1475 split into  $\text{NF}_{t\bar{t}W^\pm(N_{\text{jets}}=4)}$  assuming the scaling is the same for both processes. Both NFs  
1476 are left free-floating to constrain  $t\bar{t}W$  yields in the 4-jet bin within CR 1b(+) and CR 1b(-).  
1477 The final  $N_{\text{jets}}$ -parameterized function can then be represented by  $\text{NF}_{t\bar{t}W(j')}$  as

$$\text{NF}_{t\bar{t}W(j')} = \left( \text{NF}_{t\bar{t}W^+(N_{\text{jets}}=4)} + \text{NF}_{t\bar{t}W^-(N_{\text{jets}}=4)} \right) \times \prod_{j=4}^{j'-1} \left( a_0 + \frac{a_1}{1+(j-4)} \right). \quad (6.7)$$

1478 The normalization is calculated and applied separately for each sub-sample of  $t\bar{t}W^+$  and  
1479  $t\bar{t}W^-$  in a  $N_{\text{jets}}$  bin for  $4 \leq N_{\text{jets}} < 10$ . Due to small contributions in the CRs, events  
1480 with  $N_{\text{jets}} < 4$  and  $N_{\text{jets}} \geq 10$  are not normalized with this scheme. Instead,  $N_{\text{jets}} < 4$   
1481 events are fitted by propagating the normalization in the 4-jet bin without additional shape  
1482 correction. The correction factor for  $t\bar{t}W$  events with  $N_{\text{jets}} \geq 10$  is obtained by summing  
1483 up the overflow from  $N_{\text{jets}} = 10$  to  $N_{\text{jets}} = 12$ , described as  $\sum_{j'=10}^{12} \prod_{j=4}^{j'-1} \left( a_0 + \frac{a_1}{1+(j-4)} \right)$ .  
1484 Events with  $N_{\text{jets}} \geq 13$  are negligible and are not included in the sum.

1485      The four regions, CR  $t\bar{t}W^\pm$  and CR 1b( $\pm$ ), are constructed to fit  $NF_{t\bar{t}W^\pm(N_{\text{jets}}=4)}$  and  
1486 the scaling parameters  $a_{0(1)}$ , as well as validating the parameterization. Assuming the  $N_{\text{jets}}$   
1487 distribution of  $t\bar{t}W$  is similar across bins of  $N_b$ -jets, a fitted  $N_{\text{jets}}$  distribution in CR 1b( $\pm$ )  
1488 can be used to describe the  $t\bar{t}W$  parameterization at higher  $N_{\text{jets}}$ .

# 1489 Chapter 7. Systematic Uncertainties

1490 Physics analysis inherently incurs uncertainties in the form of statistical and systematic  
1491 uncertainties, depending on the source. Statistical uncertainties occur in this analysis from  
1492 sample size of collected data and simulated MC samples, and from the maximizing of the  
1493 LH function. Systematic uncertainties depend on identifiable sources in the analysis i.e.  
1494 from detector and reconstruction effects (experimental uncertainties) or theoretical modeling  
1495 (theoretical uncertainties). Systematic uncertainties are represented as nuisance parameters  
1496 ( $NP_x$ ) in the profile LH fit. During the fit, systematic uncertainties with negligible impact  
1497 on the final results can be pruned to simplify the statistical model and reduce computational  
1498 complexity. This section outlines all uncertainties considered in this analysis.

## 1499 7.1 Experimental uncertainties

### 1500 7.1.1 Luminosity & pile-up reweighting

1501 The uncertainty on the integrated luminosity of the 2015-2018 Run 2 data set is 0.83%  
1502 [87], obtained by the LUCID-2 detector [154] for the primary luminosity measurements and  
1503 complemented by the ID and calorimeters. Pile-up was modeled in MC and calibrated  
1504 to data through pile-up reweighting, resulting in a set of calibration SFs and associated  
1505 uncertainties.

### 1506 7.1.2 Leptons

1507 In general, calibrating MC simulations to match performance in data incurs uncertainties  
1508 associated obtaining the MC-to-data calibration SFs, which are in turn propagated to observ-

ables in the analysis. The data-to-MC calibration of trigger, reconstruction, identification and isolation efficiencies for electrons and muons incur associated uncertainties, with separate systematic and statistical components for those related to muons. Similarly, electron energy scale, muon momentum scale and resolution are also subjected to calibration uncertainties estimated by re-simulating the events while varying the energy/momenta scale and resolution. Electron has an additional uncertainty related to ECIDS efficiency. Muon has additional uncertainties for charge-independent and charge-dependent momentum scale, as well as detector-specific track resolution. Systematic uncertainties for electron reconstruction, identification, isolation, ECIDS efficiencies and muon ID/MS energy resolution were not ready for the sample version used in this analysis, and are therefore not included.

### 7.1.3 Jets

Experimental uncertainties for jets are dominated by flavor tagging-related uncertainties, with subleading contributions from uncertainties related to JES [110], JER [109] and JVT [155] calibrations.

#### Jet energy scale

Uncertainties associated with JES are determined using data from LHC collisions along with MC simulated samples [110], decomposed into uncorrelated components:

- **Effective NPs:** 15 total  $p_T$ -dependent uncertainty components measured in situ, grouped based on their origin (2 detector-related, 4 modeling-related, 3 mixed, 6 statistical-related)
- **$\eta$  intercalibration:** 6 total components (1 modeling-related, 4 non-closure and 1

1530 statistical-related) associated with the correction of the forward jets' ( $0.8 \leq |\eta| < 4.5$ )  
1531 energy scale to that of the central jets ( $|\eta| < 0.8$ ).

1532 • **Flavor composition & response:** 2 components for relative quark-gluon flavor com-  
1533 positions in background and signal samples, and 2 components for responses to gluon-  
1534 initiated versus quark-initiated jets.

1535 • **Pile-up subtraction:** 4 components, 2 for  $\mu$  (`OffsetMu`) and  $N_{\text{PV}}$  (`OffsetNPV`) mod-  
1536 eling, 1 for residual  $p_{\text{T}}$ -dependency (`PtTerm`) and 1 for topology dependence on the  
1537 per-event  $p_{\text{T}}$  density modeling (`RhoTopology`).

1538 • **Punch-through effect treatment:** 2 terms for GSC punch-through jet response  
1539 deviation between data and MC, one for each detector response simulation method  
1540 (AF3 and FS).

1541 • **Non-closure:** 1 term applied to AF3 sample to account for the difference between  
1542 AF3 and FS simulation.

1543 • **High- $p_{\text{T}}$  single-particle response:** 1 term for the response to high- $p_{\text{T}}$  jets from  
1544 single-particle and test-beam measurements.

1545 •  **$b$ -jets response:** 1 term for the difference between  $b$ -jets and light-jets response.

## 1546 Jet energy resolution

1547 Measurements of JER were performed in bins of  $p_{\text{T}}$  and  $\eta$ , separately in data using in-  
1548 situ techniques and in MC simulation using dijet events [109]. This analysis uses the full  
1549 correlation JER uncertainty scheme provided for Run 2 analysis with 14 total components:

<sub>1550</sub> 12 for effective NPs and 2 for difference between data and MC, separately for AF3 and FS  
<sub>1551</sub> [109].

## <sub>1552</sub> Jet vertex tagging

<sub>1553</sub> The uncertainty associated with JVT is obtained by varying the JVT efficiency SFs  
<sub>1554</sub> within their uncertainty range [155]. This uncertainty accounts for remaining contamination  
<sub>1555</sub> from pile-up jets after applying pile-up suppression and MC generator choice.

## <sub>1556</sub> Flavor tagging

<sub>1557</sub> Calibration SFs for  $b$ -tagging efficiencies and  $c$ -/light-jets mistagging rates are derived as  
<sub>1558</sub> a function of  $p_T$  for  $b$ -,  $c$ -, light-jets and PCBT score. The full set of flavor tagging-related  
<sub>1559</sub> uncertainties was reduced in dimensions by diagonalizing the uncertainty covariance matrix  
<sub>1560</sub> via eigendecomposition [113], resulting in a compact set of orthogonal NPs for this analysis:  
<sub>1561</sub> 85 for  $b$ -jets, 56 for  $c$ -jets and 42 for light-jets.

### <sub>1562</sub> 7.1.4 Missing transverse energy

<sub>1563</sub> Uncertainties on  $E_T^{\text{miss}}$  arise from possible mis-calibration of the soft-track component  
<sub>1564</sub> and are estimated using data-to-MC comparison of the  $p_T$  scale and resolution between  
<sub>1565</sub> the hard and soft  $E_T^{\text{miss}}$  components [117]. These uncertainties are represented by three  
<sub>1566</sub> independent terms: 1 for scale uncertainty and 2 for resolution uncertainty of the parallel  
<sub>1567</sub> and perpendicular components.

<sub>1568</sub> **7.2 Modeling uncertainties**

<sub>1569</sub> **7.2.1 Signal and irreducible background uncertainties**

<sub>1570</sub> The signal and background samples used are modeled using MC simulation. Most uncer-  
<sub>1571</sub> tainties on simulation parameters (e.g. generator choice, PS model) are estimated by varying  
<sub>1572</sub> the relevant parameters and comparing them with the nominal sample. Uncertainties in-  
<sub>1573</sub> volving PDF in particular for most processes in the analysis are set to a flat 1% uncertainty.  
<sub>1574</sub> Cross-section uncertainties were considered for all irreducible background except  $t\bar{t}W$ , which  
<sub>1575</sub> is normalized in dedicated CRs following section 6.3.3. Extra uncertainties for the produc-  
<sub>1576</sub> tion of four or more  $b$ -jets (additional  $b$ -jets) in association with  $t\bar{t}X$  and HF jets were also  
<sub>1577</sub> considered due to a lack of theoretical predictions or dedicated measurements, rendering  
<sub>1578</sub> MC modeling challenging. Uncertainties from missing higher-order QCD corrections in MC  
<sub>1579</sub> simulation are estimated by varying the renormalization scale  $\mu_R$  and factorization scale  $\mu_F$   
<sub>1580</sub> within seven different combinations

$$(\mu_R, \mu_F) = \{(0.5, 0.5), (0.5, 1), (1, 0.5), (1, 1), (1, 2), (2, 1), (2, 2)\}.$$

<sub>1581</sub> Process-specific uncertainty treatments are detailed below.

<sub>1582</sub> **SM  $t\bar{t}t\bar{t}$  background**

<sub>1583</sub> The generator uncertainty for the SM  $t\bar{t}t\bar{t}$  background was evaluated between a nominal  
<sub>1584</sub> sample of MADGRAPH5\_AMC@NLO and SHERPA. The parton shower uncertainty was  
<sub>1585</sub> evaluated between PYTHIA8 and HERWIG. The cross-section uncertainty was estimated to

1586 be 20% computed from a prediction at NLO in QCD+EW [126].

### 1587 $t\bar{t}t$ background

1588 The cross-section uncertainty for  $t\bar{t}t$  was estimated to be 30% computed from a prediction  
1589 at NLO in QCD+EW [126]. Events with additional  $b$ -jets also incur a 50% uncertainty.

### 1590 $t\bar{t}W$ , $t\bar{t}Z$ , $t\bar{t}H$ backgrounds

1591 For  $t\bar{t}W$ ,  $t\bar{t}Z$  and  $t\bar{t}H$  backgrounds, an uncertainty of 50% is assigned to events with one  
1592 additional truth  $b$ -jets that did not originate from a top quark decay, and an added 50%  
1593 uncertainty is assigned to events with two or more [156] additional  $b$ -jets. The generator  
1594 uncertainty was estimated for  $t\bar{t}Z$  using a MADGRAPH5\_AMC@NLO nominal sample and  
1595 a SHERPA sample, and for  $t\bar{t}H$  using POWHEGBOX samples interfaced with PYTHIA8 (nom-  
1596 inal) and HERWIG7. Cross-section uncertainties of 12% and 10% were applied to  $t\bar{t}Z$  and  
1597  $t\bar{t}H$  respectively [157]. No  $t\bar{t}W$  cross-section or PDF uncertainty was considered since the  
1598 normalizations and jet multiplicity spectrum for  $t\bar{t}W$  are estimated using the data-driven  
1599 method described in section 6.3.3.

### 1600 Other backgrounds

1601 Other backgrounds include processes with small overall contribution in the SR. The  
1602 cross-section uncertainty for  $tZ$  and  $tWH$  is considered to be 30% [158, 159]. A conservative  
1603 cross-section uncertainty of 50% is applied to  $t\bar{t}VV$ ,  $VVV$  and  $VH$ . For  $VV$ , the cross-  
1604 section uncertainty is dependent on jet multiplicity and is considered to be 20%/50%/60%  
1605 for events with  $\leq 3/4 \geq 5$  jets [160]. For  $VV$ ,  $t\bar{t}VV$ ,  $VVV$  and  $VH$  events with additional  
1606 truth  $b$ -jets, an uncertainty of 50% is applied.

## 1607 7.2.2 Reducible background uncertainties

1608 Reducible backgrounds consist of  $t\bar{t}/V + \text{HF}$  jets and single top events. Reducible back-  
1609 ground has small contamination within the SR, thus uncertainties related to reducible back-  
1610 ground have minor impact. Treatment for reducible background in this analysis largely  
1611 follows Ref. [44], except for QmisID.

## 1612 Charge misidentification

1613 Uncertainties on the QmisID background originate from the charge flip rates obtained  
1614 using the data-driven method described in section 6.3.2. Four sources of uncertainty were  
1615 considered: statistical uncertainty from the maximum LLH estimation using Equation 6.2;  
1616 uncertainty from choice of the  $Z$ -mass window and sidebands; non-closure uncertainty de-  
1617 fined as the relative difference between the number of SS and OS events; and statistical  
1618 uncertainty from the  $N_{\text{jets}}$  dependency correction SFs. The combined uncertainties from  
1619 all four sources are calculated separately for each region involved in section 6.3.2, and are  
1620 treated as correlated across all regions. Figure 7.1 shows the uncertainty calculated for SR.

## 1621 Internal (low $\gamma^*$ ) and material conversion

1622 The normalization for internal and material conversion backgrounds are free parameters  
1623 in the fit, as a result the only uncertainties evaluated are from the shape of the distributions  
1624 used in the template fit method (see section 6.3.1). The uncertainties on internal (material)  
1625 conversion are estimated based on the difference between data and MC prediction in a region  
1626 enriched in  $Z + \gamma \rightarrow \mu^+\mu^- + e^+e^-$  events.

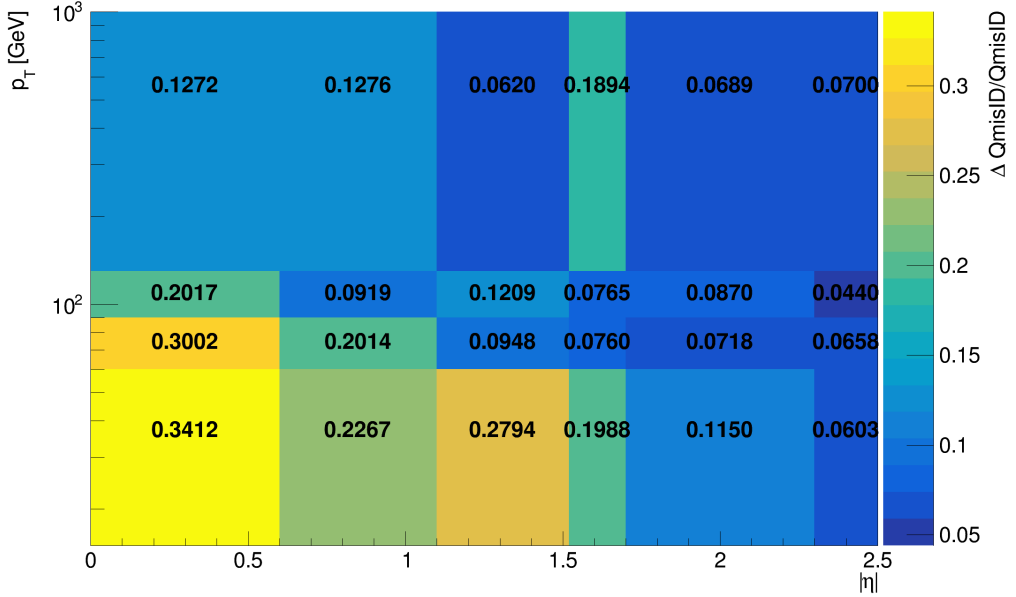


Figure 7.1: Combined QmisID uncertainty rate for SR in bins of  $|\eta|$  and  $p_T$ .

### <sup>1627</sup> Heavy-flavor non-prompt lepton

<sup>1628</sup> Similar to the conversion backgrounds, the uncertainties on non-prompt HF decays come  
<sup>1629</sup> from the shape of the distributions, and are estimated by comparing data and MC prediction  
<sup>1630</sup> between all regions in the analysis on a per bin basis. The events used are required to  
<sup>1631</sup> contain at least one *Loose* reconstructed lepton used in the region selection criteria detailed  
<sup>1632</sup> in Table 6.1 to maintain orthogonality with the SR.

### <sup>1633</sup> Light-flavor decays and other fake/non-prompt backgrounds

<sup>1634</sup> A conservative normalization uncertainty of 100% is assigned for light-flavor non-prompt  
<sup>1635</sup> lepton background [149], and an ad-hoc normalization uncertainty of 30% is applied to all  
<sup>1636</sup> other fake and non-prompt backgrounds. The shape uncertainties for these backgrounds are  
<sup>1637</sup> negligible.

<sub>1638</sub> **Chapter 8. Results**

<sub>1639</sub> **8.1 Statistical interpretation**

<sub>1640</sub> This section provides an overview of the statistical methods needed to interpret the  
<sub>1641</sub> collected and simulated data to estimate unknown physics parameters and determine com-  
<sub>1642</sub> patibility between data and the analysis hypothesis. For the BSM resonance search, the null  
<sub>1643</sub> hypothesis  $H_0$  assumes only SM background contributions and none from any new BSM  
<sub>1644</sub> resonance in the data.

<sub>1645</sub> **8.1.1 Profile likelihood fit**

<sub>1646</sub> Given a set of observed data points  $\mathbf{x} = [x_1, x_2, \dots]$  and unknown parameters  $\boldsymbol{\theta} =$   
<sub>1647</sub>  $[\theta_1, \theta_2, \dots, \theta_n]$ , the maximum likelihood method aims to find an estimate  $\hat{\boldsymbol{\theta}}$  that maximizes  
<sub>1648</sub> the joint probability function  $f(\mathbf{x}, \boldsymbol{\theta})$ , or in other words the set of parameters that gives the  
<sub>1649</sub> highest probability of observing the collected data points for a particular model. The func-  
<sub>1650</sub> tion to be maximized for this purpose is the log-likelihood (LLH) function  $\ln \mathcal{L}(\mathbf{x}, \boldsymbol{\theta})$  where  
<sub>1651</sub>  $\mathcal{L}(\mathbf{x}, \boldsymbol{\theta}) \equiv \prod_i f(x_i, \boldsymbol{\theta})$  is defined as the likelihood (LH) function. The LLH is maximized  
<sub>1652</sub> when  $\partial/\partial\theta_i (\ln \mathcal{L}) = 0$  for each parameter  $\theta_i$ .

<sub>1653</sub> For an usual binned physics analysis, the above variables for the LH function  $\mathcal{L}$  can  
<sub>1654</sub> be expressed as nuisance parameters (NP)  $\boldsymbol{\theta}$  and number of events for a model  $N_i(\mu)$  for  
<sub>1655</sub> the  $i^{\text{th}}$  bin, where  $\mu$  is the targeted parameter of interest (POI). In this analysis,  $N_i$  is  
<sub>1656</sub> assumed to follow a Poisson distribution and depends on the following quantities: the signal  
<sub>1657</sub> strength  $\mu$  defined as the ratio of observed to expected cross sections  $\sigma_{\text{obs}}/\sigma_{\text{exp}}$ ; nuisance  
<sub>1658</sub> parameters  $\boldsymbol{\theta}$  which represents the effects of systematic uncertainties, implemented in the

1659 LH function as Gaussian constraints; and normalization factors (NFs)  $\boldsymbol{\lambda}$  that control the  
 1660 normalization of background components that do not have a well-known cross section. The  
 1661 Poisson probability of observing exactly  $N_i$  events for an expected number of event  $n_i$  is

$$\mathcal{P}(N_i|n_i(\mu, \boldsymbol{\lambda})) = \frac{n_i^{N_i} e^{-n_i}}{N_i!}. \quad (8.1)$$

1662 The expected Poisson event number in a bin  $i$  can be parameterized as

$$n_i = \mu s_i(\boldsymbol{\theta}) + \sum_j \lambda_j b_{ij}(\boldsymbol{\theta}), \quad (8.2)$$

1663 where  $s_i$  is the number of signal events in bin  $i$  of every region, and  $b_{ij}$  is the number of  
 1664 events for a certain background source index  $j$  in bin  $i$ . The LH function in this analysis  
 1665 can be written as

$$\mathcal{L}(\mathbf{N}|\mu, \boldsymbol{\theta}, \boldsymbol{\lambda}) = \left( \prod_i \mathcal{P}(N_i|n_i) \right) \cdot \prod_k \mathcal{G}(\theta_k), \quad (8.3)$$

1666 where  $\mathcal{G}(\theta_k)$  is the Gaussian constraint for a NP  $k$ . The signal significance  $\mu$  and NFs  $\boldsymbol{\lambda}$  are  
 1667 left unconstrained and are fitted simultaneously in the profile LH fit. Define the profile LH  
 1668 ratio [161] as

$$\lambda(\mu) = \frac{\mathcal{L}(\mu, \hat{\boldsymbol{\theta}}_\mu, \hat{\boldsymbol{\lambda}}_\mu)}{\mathcal{L}(\hat{\mu}, \hat{\boldsymbol{\theta}}, \hat{\boldsymbol{\lambda}})}, \quad (8.4)$$

1669 where  $\hat{\mu}$ ,  $\hat{\boldsymbol{\theta}}$  and  $\hat{\boldsymbol{\lambda}}$  are parameter values that optimally maximizes the LH function, and  $\hat{\boldsymbol{\theta}}_\mu$ ,  
 1670  $\hat{\boldsymbol{\lambda}}_\mu$  are NP and NF values respectively that maximize the LH function for a given signal  
 1671 strength  $\mu$ . Using Neyman-Pearson lemma [162], the optimal test statistic for hypothesis  
 1672 testing is

$$q_\mu \equiv -2 \ln \lambda(\mu), \quad (8.5)$$

1673 where  $q_\mu = 0$  or  $\lambda(\mu) = 1$  corresponds to perfect agreement between the optimal parameter  
 1674  $\hat{\mu}$  obtained from data and the hypothesized value  $\mu$ . From Wilks' theorem [163], the test  
 1675 statistic  $q_\mu$  approaches a  $\chi^2$  distribution and can be evaluated as  $q_\mu = (\mu - \hat{\mu})^2 / \sigma_\mu^2$ .

1676 When evaluating against the background-only hypothesis ( $\mu = 0$ ), it can be assumed  
 1677 that the number of events observed under the signal hypothesis is higher than that of the  
 1678 background-only hypothesis, or  $\mu \geq 0$  according to Equation 8.2. This leads to a corre-  
 1679 sponding lower bound on the test statistic

$$q_0 = \begin{cases} -2 \ln \lambda(0), & \text{if } \hat{\mu} \geq 0, \\ 0, & \text{if } \hat{\mu} < 0. \end{cases} \quad (8.6)$$

### 1680 ***p*-value**

1681 To quantify the incompatibility between the observed data and the background-only hy-  
 1682 pothesis, the *p*-value is defined as  $p = P(q_\mu \geq q_{\mu, \text{obs}} | H_0)$  or in other words, the probability  
 1683 of observing data with a test statistic  $q_\mu$  under the null hypothesis  $H_0$  that is less compat-  
 1684 ible with  $H_0$  than the actual observed data with test statistic  $q_{\mu, \text{obs}}$ . The *p*-value can be  
 1685 expressed in terms of  $q_\mu$  as

$$p_\mu = \int_{q_{\mu, \text{obs}}}^{\infty} f(q_\mu | \mu) dq_\mu, \quad (8.7)$$

1686 where  $f(q_\mu | \mu) dq_\mu$  is the conditional probability density function of  $q_\mu$  given  $\mu$ .

1687 In some cases, it is more convenient to evaluate compatibility using the *Z*-value, defined  
 1688 as the number of standard deviations between the observed data and the mean in a Gaussian

1689 distribution. The  $p$ -value can be converted to  $Z$ -value via the relation

$$Z = \Phi^{-1}(1 - p), \quad (8.8)$$

1690 where  $\Phi$  is the quantile of the standard Gaussian. Rejecting the signal hypothesis usually  
1691 requires a 95% confidence level (CL) which corresponds to a  $p$ -value of 0.05 or a  $Z$ -value of  
1692 1.64, while rejecting the background-only hypothesis generally requires a  $Z$ -value of 5 or a  
1693  $p$ -value of  $2.84 \times 10^{-7}$ .

### 1694 8.1.2 Exclusion limit

1695 If the signal hypothesis is rejected, the exclusion upper limits can still be computed at  
1696 a certain CL (usually 95%) to establish the maximum value of  $\mu$  that is not excluded by  
1697 the observed data. The exclusion limits are calculated based on the  $\text{CL}_s$  method [164, 165]  
1698 under which the test statistic is defined as  $q_\mu = -2 \ln \frac{\mathcal{L}_{s+b}}{\mathcal{L}_b}$  with  $\mathcal{L}_{s+b}$  being the LH function  
1699 for the signal and background hypothesis ( $\mu > 0$ ) and  $\mathcal{L}_b$  being the LH function for the  
1700 background-only hypothesis ( $\mu = 0$ ). The  $p$ -value for both hypotheses can then be expressed  
1701 as

$$\begin{aligned} p_{s+b} &= P(q \geq q_{\text{obs}} | s + b) = \int_{q_{\text{obs}}}^{\infty} f(q | s + b) dq \\ p_b &= P(q \geq q_{\text{obs}} | b) = \int_{-\infty}^{q_{\text{obs}}} f(q | b) dq. \end{aligned} \quad (8.9)$$

1702 The signal hypothesis is excluded for a CL  $\alpha$  when the following condition is satisfied

$$\text{CL}_s \equiv \frac{p_{s+b}}{p_b} \geq 1 - \alpha. \quad (8.10)$$

1703 The value of  $\mu$  such that the signal hypothesis leads to  $\text{CL}_s = 1 - \alpha = 0.05$  is then the  
1704 exclusio upper limit at a 95% CL.

## 1705 8.2 Fit results

1706 The signal strength  $\mu$ , background NFs,  $t\bar{t}W$  scaling factors and uncertainty NPs are  
1707 simultaneously fitted using a binned profile LLH fit under the background-only hypothesis  
1708 to the  $H_T$  distribution in the SR and to corresponding distributions shown in Table 6.1 for  
1709 CRs.

1710 Before fitting to real data (unblinded fit), the fit was first performed in both the SR  
1711 and CRs using Asimov pseudo-datasets, in which the simulated data match exactly to MC  
1712 prediction with nominal  $\mu$  set to 0. This is done for the purpose of optimizing object selection  
1713 criteria and region definition, refining background estimation techniques and testing the  
1714 statistical interpretation model for signal extraction described in section 8.1. The fit is then  
1715 performed with Asimov data in the SR and real data in CRs to validate background modeling,  
1716 estimate sensitivity and assess the influence of statistical effects on fitted parameters. Finally,  
1717 the fully unblinded fit is performed with real data in all regions.

1718 The unblinded fit results are presented below. No significant excess over SM predictions  
1719 is observed, and the fitted signal strength  $\mu$  is compatible with zero for all  $Z'$  mass points.  
1720 Figure 8.1 shows the observed and expected upper limits at 95% confidence level on the  
1721 cross-section of  $pp \rightarrow t\bar{t}Z'$  production times the branching ratio of  $Z' \rightarrow t\bar{t}$  as a function of  
1722 the  $Z'$  resonance mass. The exclusion limits range from 7.9 fb to 9.44 fb depending on  $m_{Z'}$ .

1723 No significant variation is observed in fit output behavior using  $t\bar{t}Z'$  samples of different  
1724  $m_{Z'}$ ; results fitted using  $m_{Z'} = 2$  TeV are shown without substantial loss of generality.

1725 The background modeling is evaluated under the background-only hypothesis. The fitted  
1726 background NFs are shown in Table 8.1 and are consistent with their nominal values within  
1727 one standard deviation, or two standard deviations in the case of  $\text{NF}_{\text{HF } e}$  and  $\text{NF}_{t\bar{t}W+(4j)}$ .  
1728 Figure 8.2 shows good agreement between data and post-fit background distributions in  
1729 non-prompt background CRs and  $t\bar{t}W$  CRs.

1730 The pre-fit and post-fit background yields are shown in Table 8.2. Except for HF  $e$   
1731 background, post-fit yields for various backgrounds e.g.  $t\bar{t}t\bar{t}$ ,  $t\bar{t}H$ , other fake, etc. are  
1732 increased; the pre-fit to post-fit variations are consistent within  $\pm\sigma$ . Data and total post-fit  
1733 yields are also consistent within  $\pm\sigma$ . Post-fit yield for HF  $e$  background is lowered compared  
1734 to pre-fit yield within within  $2\sigma$  which can be related to the fitted value of  $\text{NF}_{\text{HF } e}$  in  
1735 Table 8.1; however, this difference in pre- and post-fit yields of HF  $e$  background has negligible  
1736 impact on the  $\mu$  as seen in Table 8.3.

1737 Table 8.3 outlines the impact on the signal strength  $\mu$  of various sources of uncertainty  
1738 grouped by their corresponding category. The background sources of uncertainty with the  
1739 largest impact is  $t\bar{t}t\bar{t}$  modeling, in particular  $t\bar{t}t\bar{t}$  generator choice and cross-section uncer-  
1740 tainties, followed by  $t\bar{t}W$  modeling due to their significant contributions in the SR observed  
1741 in Figure 6.1, especially in the more sensitive regions requiring three or more  $b$ -tagged jets.  
1742 The most significant impact on  $\mu$  within the set of instrumental uncertainties are uncertain-  
1743 ties on jet  $b$ -tagging attributable to the high jet and  $b$ -jet multiplicities in the BSM  $t\bar{t}t\bar{t}$  signal  
1744 signature.

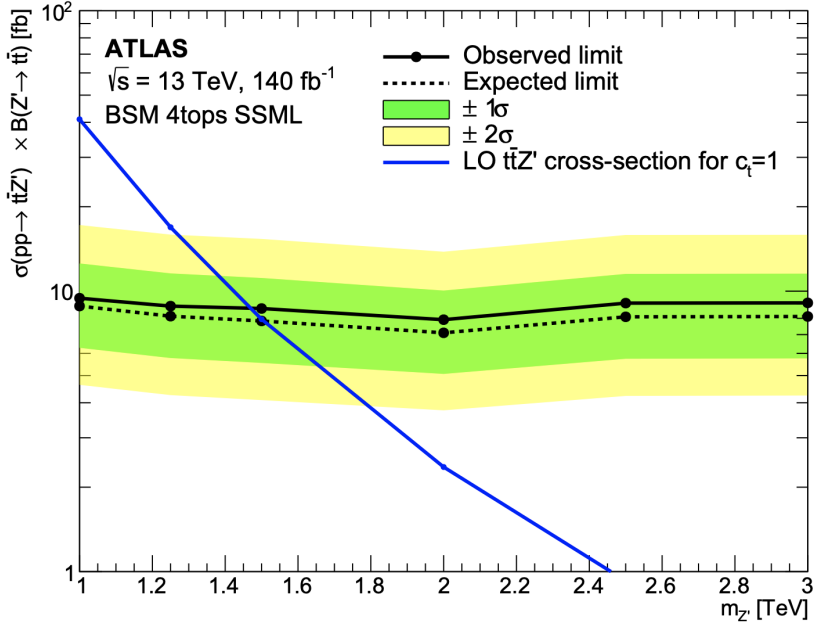


Figure 8.1: Observed (solid line) and expected (dotted line) upper limits as a function of the  $Z'$  mass at 95% CL on the cross-section of  $pp \rightarrow t\bar{t}Z'$  production times the  $Z' \rightarrow t\bar{t}$  branching ratio. The region above the observed limit is excluded. The solid blue line represents the theoretical signal cross-section with  $c_t = 1$  at LO in QCD [73]. The green and yellow bands represent the 68% ( $\pm\sigma$ ) and 95% ( $\pm 2\sigma$ ) confidence intervals respectively.

Table 8.1: Normalization factors for backgrounds with dedicated CRs, obtained from a simultaneous fit in all CRs and SR under the background-only hypothesis. The nominal pre-fit value is 1 for all NFs and 0 for the scaling factors  $a_0$  and  $a_1$ . Uncertainties shown include both statistical and systematic uncertainties.

Parameter	NF <sub>HF e</sub>	NF <sub>HF <math>\mu</math></sub>	NF <sub>Mat. Conv.</sub>	NF <sub>Low <math>m_{\gamma^*}</math></sub>	$a_0$	$a_1$	NF <sub><math>t\bar{t}W+(4j)</math></sub>	NF <sub><math>t\bar{t}W-(4j)</math></sub>
Fit value	$0.68^{+0.23}_{-0.22}$	$0.97^{+0.17}_{-0.16}$	$0.97^{+0.31}_{-0.28}$	$0.97^{+0.23}_{-0.20}$	$0.39^{+0.11}_{-0.11}$	$0.42^{+0.25}_{-0.24}$	$1.21^{+0.18}_{-0.18}$	$1.10^{+0.26}_{-0.26}$

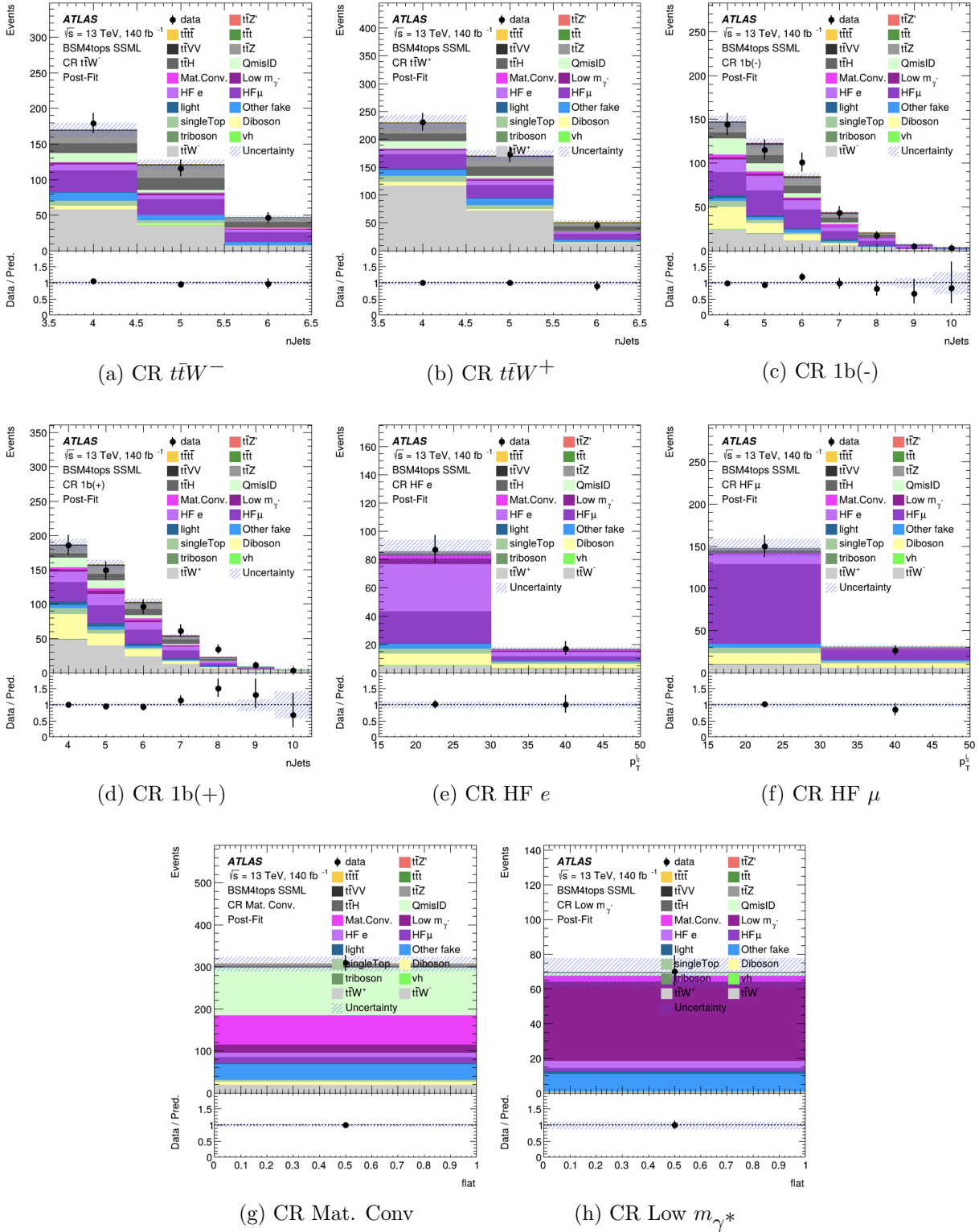


Figure 8.2: Comparison between data and post-fit prediction for the discriminant observable in each non-prompt and  $t\bar{t}W$  background CR. The fit is performed simultaneously in all CRs and SR under the background-only hypothesis. The lower panel shows the ratio between data and post-fit predictions. The shaded band represents the total uncertainty on the fit.

Table 8.2: Pre-fit and post-fit background yields in the inclusive SR. The number of data events and pre-fit estimate signal yields are also shown. Background yields shown are obtained from the fit using the  $t\bar{t}Z'$  signal sample with  $m_{Z'} = 2$  TeV. Pre-fit yields for  $t\bar{t}W$  background are set to 0 nominally prior to data-driven normalization. Total yield uncertainty differs from the quadrature sum of constituent uncertainties due to correlation and anticorrelation effects.

Process	Pre-fit	Post-fit
<b>Background</b>		
$t\bar{t}t\bar{t}$	$42.35 \pm 5.45$	$46.91 \pm 5.19$
$t\bar{t}W^+$	-	$103.93 \pm 15.91$
$t\bar{t}W^-$	-	$55.27 \pm 11.14$
$t\bar{t}Z$	$78.02 \pm 14.12$	$75.57 \pm 11.13$
$t\bar{t}H$	$81.00 \pm 7.10$	$82.90 \pm 7.30$
$t\bar{t}t$	$3.33 \pm 0.59$	$3.37 \pm 0.60$
Single-top ( $tq$ , $tZq$ , $tWZ$ , etc.)	$13.38 \pm 2.87$	$12.69 \pm 2.86$
$t\bar{t}VV/t\bar{t}VH/t\bar{t}HH$	$17.07 \pm 4.66$	$16.44 \pm 4.64$
Charge misidentification	$40.31 \pm 0.32$	$40.33 \pm 0.32$
$VV/VVV/VH$	$10.01 \pm 4.76$	$6.69 \pm 2.75$
Mat. Conv.	$26.20 \pm 0.91$	$25.76 \pm 6.06$
Low $m_{\gamma^*}$	$26.14 \pm 0.66$	$25.62 \pm 4.23$
HF $e$	$21.99 \pm 1.45$	$15.42 \pm 3.70$
HF $\mu$	$31.33 \pm 3.47$	$31.53 \pm 5.06$
Light-flavor decays	$13.47 \pm 0.53$	$13.54 \pm 0.53$
Other fake & non-prompt	$24.90 \pm 2.26$	$26.00 \pm 1.96$
Total background	-	$576.53 \pm 19.86$
<b>Signal <math>t\bar{t}Z' \rightarrow t\bar{t}t\bar{t}</math></b>		
$m_{Z'} = 1$ TeV	$52.83 \pm 1.41$	-
$m_{Z'} = 1.25$ TeV	$52.94 \pm 1.35$	-
$m_{Z'} = 1.5$ TeV	$53.07 \pm 1.47$	-
$m_{Z'} = 2$ TeV	$52.49 \pm 1.43$	-
$m_{Z'} = 2.5$ TeV	$53.07 \pm 1.47$	-
$m_{Z'} = 3$ TeV	$52.45 \pm 1.50$	-
<b>Data</b>	604	

Table 8.3: Post-fit impact of uncertainty sources on the signal strength  $\mu$ , grouped by categories. Values shown are obtained from the fit using the  $t\bar{t}Z'$  signal sample with  $m_{Z'} = 2$  TeV. Impact on  $\mu$  is evaluated for each uncertainty category by re-fitting with the corresponding set of NPs fixed to their best-fit values. Total uncertainty differs from the quadrature sum of constituent uncertainties due to correlation between NPs in the fit.

Uncertainty source	$\Delta\mu$	
<b>Signal modeling</b>		
$t\bar{t}Z'$	+0.00	-0.00
<b>Background modeling</b>		
$t\bar{t}\bar{t}$	+0.15	-0.13
$t\bar{t}W$	+0.04	-0.03
$t\bar{t}Z$	+0.02	-0.02
$t\bar{t}H$	+0.02	-0.02
Non-prompt leptons	+0.00	-0.00
Other backgrounds	+0.02	-0.02
<b>Instrumental</b>		
Luminosity	+0.00	-0.00
Jet uncertainties	+0.04	-0.04
Jet flavor tagging ( $b$ -jets)	+0.04	-0.04
Jet flavor tagging ( $c$ -jets)	+0.01	-0.01
Jet flavor tagging (light-jets)	+0.02	-0.01
MC simulation sample size	+0.01	-0.01
Other experimental uncertainties	+0.01	-0.01
Total systematic uncertainty	+0.15	-0.17
<b>Statistical</b>		
$t\bar{t}W$ NFs and scaling factors	+0.01	-0.01
Non-prompt lepton NFs (HF, Mat. Conv., Low $m_{\gamma^*}$ )	+0.00	-0.00
Total statistical uncertainty	+0.25	-0.23
<b>Total uncertainty</b>	+0.29	-0.29

# 1745 Chapter 9. Summary

1746 This dissertation presents a search for BSM top-philic heavy vector resonance based on a  
1747 simplified top-philic color singlet  $Z'(\rightarrow t\bar{t})$  model in the top-quark pair associated production  
1748 channel ( $t\bar{t}Z'$ ). The search is performed in the same-sign dilepton and multilepton channel  
1749 of the  $t\bar{t}t\bar{t}$  final states, using the full Run 2 data set collected between 2015 and 2018 by the  
1750 ATLAS detector at the LHC, corresponding to an integrated luminosity of  $140 \text{ fb}^{-1}$  of  $pp$   
1751 collisions at center-of-mass energy  $\sqrt{s} = 13 \text{ TeV}$ .

1752 New data-driven estimation methods for  $t\bar{t}W$  and charge misidentification background  
1753 are employed to improve background modeling and signal sensitivity compared to previous  
1754 analysis [28]. No significant excess over Standard Model predictions is observed. Observed  
1755 exclusion limits at 95% confidence level as a function of the  $Z'$  mass are set on the production  
1756 cross section of  $pp \rightarrow t\bar{t}Z'$  times the  $Z' \rightarrow t\bar{t}$  branching ratio, ranging from 7.9 fb to 9.4 fb  
1757 depending on the  $Z'$  mass. The analysis probes a  $Z'$  mass range from 1 TeV to 3 TeV under  
1758 the assumption of a top- $Z'$  coupling strength of  $c_t = 1$  and chirality angle  $\theta = \pi/4$ .

1759 Further improvements in analysis strategies, including multivariate techniques for signal  
1760 discrimination, are expected to increase discovery potential in future searches. Looking  
1761 forward, the upcoming Run 3 data with increased luminosity at  $\sqrt{s} = 13.6 \text{ TeV}$  along  
1762 with prospects of the High-Luminosity LHC will significantly enhance sensitivity to BSM  
1763 physics and offer more opportunities to explore top-philic resonances and other exciting new  
1764 phenomena.

# 1765 References

- 1766 [1] J. Schwinger. *On Quantum-Electrodynamics and the Magnetic Moment of the Elec-*  
tron. *Phys. Rev.* **73** (4 1948), pp. 416–417 (cit. on p. 1).
- 1767 [2] R. P. Feynman. *Space-Time Approach to Quantum Electrodynamics.* *Phys. Rev.* **76**  
(6 1949), pp. 769–789 (cit. on p. 1).
- 1768 [3] S. Tomonaga. *On a relativistically invariant formulation of the quantum theory of*  
wave fields. *Prog. Theor. Phys.* **1** (1946), pp. 27–42 (cit. on p. 1).
- 1769 [4] E. Fermi. *An attempt of a theory of beta radiation. I.* *Nuclear Physics B* **4** (1967).  
Translated from the original 1934 German article by C. P. Enz and C. H. Beck, pp. 1–  
27 (cit. on p. 1).
- 1770 [5] D. J. Griffiths. *Introduction to Elementary Particles.* 2nd. Weinheim: Wiley-VCH,  
2008. ISBN: 978-3-527-40601-2 (cit. on p. 1).
- 1771 [6] C. Yang and R. Mills. *Conservation of Isotopic Spin and Isotopic Gauge Invariance.*  
*Phys. Rev.* **96** (1 1954), pp. 191–195 (cit. on pp. 1, 10).
- 1772 [7] A. Milsted and T. J. Osborne. *Quantum Yang-Mills theory: An overview of a program.*  
*Phys. Rev. D* **98** (1 2018), p. 014505 (cit. on pp. 1, 10).

- 1781 [8] S. L. Glashow. *Partial-symmetries of weak interactions*. Nuclear Physics 22.4 (1961),  
1782 pp. 579–588. ISSN: 0029-5582 (cit. on p. 1).
- 1783 [9] D. J. Gross and F. Wilczek. *Ultraviolet Behavior of Non-Abelian Gauge Theories*.  
1784 Phys. Rev. Lett. 30 (26 1973), pp. 1343–1346 (cit. on p. 1).
- 1785 [10] H. D. Politzer. *Reliable Perturbative Results for Strong Interactions?* Phys. Rev. Lett.  
1786 30 (26 1973), pp. 1346–1349 (cit. on p. 1).
- 1787 [11] P. Higgs. *Broken symmetries and the masses of gauge bosons*. Phys. Rev. Lett. 13 (16  
1788 1964), pp. 508–509 (cit. on pp. 1, 14).
- 1789 [12] P. Higgs. *Broken symmetries, massless particles and gauge fields*. Physics Letters 12.2  
1790 (1964), pp. 132–133. ISSN: 0031-9163 (cit. on pp. 1, 14).
- 1791 [13] F. Englert and R. Brout. *Broken Symmetry and the Mass of Gauge Vector Mesons*.  
1792 Phys. Rev. Lett. 13 (9 1964), pp. 321–323 (cit. on pp. 1, 14).
- 1793 [14] S. Weinberg. *The making of the Standard Model*. The European Physical Journal C  
1794 34.1 (May 2004), 513. ISSN: 1434-6052. arXiv: hep-ph/0401010 [hep-ph] (cit. on  
1795 p. 2).
- 1796 [15] D. P. Barber et al. *Discovery of Three-Jet Events and a Test of Quantum Chromody-  
1797 namics at PETRA*. Phys. Rev. Lett. 43 (12 1979), pp. 830–833 (cit. on p. 2).
- 1798 [16] G. Arnison et al. *Experimental Observation of Isolated Large Transverse Energy Elec-  
1799 trons with Associated Missing Energy at  $\sqrt{s} = 540 \text{ GeV}$* . Phys. Lett. B 122 (1983),  
1800 pp. 103–116 (cit. on p. 2).

- 1801 [17] G. Arnison and others. *Experimental Observation of Lepton Pairs of Invariant Mass*  
1802       *Around  $95 \text{ GeV}/c^2$  at the CERN SPS Collider.* [Phys. Lett. B 126 \(1983\), pp. 398–410](#)  
1803       (cit. on p. 2).
- 1804 [18] CDF Collaboration. *Observation of Top Quark Production in  $\bar{p}p$  Collisions with the*  
1805       *Collider Detector at Fermilab.* [Phys. Rev. Lett. 74 \(14 1995\), pp. 2626–2631](#) (cit. on  
1806       p. 2).
- 1807 [19] DØ Collaboration. *Observation of the Top Quark.* [Phys. Rev. Lett. 74 \(14 1995\),](#)  
1808       pp. 2632–2637 (cit. on p. 2).
- 1809 [20] ATLAS Collaboration. *Observation of a new particle in the search for the Standard*  
1810       *Model Higgs boson with the ATLAS detector at the LHC.* [Phys. Lett. B 716 \(2012\),](#)  
1811       p. 1. arXiv: 1207.7214 [[hep-ex](#)] (cit. on pp. 2, 14).
- 1812 [21] CMS Collaboration. *Observation of a new boson at a mass of 125 GeV with the CMS*  
1813       *experiment at the LHC.* [Phys. Lett. B 716 \(2012\), p. 30.](#) arXiv: 1207.7235 [[hep-ex](#)]  
1814       (cit. on pp. 2, 14).
- 1815 [22] S. Navas et al. *Review of particle physics.* [Phys. Rev. D 110.3 \(2024\), p. 030001](#) (cit.  
1816       on pp. 2, 7, 8).
- 1817 [23] Y. Fukuda et al. *Evidence for Oscillation of Atmospheric Neutrinos.* [Phys. Rev. Lett.](#)  
1818       81 (8 1998), pp. 1562–1567 (cit. on p. 2).
- 1819 [24] M. Cristinziani and M. Mulders. *Top-quark physics at the Large Hadron Collider.*  
1820       Journal of Physics G: Nuclear and Particle Physics 44.6 (2017), p. 063001. arXiv:  
1821       1606.00327 [[hep-ex](#)] (cit. on pp. 2, 8).

- 1822 [25] ATLAS and CMS Collaborations. *Combination of inclusive top-quark pair production*  
1823 *cross-section measurements using ATLAS and CMS data at  $\sqrt{s} = 7$  and 8 TeV.* *JHEP*  
1824 **07** (2023), p. 213. arXiv: [2205.13830 \[hep-ex\]](#) (cit. on p. 3).
- 1825 [26] C. Degrande, J.-M. Grard, C. Grojean, F. Maltoni, and G. Servant. *Non-resonant new*  
1826 *physics in top pair production at hadron colliders.* *Journal of High Energy Physics*  
1827 **2011.3** (Mar. 2011). ISSN: 1029-8479. arXiv: [1010.6304 \[hep-ph\]](#) (cit. on p. 3).
- 1828 [27] ATLAS Collaboration. *The ATLAS Experiment at the CERN Large Hadron Collider.*  
1829 *JINST* **3** (2008), S08003 (cit. on pp. 3, 21, 24, 25, 27–31).
- 1830 [28] ATLAS Collaboration. *Search for top-philic heavy resonances in pp collisions at  $\sqrt{s} =$*   
1831 *13 TeV with the ATLAS detector.* *Eur. Phys. J. C* **84** (2024), p. 157. arXiv: [2304.01678 \[hep-ex\]](#) (cit. on pp. 3, 4, 18, 90).
- 1833 [29] H. P. Nilles. *Supersymmetry, Supergravity and Particle Physics.* *Phys. Rept.* **110**  
1834 (1984), pp. 1–162 (cit. on p. 3).
- 1835 [30] G. R. Farrar and P. Fayet. *Phenomenology of the Production, Decay, and Detection*  
1836 *of New Hadronic States Associated with Supersymmetry.* *Phys. Lett. B* **76** (1978),  
1837 pp. 575–579 (cit. on p. 3).
- 1838 [31] T. Plehn and T. M. P. Tait. *Seeking sgluons.* *Journal of Physics G: Nuclear and*  
1839 *Particle Physics* **36.7** (2009), p. 075001. arXiv: [0810.3919 \[hep-ph\]](#) (cit. on p. 3).
- 1840 [32] S. Calvet, B. Fuks, P. Gris, and L. Valry. *Searching for sgluons in multitop events*  
1841 *at a center-of-mass energy of 8 TeV.* *Journal of High Energy Physics* **2013.4** (Apr.  
1842 2013). ISSN: 1029-8479. arXiv: [1212.3360 \[hep-ph\]](#) (cit. on p. 3).

- 1843 [33] A. Pomarol and J. Serra. *Top quark compositeness: Feasibility and implications*. Phys-  
1844       ical Review D 78.7 (Oct. 2008). ISSN: 1550-2368. arXiv: 0806.3247 [hep-ph] (cit. on  
1845       p. 3).
- 1846 [34] K. Kumar, T. M. Tait, and R. Vega-Morales. *Manifestations of top compositeness at*  
1847       *colliders*. Journal of High Energy Physics 2009.05 (May 2009), 022022. ISSN: 1029-  
1848       8479. arXiv: 0901.3808 [hep-ph] (cit. on p. 3).
- 1849 [35] G. Banelli, E. Salvioni, J. Serra, T. Theil, and A. Weiler. *The present and future of*  
1850       *four top operators*. Journal of High Energy Physics 2021.2 (Feb. 2021). ISSN: 1029-  
1851       8479. arXiv: 2010.05915 [hep-ph] (cit. on p. 3).
- 1852 [36] R. Aoude, H. El Faham, F. Maltoni, and E. Vryonidou. *Complete SMEFT predictions*  
1853       *for four top quark production at hadron colliders*. Journal of High Energy Physics  
1854       2022.10 (Oct. 2022). ISSN: 1029-8479. arXiv: 2208.04962 [hep-ph] (cit. on p. 3).
- 1855 [37] C. Zhang. *Constraining qqtt operators from four-top production: a case for enhanced*  
1856       *EFT sensitivity*. Chinese Physics C 42.2 (Feb. 2018), p. 023104. ISSN: 1674-1137.  
1857       arXiv: 1708.05928 [hep-ph] (cit. on p. 3).
- 1858 [38] L. Darmé, B. Fuks, and F. Maltoni. *Topophilic heavy resonances in four-top final*  
1859       *states and their EFT interpretation*. Journal of High Energy Physics 2021.9 (Sept.  
1860       2021). ISSN: 1029-8479. arXiv: 2104.09512 [hep-ph] (cit. on pp. 3, 17).
- 1861 [39] N. Craig, F. D'Eramo, P. Draper, S. Thomas, and H. Zhang. *The Hunt for the Rest*  
1862       *of the Higgs Bosons*. JHEP 06 (2015), p. 137. arXiv: 1504.04630 [hep-ph] (cit. on  
1863       pp. 3, 17).

- 1864 [40] N. Craig, J. Hajer, Y.-Y. Li, T. Liu, and H. Zhang. *Heavy Higgs bosons at low  $\tan \beta$ :  
1865 from the LHC to 100 TeV*. *Journal of High Energy Physics* 2017.1 (Jan. 2017). ISSN:  
1866 1029-8479. arXiv: [1605.08744 \[hep-ph\]](#) (cit. on pp. 3, 17).
- 1867 [41] G. C. Branco et al. *Theory and phenomenology of two-Higgs-doublet models*. *Phys.  
1868 Rept.* 516 (2012), pp. 1–102. arXiv: [1106.0034 \[hep-ph\]](#) (cit. on pp. 3, 17).
- 1869 [42] S. Gori, I.-W. Kim, N. R. Shah, and K. M. Zurek. *Closing the wedge: Search strategies  
1870 for extended Higgs sectors with heavy flavor final states*. *Phys. Rev. D* 93 (7 2016),  
1871 p. [075038](#) (cit. on pp. 3, 17).
- 1872 [43] P. S. B. Dev and A. Pilaftsis. *Maximally symmetric two Higgs doublet model with  
1873 natural Standard Model alignment*. *Journal of High Energy Physics* 2014.12 (Dec.  
1874 2014), p. 024. arXiv: [1408.3405 \[hep-ph\]](#) (cit. on pp. 3, 17).
- 1875 [44] ATLAS Collaboration. *Observation of four-top-quark production in the multilepton  
1876 final state with the ATLAS detector*. *Eur. Phys. J. C* 83 (2023), p. 496. arXiv: [2303.  
1877 15061 \[hep-ex\]](#) (cit. on pp. 3, 4, 18, 50, 64, 70, 78).
- 1878 [45] N. Greiner, K. Kong, J.-C. Park, S. C. Park, and J.-C. Winter. *Model-independent  
1879 production of a topophilic resonance at the LHC*. *Journal of High Energy Physics*  
1880 2015.4 (2015), p. 29. ISSN: 1029-8479. arXiv: [1410.6099 \[hep-ph\]](#) (cit. on pp. 3, 18,  
1881 19).
- 1882 [46] ATLAS Collaboration. *Evidence for  $t\bar{t}t\bar{t}$  production in the multilepton final state in  
1883 proton–proton collisions at  $\sqrt{s} = 13\text{TeV}$  with the ATLAS detector*. *Eur. Phys. J. C*  
1884 80 (2020), p. 1085. arXiv: [2007.14858 \[hep-ex\]](#) (cit. on pp. 4, 70).
- 1885 [47] D. H. Perkins. *Introduction to High Energy Physics*. 4th. Cambridge, UK: Cambridge  
1886 University Press, Apr. 2000. ISBN: 9780521621960 (cit. on p. 5).

- 1887 [48] C. Burgard and D. Galbraith. *Standard Model of Physics*. URL: <https://texample.net/model-physics/> (visited on 06/02/2025) (cit. on p. 6).
- 1888
- 1889 [49] H. Georgi. *Lie Algebras in Particle Physics: from Isospin to Unified Theories*. 2nd.
- 1890 CRC Press, 2000. ISBN: 9780429499210 (cit. on pp. 7, 10).
- 1891 [50] ATLAS and CMS Collaborations. *Combination of Measurements of the Top Quark*
- 1892 *Mass from Data Collected by the ATLAS and CMS Experiments at  $\sqrt{s} = 7$  and 8 TeV*.
- 1893 Phys. Rev. Lett. 132 (2023), p. 261902. arXiv: 2402.08713 [hep-ex] (cit. on p. 8).
- 1894 [51] H. de la Torre and T. Farooque. *Looking beyond the Standard Model with Third Gen-*
- 1895 *eration Quarks at the LHC*. Symmetry 14.3 (2022), p. 444 (cit. on p. 8).
- 1896 [52] Q.-H. Cao, J.-N. Fu, Y. Liu, X.-H. Wang, and R. Zhang. *Probing Top-philic New*
- 1897 *Physics via Four-Top-Quark Production*. Chinese Physics C 45.9 (2021), p. 093107.
- 1898 arXiv: 2105.03372 [hep-ph] (cit. on p. 8).
- 1899 [53] H. Beauchesne et al. *A case study about BSM vector resonances with direct couplings*
- 1900 *to the third quark generation*. European Physical Journal C 80.5 (2020), p. 485. arXiv:
- 1901 1908.11619 [hep-ph] (cit. on p. 8).
- 1902 [54] F. Maltoni, D. Pagani, and S. Tentori. *Top-quark pair production as a probe of light*
- 1903 *top-philic scalars and anomalous Higgs interactions*. Journal of High Energy Physics
- 1904 2024.9 (Sept. 2024), p. 098. arXiv: 2406.06694 [hep-ph] (cit. on p. 8).
- 1905 [55] CMS Collaboration. *Search for  $t\bar{t}H$  production in the  $H \rightarrow b\bar{b}$  decay channel with*
- 1906 *leptonic  $t\bar{t}$  decays in proton–proton collisions at  $\sqrt{s} = 13$  TeV*. JHEP 03 (2019),
- 1907 p. 026. arXiv: 1804.03682 [hep-ex] (cit. on p. 8).

- 1908 [56] Y. Grossman and Y. Nir. *The Standard Model: From Fundamental Symmetries to Ex-*  
1909 *perimental Tests*. See Chapter 8.2. Cambridge University Press, 2023. ISBN: 9781009320378  
1910 (cit. on p. 9).
- 1911 [57] M. E. Peskin and D. V. Schroeder. *An Introduction to Quantum Field Theory*. 1st.  
1912 Reading, MA, USA: AddisonWesley, 1995. ISBN: 978-0-201-50397-5 (cit. on p. 9).
- 1913 [58] D. J. Gross. *The role of symmetry in fundamental physics*. Proceedings of the National  
1914 Academy of Sciences of the United States of America 93.25 (Dec. 1996), pp. 14256–  
1915 14259 (cit. on p. 9).
- 1916 [59] M. Bañados and I. Reyes. *A short review on Noethers theorems, gauge symmetries*  
1917 *and boundary terms*. International Journal of Modern Physics D 25.10 (Aug. 2016),  
1918 p. 1630021. ISSN: 1793-6594. arXiv: 1601.03616 [hep-th] (cit. on p. 9).
- 1919 [60] A. Pich. *The Standard Model of electroweak interactions. 2004 European School of*  
1920 *High-Energy Physics*. Feb. 2005, pp. 1–48. arXiv: hep-ph/0502010 [hep-ex] (cit. on  
1921 pp. 11–13).
- 1922 [61] P. Dev and A. Pilaftsis. *High-temperature electroweak symmetry non-restoration from*  
1923 *new fermions and implications for baryogenesis*. Journal of High Energy Physics  
1924 2020.9 (Sept. 2020), p. 012. arXiv: 2002.05174 [hep-ph] (cit. on p. 13).
- 1925 [62] J. Riebesell. *Higgs Potential*. URL: <https://tikz.net/higgs-potential/> (visited on  
1926 07/07/2025) (cit. on p. 15).
- 1927 [63] J. Goldstone, A. Salam, and S. Weinberg. *Broken Symmetries*. Phys. Rev. 127 (3  
1928), pp. 965–970 (cit. on p. 15).
- 1929 [64] J. Ellis. *Higgs Physics. 2013 European School of High-Energy Physics*. 2015, pp. 117–  
1930 168. arXiv: 1312.5672 [hep-ph] (cit. on pp. 15, 16).

- 1931 [65] G. Ferretti and D. Karateev. *Fermionic UV completions of composite Higgs models*.  
1932 Journal of High Energy Physics 2014.3 (Mar. 2014). ISSN: 1029-8479 (cit. on p. 17).
- 1933 [66] L. Vecchi. *A dangerous irrelevant UV-completion of the composite Higgs*. JHEP 02  
1934 (2017), p. 094. arXiv: 1506.00623 [hep-ph] (cit. on p. 17).
- 1935 [67] CDF Collaboration. *Search for New Physics in High-Mass Electron-Positron Events*  
1936 *in  $p\bar{p}$  Collisions at  $\sqrt{s} = 1.96$  TeV*. Phys. Rev. Lett. 99 (17 2007), p. 171802. arXiv:  
1937 0707.2524 [hep-ex] (cit. on p. 17).
- 1938 [68] M. Battaglia and G. Servant. *Four-top production and  $t\bar{t}$ +missing energy events at*  
1939 *multi TeV  $e^+e^-$  colliders*. Nuovo Cim. C 033N2 (2010), pp. 203–208. arXiv: 1005.4632  
1940 [hep-ex] (cit. on p. 17).
- 1941 [69] N. Arkani-Hamed, A. G. Cohen, and H. Georgi. *Electroweak symmetry breaking from*  
1942 *dimensional deconstruction*. Physics Letters B 513.1-2 (July 2001), pp. 232–240. arXiv:  
1943 hep-ph/0105239 [hep-ph] (cit. on p. 17).
- 1944 [70] T. Han, H. E. Logan, B. McElrath, and L.-T. Wang. *Phenomenology of the little Higgs*  
1945 *model*. Phys. Rev. D 67 (9 2003), p. 095004. arXiv: hep-ph/0301040 [hep-ph] (cit. on  
1946 p. 17).
- 1947 [71] P. Langacker and M. Plümacher. *Flavor changing effects in theories with a heavy  $Z'$*   
1948 *boson with family nonuniversal couplings*. Phys. Rev. D 62 (1 2000), p. 013006. arXiv:  
1949 hep-ph/0001204 [hep-ph] (cit. on p. 17).
- 1950 [72] P. Langacker. *The Physics of Heavy  $Z'$  Gauge Bosons*. Rev. Mod. Phys. 81 (2009),  
1951 pp. 1199–1228. arXiv: 0801.1345 [hep-ph] (cit. on p. 17).

- 1952 [73] J. H. Kim, K. Kong, S. J. Lee, and G. Mohlabeng. *Probing TeV scale top-philic*  
1953 *resonances with boosted top-tagging at the high luminosity LHC*. *Phys. Rev. D* **94** (3  
1954 2016), p. 035023. arXiv: [1604.07421 \[hep-ph\]](https://arxiv.org/abs/1604.07421) (cit. on pp. 17, 18, 86).
- 1955 [74] P. J. Fox, I. Low, and Y. Zhang. *Top-philic Z' forces at the LHC*. *Journal of High*  
1956 *Energy Physics* **2018**.3 (Mar. 2018). ISSN: 1029-8479. arXiv: [1801.03505 \[hep-ph\]](https://arxiv.org/abs/1801.03505)  
1957 (cit. on p. 17).
- 1958 [75] CMS Collaboration. *Observation of four top quark production in proton-proton col-*  
1959 *lisions at  $\sqrt{s} = 13\text{TeV}$* . *Physics Letters B* **847** (2023), p. 138290. arXiv: [2305.13439](https://arxiv.org/abs/2305.13439)  
1960 [[hep-ex](https://arxiv.org/abs/2305.13439)] (cit. on p. 18).
- 1961 [76] P. Sabatini. *Evidence for four-top-quarks production with the ATLAS detector at the*  
1962 *Large Hadron Collider*. Tech. rep. Geneva: CERN, 2021. URL: <https://cds.cern.ch/record/2784150> (cit. on p. 20).
- 1964 [77] L. Evans and P. Bryant. *LHC Machine*. *JINST* **3** (2008), S08001 (cit. on p. 21).
- 1965 [78] CMS Collaboration. *The CMS Experiment at the CERN LHC*. *JINST* **3** (2008),  
1966 S08004 (cit. on p. 21).
- 1967 [79] The ALICE Collaboration. *The ALICE experiment at the CERN LHC*. *JINST* **3**  
1968 (2008), S08002 (cit. on p. 21).
- 1969 [80] The LHCb Collaboration. *The LHCb Detector at the LHC*. *JINST* **3** (2008), S08005  
1970 (cit. on p. 21).
- 1971 [81] E. e. a. Gschwendtner. *AWAKE, The Advanced Proton Driven Plasma Wakefield*  
1972 *Acceleration Experiment at CERN*. *Nuclear Instruments and Methods in Physics Re-*  
1973 *search Section A* **829** (2016), pp. 76–82. arXiv: [1512.05498 \[physics.acc-ph\]](https://arxiv.org/abs/1512.05498) (cit. on  
1974 p. 22).

- 1975 [82] J. L. Feng, I. Galon, F. Kling, and S. Trojanowski. *ForwArd Search ExpeRiment at*  
1976 *the LHC*. Phys. Rev. D 97 (3 2018), p. 035001. arXiv: 1708.09389 [hep-ph] (cit. on  
1977 p. 22).
- 1978 [83] The KATRIN collaboration. *The design, construction, and commissioning of the KA-*  
1979 *TRIN experiment*. Journal of Instrumentation 16.08 (2021), T08015. arXiv: 2103.  
1980 04755 [physics.ins-det] (cit. on p. 22).
- 1981 [84] E. Lopienska. *The CERN accelerator complex, layout in 2022*. General Photo. 2022.  
1982 URL: <https://cds.cern.ch/record/2800984> (visited on 07/08/2025) (cit. on p. 22).
- 1983 [85] High Luminosity LHC Project Organization. *The HL-LHC project*. 2025. URL: <https://hilumilhc.web.cern.ch/content/hl-lhc-project> (visited on 06/11/2025) (cit. on  
1984 p. 23).
- 1985 [86] ATLAS Collaboration. *Performance of the ATLAS detector using first collision data*.  
1986 JHEP 09 (2010), p. 056. arXiv: 1005.5254 [hep-ex] (cit. on p. 23).
- 1987 [87] ATLAS Collaboration. *Luminosity determination in pp collisions at  $\sqrt{s} = 13 \text{ TeV}$*   
1988 *using the ATLAS detector at the LHC*. Eur. Phys. J. C 83 (2023), p. 982. arXiv:  
1989 2212.09379 [hep-ex] (cit. on pp. 24, 50, 72).
- 1990 [88] J. M. Butterworth, G. Dissertori, and G. P. Salam. *Hard Processes in Proton-Proton*  
1991 *Collisions at the Large Hadron Collider*. Annu. Rev. Nucl. Part. Sci. 62 (2012),  
1992 pp. 387–405. arXiv: 1202.0583 [hep-ex] (cit. on p. 24).
- 1993 [89] J. Campbell, J. Huston, and W. J. Stirling. *Hard interactions of quarks and gluons:*  
1994 *a primer for LHC physics*. Reports on Progress in Physics 70.1 (2006), p. 89. arXiv:  
1995 hep-ph/0611148 [hep-ex] (cit. on p. 24).

- 1997 [90] ATLAS Collaboration. *Standard Model Summary Plots October 2023*. ATL-PHYS-  
1998 PUB-2023-039. 2023. URL: <https://cds.cern.ch/record/2882448> (cit. on p. 25).
- 1999 [91] J. Pequenao and P. Schaffner. *How ATLAS detects particles: diagram of particle  
2000 paths in the detector*. 2013. URL: <https://cds.cern.ch/record/1505342> (visited on  
2001 07/08/2025) (cit. on p. 26).
- 2002 [92] J. Pequenao. *Computer generated image of the ATLAS inner detector*. 2008. URL:  
2003 <https://cds.cern.ch/record/1095926> (visited on 07/08/2025) (cit. on p. 27).
- 2004 [93] J. Pequenao. *Computer Generated image of the ATLAS calorimeter*. 2008. URL: <https://cds.cern.ch/record/1095927> (visited on 07/08/2025) (cit. on p. 29).
- 2006 [94] ATLAS Collaboration. *Operation of the ATLAS trigger system in Run 2*. **JINST** 15  
2007 (2020), P10004. arXiv: [2007.12539 \[physics.ins-det\]](https://arxiv.org/abs/2007.12539) (cit. on p. 32).
- 2008 [95] ATLAS Collaboration. *Performance of the ATLAS track reconstruction algorithms  
2009 in dense environments in LHC Run 2*. **Eur. Phys. J. C** 77 (2017), p. 673. arXiv:  
2010 [1704.07983 \[hep-ex\]](https://arxiv.org/abs/1704.07983) (cit. on p. 33).
- 2011 [96] T. Cornelissen et al. *Concepts, design and implementation of the ATLAS New Track-  
2012 ing (NEWT)*. Tech. rep. Geneva: CERN, 2007. URL: <https://cds.cern.ch/record/1020106> (cit. on p. 33).
- 2014 [97] A. Salzburger. *Optimisation of the ATLAS Track Reconstruction Software for Run-2*.  
2015 **Journal of Physics: Conference Series** 664.7 (2015), p. 072042 (cit. on p. 33).
- 2016 [98] R. Frühwirth. *Application of Kalman filtering to track and vertex fitting*. **Nucl. In-**  
2017 **strum. Methods Phys. Res. A** 262.2 (1987), pp. 444–450. ISSN: 0168-9002 (cit. on  
2018 p. 33).

- 2019 [99] T. Cornelissen et al. *The global  $\chi^2$  track fitter in ATLAS*. Journal of Physics: Conference Series 119.3 (2008), p. 032013 (cit. on p. 33).
- 2020
- 2021 [100] ATLAS Collaboration. *Improved electron reconstruction in ATLAS using the Gaussian Sum Filter-based model for bremsstrahlung*. ATLAS-CONF-2012-047. 2012. URL: <https://cds.cern.ch/record/1449796> (cit. on p. 33).
- 2022
- 2023
- 2024 [101] D. Wicke. *A new algorithm for solving tracking ambiguities*. Tech. rep. Oct. 1998.
- 2025 URL: <https://cds.cern.ch/record/2625731> (cit. on p. 34).
- 2026 [102] ATLAS Collaboration. *Reconstruction of primary vertices at the ATLAS experiment in Run 1 proton–proton collisions at the LHC*. Eur. Phys. J. C 77 (2017), p. 332.
- 2027
- 2028 arXiv: [1611.10235 \[physics.ins-det\]](https://arxiv.org/abs/1611.10235) (cit. on p. 34).
- 2029 [103] W. Waltenberger, R. Frühwirth, and P. Vanlaer. *Adaptive vertex fitting*. Journal of
- 2030 Physics G: Nuclear and Particle Physics 34.12 (2007), N343 (cit. on p. 34).
- 2031 [104] ATLAS Collaboration. *Secondary vertex finding for jet flavour identification with the*
- 2032 *ATLAS detector*. ATL-PHYS-PUB-2017-011. 2017. URL: <https://cds.cern.ch/record/2270366> (cit. on p. 34).
- 2033
- 2034 [105] ATLAS Collaboration. *Performance of pile-up mitigation techniques for jets in pp*
- 2035 *collisions at  $\sqrt{s} = 8 \text{ TeV}$  using the ATLAS detector*. Eur. Phys. J. C 76 (2016),
- 2036 p. 581. arXiv: [1510.03823 \[hep-ex\]](https://arxiv.org/abs/1510.03823) (cit. on pp. 35, 38).
- 2037 [106] ATLAS Collaboration. *Topological cell clustering in the ATLAS calorimeters and its*
- 2038 *performance in LHC Run 1*. Eur. Phys. J. C 77 (2017), p. 490. arXiv: [1603.02934 \[hep-ex\]](https://arxiv.org/abs/1603.02934) (cit. on pp. 35, 36).
- 2039

- 2040 [107] ATLAS Collaboration. *Jet reconstruction and performance using particle flow with*  
2041 *the ATLAS Detector.* *Eur. Phys. J. C* **77** (2017), p. 466. arXiv: [1703.10485 \[hep-ex\]](#)  
2042 (cit. on p. 37).
- 2043 [108] M. Cacciari, G. P. Salam, and G. Soyez. *The anti- $k_t$  jet clustering algorithm.* *JHEP*  
2044 **04** (2008), p. 063. arXiv: [0802.1189 \[hep-ph\]](#) (cit. on p. 37).
- 2045 [109] ATLAS Collaboration. *Jet energy scale and resolution measured in proton–proton*  
2046 *collisions at  $\sqrt{s} = 13\text{ TeV}$  with the ATLAS detector.* *Eur. Phys. J. C* **81** (2021),  
2047 p. 689. arXiv: [2007.02645 \[hep-ex\]](#) (cit. on pp. 38, 73–75).
- 2048 [110] ATLAS Collaboration. *Jet energy scale measurements and their systematic uncertainties*  
2049 *in proton–proton collisions at  $\sqrt{s} = 13\text{ TeV}$  with the ATLAS detector.* *Phys. Rev.*  
2050 **D 96** (2017), p. 072002. arXiv: [1703.09665 \[hep-ex\]](#) (cit. on pp. 38, 73).
- 2051 [111] ATLAS Collaboration. *Transforming jet flavour tagging at ATLAS.* Tech. rep. Sub-  
2052 mitted to: Nature Communications. Geneva: CERN, 2025. arXiv: [2505.19689](#) (cit. on  
2053 pp. 39–41).
- 2054 [112] A. Vaswani et al. *Attention Is All You Need.* 2023. arXiv: [1706.03762 \[cs.CL\]](#) (cit. on  
2055 p. 39).
- 2056 [113] ATLAS Collaboration. *Measurements of  $b$ -jet tagging efficiency with the ATLAS de-*  
2057 *tector using  $t\bar{t}$  events at  $\sqrt{s} = 13\text{ TeV}.$*  *JHEP* **08** (2018), p. 089. arXiv: [1805.01845](#)  
2058 [[hep-ex](#)] (cit. on pp. 41, 75).
- 2059 [114] ATLAS Collaboration. *Electron reconstruction and identification in the ATLAS ex-*  
2060 *periment using the 2015 and 2016 LHC proton–proton collision data at  $\sqrt{s} = 13\text{ TeV}.$*   
2061 *Eur. Phys. J. C* **79** (2019), p. 639. arXiv: [1902.04655 \[physics.ins-det\]](#) (cit. on  
2062 pp. 42–44).

- 2063 [115] ATLAS Collaboration. *Muon reconstruction and identification efficiency in ATLAS*  
2064 *using the full Run 2 pp collision data set at  $\sqrt{s} = 13 \text{ TeV}$* . *Eur. Phys. J. C* **81** (2021),  
2065 p. 578. arXiv: 2012.00578 [hep-ex] (cit. on pp. 45, 46).
- 2066 [116] ATLAS Collaboration. *Muon reconstruction performance of the ATLAS detector in*  
2067 *proton–proton collision data at  $\sqrt{s} = 13 \text{ TeV}$* . *Eur. Phys. J. C* **76** (2016), p. 292. arXiv:  
2068 1603.05598 [hep-ex] (cit. on p. 46).
- 2069 [117] ATLAS Collaboration. *Performance of missing transverse momentum reconstruction*  
2070 *with the ATLAS detector using proton–proton collisions at  $\sqrt{s} = 13 \text{ TeV}$* . *Eur. Phys.*  
2071 *J. C* **78** (2018), p. 903. arXiv: 1802.08168 [hep-ex] (cit. on pp. 47, 75).
- 2072 [118] ATLAS Collaboration.  *$E_T^{\text{miss}}$  performance in the ATLAS detector using 2015–2016*  
2073 *LHC pp collisions*. ATLAS-CONF-2018-023. 2018. URL: <https://cds.cern.ch/record/2625233> (cit. on p. 48).
- 2075 [119] J. Alwall et al. *The automated computation of tree-level and next-to-leading order*  
2076 *differential cross sections, and their matching to parton shower simulations*. *JHEP* **07**  
2077 (2014), p. 079. arXiv: 1405.0301 [hep-ph] (cit. on pp. 51, 53–56).
- 2078 [120] NNPDF Collaboration, R. D. Ball, et al. *Parton distributions for the LHC run II*.  
2079 *JHEP* **04** (2015), p. 040. arXiv: 1410.8849 [hep-ph] (cit. on pp. 51, 53–57).
- 2080 [121] T. Sjöstrand et al. *An introduction to PYTHIA 8.2*. *Comput. Phys. Commun.* **191**  
2081 (2015), p. 159. arXiv: 1410.3012 [hep-ph] (cit. on pp. 51, 53–57).
- 2082 [122] ATLAS Collaboration. *ATLAS Pythia 8 tunes to 7 TeV data*. ATL-PHYS-PUB-2014-  
2083 021. 2014. URL: <https://cds.cern.ch/record/1966419> (cit. on pp. 53–57).

- 2084 [123] S. Frixione, E. Laenen, P. Motylinski, and B. R. Webber. *Angular correlations of*  
 2085 *lepton pairs from vector boson and top quark decays in Monte Carlo simulations.*  
 2086 JHEP 04 (2007), p. 081. arXiv: [hep-ph/0702198](#) (cit. on p. 53).
- 2087 [124] P. Artoisenet, R. Frederix, O. Mattelaer, and R. Rietkerk. *Automatic spin-entangled*  
 2088 *decays of heavy resonances in Monte Carlo simulations.* JHEP 03 (2013), p. 015.  
 2089 arXiv: [1212.3460 \[hep-ph\]](#) (cit. on p. 53).
- 2090 [125] D. J. Lange. *The EvtGen particle decay simulation package.* Nucl. Instrum. Meth. A  
 2091 462 (2001), p. 152 (cit. on p. 53).
- 2092 [126] R. Frederix, D. Pagani, and M. Zaro. *Large NLO corrections in  $t\bar{t}W^\pm$  and  $t\bar{t}t\bar{t}$*   
 2093 *hadroproduction from supposedly subleading EW contributions.* JHEP 02 (2018), p. 031.  
 2094 arXiv: [1711.02116 \[hep-ph\]](#) (cit. on pp. 53, 77).
- 2095 [127] E. Bothmann et al. *Event generation with Sherpa 2.2.* SciPost Phys. 7.3 (2019), p. 034.  
 2096 arXiv: [1905.09127 \[hep-ph\]](#) (cit. on pp. 53, 54, 56).
- 2097 [128] S. Schumann and F. Krauss. *A parton shower algorithm based on Catani–Seymour*  
 2098 *dipole factorisation.* JHEP 03 (2008), p. 038. arXiv: [0709.1027 \[hep-ph\]](#) (cit. on  
 2099 pp. 53, 56, 57).
- 2100 [129] S. Höche, F. Krauss, M. Schönherr, and F. Siegert. *A critical appraisal of NLO+PS*  
 2101 *matching methods.* JHEP 09 (2012), p. 049. arXiv: [1111.1220 \[hep-ph\]](#) (cit. on pp. 53,  
 2102 56, 57).
- 2103 [130] S. Höche, F. Krauss, M. Schönherr, and F. Siegert. *QCD matrix elements + parton*  
 2104 *showers. The NLO case.* JHEP 04 (2013), p. 027. arXiv: [1207.5030 \[hep-ph\]](#) (cit. on  
 2105 pp. 53, 56, 57).

- 2106 [131] S. Catani, F. Krauss, B. R. Webber, and R. Kuhn. *QCD Matrix Elements + Parton*  
 2107 *Showers*. JHEP 11 (2001), p. 063. arXiv: [hep-ph/0109231](#) (cit. on pp. 53, 56, 57).
- 2108 [132] S. Höche, F. Krauss, S. Schumann, and F. Siegert. *QCD matrix elements and truncated*  
 2109 *showers*. JHEP 05 (2009), p. 053. arXiv: [0903.1219 \[hep-ph\]](#) (cit. on pp. 53, 56, 57).
- 2110 [133] F. Caccioli, P. Maierhöfer, and S. Pozzorini. *Scattering Amplitudes with Open Loops*.  
 2111 Phys. Rev. Lett. 108 (2012), p. 111601. arXiv: [1111.5206 \[hep-ph\]](#) (cit. on pp. 53,  
 2112 56, 57).
- 2113 [134] A. Denner, S. Dittmaier, and L. Hofer. COLLIER: *A fortran-based complex one-loop*  
 2114 *library in extended regularizations*. Comput. Phys. Commun. 212 (2017), pp. 220–238.  
 2115 arXiv: [1604.06792 \[hep-ph\]](#) (cit. on pp. 53, 56, 57).
- 2116 [135] F. Buccioni et al. *OpenLoops 2*. Eur. Phys. J. C 79.10 (2019), p. 866. arXiv: [1907.13071](#)  
 2117 [hep-ph] (cit. on p. 53).
- 2118 [136] S. Frixione, G. Ridolfi, and P. Nason. *A positive-weight next-to-leading-order Monte*  
 2119 *Carlo for heavy flavour hadroproduction*. JHEP 09 (2007), p. 126. arXiv: [0707.3088](#)  
 2120 [hep-ph] (cit. on pp. 54, 55, 57).
- 2121 [137] P. Nason. *A new method for combining NLO QCD with shower Monte Carlo algo-*  
 2122 *rithms*. JHEP 11 (2004), p. 040. arXiv: [hep-ph/0409146](#) (cit. on pp. 54, 55, 57).
- 2123 [138] S. Frixione, P. Nason, and C. Oleari. *Matching NLO QCD computations with parton*  
 2124 *shower simulations: the POWHEG method*. JHEP 11 (2007), p. 070. arXiv: [0709.2092](#)  
 2125 [hep-ph] (cit. on pp. 54, 55, 57).
- 2126 [139] S. Alioli, P. Nason, C. Oleari, and E. Re. *A general framework for implementing NLO*  
 2127 *calculations in shower Monte Carlo programs: the POWHEG BOX*. JHEP 06 (2010),  
 2128 p. 043. arXiv: [1002.2581 \[hep-ph\]](#) (cit. on pp. 54, 55, 57).

- 2129 [140] NNPDF Collaboration, R. D. Ball, et al. *Parton distributions with LHC data*. Nucl.  
2130 Phys. B 867 (2013), p. 244. arXiv: 1207.1303 [hep-ph] (cit. on pp. 54, 55, 57).
- 2131 [141] M. Bähr et al. *Herwig++ physics and manual*. Eur. Phys. J. C 58 (2008), p. 639.  
2132 arXiv: 0803.0883 [hep-ph] (cit. on p. 54).
- 2133 [142] J. Bellm et al. *Herwig 7.0/Herwig++ 3.0 release note*. Eur. Phys. J. C 76.4 (2016),  
2134 p. 196. arXiv: 1512.01178 [hep-ph] (cit. on p. 54).
- 2135 [143] S. Alekhin, J. Blümlein, S. Klein, and S. Moch. *The 3-, 4-, and 5-flavor NNLO parton  
2136 distribution functions from deep-inelastic-scattering data at hadron colliders*. Physical  
2137 Review D 81.1 (Jan. 2010). ISSN: 1550-2368. arXiv: 0908.2766 [hep-ph] (cit. on  
2138 pp. 54, 55).
- 2139 [144] ATLAS Collaboration. *Studies on top-quark Monte Carlo modelling for Top2016*.  
2140 ATL-PHYS-PUB-2016-020. 2016. URL: <https://cds.cern.ch/record/2216168> (cit. on  
2141 p. 55).
- 2142 [145] S. Frixione, E. Laenen, P. Motylinski, C. White, and B. R. Webber. *Single-top hadropro-  
2143 duction in association with a W boson*. JHEP 07 (2008), p. 029. arXiv: 0805.3067  
2144 [hep-ph] (cit. on p. 55).
- 2145 [146] T. Gleisberg and S. Höche. *Comix, a new matrix element generator*. JHEP 12 (2008),  
2146 p. 039. arXiv: 0808.3674 [hep-ph] (cit. on p. 56).
- 2147 [147] C. Anastasiou, L. Dixon, K. Melnikov, and F. Petriello. *High-precision QCD at hadron  
2148 colliders: Electroweak gauge boson rapidity distributions at next-to-next-to leading or-  
2149 der*. Phys. Rev. D 69 (2004), p. 094008. arXiv: hep-ph/0312266 (cit. on p. 56).

- 2150 [148] ATLAS Collaboration. *ATLAS data quality operations and performance for 2015–*  
2151 *2018 data-taking*. JINST 15 (2020), P04003. arXiv: 1911.04632 [physics.ins-det]  
2152 (cit. on p. 58).
- 2153 [149] ATLAS Collaboration. *Analysis of  $t\bar{t}H$  and  $t\bar{t}W$  production in multilepton final states*  
2154 *with the ATLAS detector*. ATLAS-CONF-2019-045. 2019. URL: <https://cds.cern.ch/record/2693930> (cit. on pp. 64, 67, 79).
- 2155  
2156 [150] ATLAS Collaboration. *Measurement of the total and differential cross-sections of  $t\bar{t}W$*   
2157 *production in  $pp$  collisions at  $\sqrt{s} = 13$  TeV with the ATLAS detector*. JHEP 05 (2024),  
2158 p. 131. arXiv: 2401.05299 [hep-ex] (cit. on p. 64).
- 2159 [151] ATLAS Collaboration. *Search for new phenomena in events with same-charge leptons*  
2160 *and  $b$ -jets in  $pp$  collisions at  $\sqrt{s} = 13$  TeV with the ATLAS detector*. JHEP 12 (2018),  
2161 p. 039. arXiv: 1807.11883 [hep-ex] (cit. on p. 68).
- 2162 [152] ATLAS Collaboration. *Search for  $R$ -parity-violating supersymmetry in a final state*  
2163 *containing leptons and many jets with the ATLAS experiment using  $\sqrt{s} = 13$  TeV*  
2164 *proton–proton collision data*. Eur. Phys. J. C 81 (2021), p. 1023. arXiv: 2106.09609  
2165 [hep-ex] (cit. on p. 70).
- 2166 [153] E. Gerwick, T. Plehn, S. Schumann, and P. Schichtel. *Scaling Patterns for QCD Jets*.  
2167 JHEP 10 (2012), p. 162. arXiv: 1208.3676 [hep-ph] (cit. on p. 70).
- 2168 [154] G. Avoni et al. *The new LUCID-2 detector for luminosity measurement and moni-*  
2169 *toring in ATLAS*. JINST 13.07 (2018), P07017 (cit. on p. 72).
- 2170 [155] ATLAS Collaboration. *Tagging and suppression of pileup jets*. ATL-PHYS-PUB-2014-  
2171 001. 2014. URL: <https://cds.cern.ch/record/1643929> (cit. on pp. 73, 75).

- 2172 [156] ATLAS Collaboration. *Measurements of inclusive and differential fiducial cross-sections*  
2173 *of  $t\bar{t}$  production with additional heavy-flavour jets in proton–proton collisions at  $\sqrt{s} =$*   
2174 *13 TeV with the ATLAS detector.* JHEP 04 (2019), p. 046. arXiv: 1811.12113 [hep-ex]  
2175 (cit. on p. 77).
- 2176 [157] D. de Florian et al. *Handbook of LHC Higgs Cross Sections: 4. Deciphering the Nature*  
2177 *of the Higgs Sector.* CERN Yellow Rep. Monogr. 2 (2017), pp. 1–869. arXiv: 1610.  
2178 07922 [hep-ph] (cit. on p. 77).
- 2179 [158] ATLAS Collaboration. *Measurement of the production cross-section of a single top*  
2180 *quark in association with a Z boson in proton–proton collisions at 13 TeV with the*  
2181 *ATLAS detector.* ATLAS-CONF-2017-052. 2017. URL: <https://cds.cern.ch/record/2273868> (cit. on p. 77).
- 2183 [159] F. Demartin, B. Maier, F. Maltoni, K. Mawatari, and M. Zaro. *tWH associated*  
2184 *production at the LHC.* EPJC 77.1 (2017). arXiv: 1607.05862 [hep-ph]. URL: <https://doi.org/10.1140/epjc/s10052-017-4601-7> (cit. on p. 77).
- 2186 [160] ATLAS Collaboration. *Measurement of  $W^\pm Z$  production cross sections and gauge*  
2187 *boson polarisation in pp collisions at  $\sqrt{s} = 13$  TeV with the ATLAS detector.* Eur.  
2188 Phys. J. C 79 (2019), p. 535. arXiv: 1902.05759 [hep-ex] (cit. on p. 77).
- 2189 [161] G. Cowan, K. Cranmer, E. Gross, and O. Vitells. *Asymptotic formulae for likelihood-*  
2190 *based tests of new physics.* The European Physical Journal C 71.2 (Feb. 2011). ISSN:  
2191 1434-6052. arXiv: 1007.1727 [physics.data-an]. URL: <http://dx.doi.org/10.1140/epjc/s10052-011-1554-0> (cit. on p. 81).
- 2193 [162] J. Neyman and E. S. Pearson. *IX. On the problem of the most efficient tests of*  
2194 *statistical hypotheses.* Philosophical Transactions of the Royal Society of London.

- 2195 Series A, Containing Papers of a Mathematical or Physical Character 231.694-706
- 2196 (1933), pp. 289–337 (cit. on p. 81).
- 2197 [163] S. S. Wilks. *The large-sample distribution of the likelihood ratio for testing composite*  
2198 *hypotheses*. Annals of Mathematical Statistics 9.1 (1938), pp. 60–62 (cit. on p. 82).
- 2199 [164] T. Junk. *Confidence level computation for combining searches with small statistics*.  
2200 Nuclear Instruments and Methods in Physics Research Section A: Accelerators, Spec-  
2201 trometers, Detectors and Associated Equipment 434.23 (Sept. 1999), 435443. ISSN:  
2202 0168-9002. arXiv: [hep-ex/9902006 \[hep-ex\]](https://arxiv.org/abs/hep-ex/9902006) (cit. on p. 83).
- 2203 [165] A. L. Read. *Modified frequentist analysis of search results: The CLs method*. Tech.  
2204 rep. CERN-OPEN-2000-205. Presented at Workshop on Confidence Limits, Geneva,  
2205 Switzerland. CERN, 2000. URL: <https://cds.cern.ch/record/451614> (cit. on p. 83).